View metadata, citation and similar papers at core.ac.uk

brought to you by CORE

provided by Carolina Digital Repository

# MICROPALLET ARRAYS AS AN INTEGRATED PLATFORM FOR THE CHARACTERIZATION AND MANIPULATION OF SINGLE CELLS

Pavak Kirit Shah

A dissertation submitted to the faculty at the University of North Carolina at Chapel Hill in partial fulfillment of the requirements for the degree of Doctor of Philosophy in the School of Medicine (Biomedical Engineering).

Chapel Hill
2014

Approved by:

Nancy L. Allbritton

David S. Lalush

Shawn M. Gomez

James E. Bear

Michael B. Major

This work by Pavak Kirit Shah is licensed under a Creative Commons Attribution-NonCommercial-NoDerivatives 4.0 International License.
To view a copy of this license, see Appendix 1 or visit http://creativecommons.org/licenses/by-nc-nd/4.0/

# ABSTRACT

Pavak Kirit Shah: Micropallet Arrays as an Integrated Platform for the Characterization and Manipulation of Single Cells
(Under the direction of Nancy L. Allbritton)

Cell isolations remain a critical bottleneck in cell biology. Fluorescence activated cell sorting (FACS) revolutionized the field by enabling rapid sorting of samples based on cell surface markers and bulk optical properties. Despite these advances, it remains impossible or prohibitively difficult to sort cells based on dynamic and morphological characteristics or to sort cells from extremely small samples such as are typically acquired from patient biopsies and small animal models. The work described in this dissertation is focused on the development of an integrated platform that can surmount the limitations of existing sorting technologies through the integration of a microfabricated platform and image cytometry.

The integration of simple microdevices such as microwell arrays with image-based cytometry has enabled temporally and spatially resolved single-cell measurements to be performed with high-throughput yet such instruments remain incapable of sorting cells based on this expanded feature-space. Micropallet arrays are a simple, scalable platform for performing high-throughput single-cell assays with spatial and temporal resolution. Individual elements from the array can also be released using low-energy laser pulses, enabling single-cell isolations to be performed with high purity and yield from extremely small samples.

A transparent, biocompatible and superparamagnetic composite photoresist was developed to enable the fabrication of micropallet arrays which could be manipulated by external magnetic fields after release. This enabled the collection of released micropallets against gravity to improve the purity of sorts. An imaging cytometer was developed which combined high-throughput automated image acquisition and analysis of micropallet arrays with automated laser-based miropallet release for single-cell isolation. As a demonstration of the capability of micropallet arrays to sort exceedingly small and diverse samples as well as to characterize the performance of the automated platform, patient-derived xenograft tumor samples were sorted to yield pure populations of tumor cells from a mixture of tumor and host stromal tissue. This platform was subsequently applied to the study of the heterogeneity exhibited by monoclonal melanoma cell populations in their dynamic response to stimulation by Wnt-3a.

# ACKNOWLEDGEMENTS

There are many people whom I would like to thank for their guidance and support in helping me learn, grow, achieve and find happiness. The last few years of my life have been a journey and I have been blessed to have had the pleasure of all of your company for it.

First and foremost I must thank my family for making my life rich and fulfilling and for giving me a home I could look forward to coming back to. Mom and Dad, it was your encouragement and love from day one that taught me the curiosity that inspired me to pursue science, the discipline to accomplish what I set out to and the values to always try to be a better person. Thank you Naman, for having my back, showing me the way and for just being the best brother anyone could ask for. To Sapna, thank you for your love, smiles, and always being understanding and supportive of my dreams.

I have had many mentors over the years that have constantly challenged, inspired and taught me and to whom I owe a great deal. Thank you Mr. Enns and Ms. Wormald, for encouraging my interest in science and making school fun. To Dr. Stefan Franzen, thank you for welcoming me into the academic world before I knew what it was and for showing me what it meant to make a career of science. To Dr. Howard Shapiro, I have had few teachers from whom I have learned so much- not just about science, but of the challenges that face the world and the need for people to acknowledge, understand and address them. I must also thank you for introducing me to my current mentors. Dr. Nancy Allbritton, thank you for your guidance, patience and persistence in keeping me focused. I could have easily spent a decade exploring the technologies developed in your lab, but you never let me forget about my goals. To Dr. Christopher Sims, thank you for helping me along every step of the way and giving me opportunities to learn and grow.

To all of the past and present members of the Allbritton lab, thank you for making every day at work for me fun and filled with friends, however there are a few individuals that I must thank in particular. Dr. Ryan Phillips, in addition to the many hours of entertaining philosophizing, you encouraged and helped me to stay far healthier and more active in grad school than I would have otherwise. Dr. Angela Proctor and Dr. Michelle Kovarik, I will always appreciate the help and advice you gave me in every aspect of my graduate career. Dr. Nicholas Dobes, Dr. Philip Gach, Asad Ahmad and Peter Attayek; we've worked on so much and enjoyed so many good times together, thank you all for being awesome. Dr. Yuli Wang, Dr. Wei Xu and Dr. Frank Pai, thank you for everything you taught me about microfabrication. To Emilie Mainz, Abigail Turner, Jazz Dickinson and Greg Woss, thank you for the many fun conversations, great suggestions and so much help over the years. Finally, thank you to all of the classmates, colleagues, teachers and collaborators at UNC and NCSU that helped make grad school an adventure.

## TABLE OF CONTENTS

# LIST OF FIGURES

# LIST OF TABLES

# LIST OF ABBREVIATIONS AND SYMBOLS

| Abbreviation | Definition |
|---|---|
| °C | Degrees celsius |
| μg | microgram |
| μL | microliter |
| μm | micrometer |
| 3D | 3-dimensional |
| A375 | A human cell line derived from malignant melanoma |
| A375-BAR-mCherry | A375 cell line transformed with the beta catenin activated reporter coupled to a nuclear localization signal tagged mCherry fluorescent protein |
| ABS | Acrylonitrile butadiene styrene |
| APC | Adenomatous polyposis coli protein |
| API | Application programming interface |
| BAR-mCherry | The beta catenin activated reporter coupled to a nuclear localization signal tagged mCherry fluorescent protein |
| BODIPY | Boron-dipyrromethene |
| CCD | Charge-coupled device |
| CMOS | Complementary metal-oxide-semiconductor |
| CRC | Colorectal cancer |
| CTC | Circulating tumor cell |
| DI | Deionized |
| DKK | Dickkopf-related protein |

| | |
|---|---|
| DMEM | Dulbecco's modified eagle medium |
| DMSO | Dimethylsulfoxide |
| DSC | Differential scanning calorimetry |
| ECB | Extracellular buffer |
| ECM | Extracellular matrix |
| EM-CCD | Electron multiplying charge-coupled device |
| EpCAM | Eptheilial cell adhesion molecule |
| EpCAM+ | Eptheilial cell adhesion molecule positive |
| FACS | Fluorescence activated cell sorting |
| Fbn | Fibronectin |
| FBS | Fetal bovine serum |
| $Fe(NO_3)_2$ | Iron (II) nitrate |
| $FeCl_2$ | Iron (II) chloride |
| $FeCl_3$ | Irone (III) chloride |
| g | Gram |
| GBL | Gamma-butyrolactone |
| Gel | Gelatin |
| GFP | Green fluorescent protein |
| GSK3 | Glycogen synthase kinase 3 |
| h | Hour |
| H2B-GFP | A fusion protein between histone-2B and green fluorescent protein |
| $HNO_3$ | Nitric acid |
| KCl | Potassium chloride |

| | |
|---|---|
| kg | Kilogram |
| $KH_2PO_4$ | Potassium phosphate, monobasic |
| LCM | Laser capture microdissection |
| LEF | Lymphoid enhancer-binding factor, a family of transcription factors |
| LSC | Laser scanning cytometry |
| M | Molarity (moles per liter) |
| MACS | Magnetic activated cell sorting |
| mCherry | A red fluorescent protein derived from green fluorescent protein |
| mg | Milligram |
| min | Minute |
| mL | Milliliter |
| mm | Millimeter |
| mM | Millimolar (millimoles per liter) |
| $mm^2$ | Square millimeter |
| MSC | Mesenchymal stem cell |
| MTT | 3-(4,5-dimethylthiazol-2-yl)-2,5-diphenyltetrazolium bromide |
| N.A. | Numerical aperture |
| $Na_2HPO_4$ | Sodium phosphate, dibasic |
| NaCl | Sodium chloride |
| Nd:YAG | Neodynium-doped yttrium aluminum garnet |
| ng | Nanogram |
| $NH_4OH$ | Ammonium hydroxide |
| nm | Nanometer |

| | |
|---|---|
| PBS | Phosphate-buffered saline |
| PCR | Polymerase chain reaction |
| PDMS | Polymitheylsiloxane |
| PDX | Patient-derived xenograft |
| PMMA/1002F | Poly(methyl methacrylate) / 1002F |
| PMMA/MMA | Poly(methyl methacrylate-co-methacrylic acid) |
| PMT | Photomultiplier tube |
| s | Second |
| SDS | Sodium dodecyl sulfate |
| SEM | Scanning electron microscope |
| TC | Tissue culture polystyrene |
| TCF | T-cell factor, a family of transcription factors |
| TEM | Transmission electron microscope |
| UV | Ultraviolet |
| UV-Vis | Ultraviolet-visible |
| Wnt | Wingless-related integration site |
| β-catenin | Beta cadherin associated protein |
| β-TrCP | Beta transducin repeat containing protein |

# Chapter 1: Introduction

## 1.1 The heterogeneity of biological systems

### 1.1.1 Tumor diversity and evolution

Cancer remains the most commonly studied family of diseases and while advances in its detection and treatment have been made, significant gaps in the understanding of its emergence, evolution and metastasis remain. These advances have principally been driven by concurrent developments in genetic and molecular characterization techniques that have shaped and continue to shape our understanding of the disease. Perhaps the most critical recent advance in the development of anti-cancer therapeutics was the discovery of abnormalities of signaling pathways in cancer cells and their association, through genetic and molecular investigations, to specific enzymes. The identification of breast cancer bearing increased expression levels of ERBB2 and the production of the Bcr-Abl fusion kinase as a result of chromosomal translocation in three forms of leukemia (chronic myelogenous, acute lymphoblastic and acute myelogenous) led to the development of two of the most successful targeted cancer therapies (respectively, trastuzumab[1] and imatinib[2]).

The success of these therapeutics has resulted in an explosion of novel targeted therapies, yet our understanding of cancer continues to evolve. Increasing instances of resistance to targeted inhibitor therapy[3–6] called into question the simplified view of cancer as a monolithic disease and on-going work continues to build on the genetic and molecular understanding of cancer as a diverse, heterogeneous disease[7,8].

Advances in single-cell assays have greatly expanded an understanding of the diversity and heterogeneity present in seemingly simple biological systems. Advances in analytical tools for biochemical assays have significantly accelerated understanding the genomic[8,9], transcriptional[10–12] and proteomic[13–15] heterogeneity present in biology and their role in governing normal and pathological function. A significant amount of focus has been given to cancer for characterization at the single-cell level and single-cell technologies continue to unravel the mechanisms by which cancers emerge[16–18], evolve[8,19,20] and metastasize[18,21–23]. While much of the integrative perspective on heterogeneity has been driven by so-called '-omics' approaches to analysis, more targeted investigations employing cytometric approaches have also made discoveries possible and are critical tools in the pipeline from basic discovery to the development of new diagnostics and therapeutics.[24–30]

Central to this understanding of cancer as a heterogeneous disease is the fundamental genetic instability of most cancers[8]. Intense growth pressure within tumors coupled with competition for nutrients and oxygen creates an environment well-suited to the selection of aggressive and robust mutants[31]. Single-cell sequencing investigations have shown that tumors typically evolve to consist of a small number of successful sub-clones as well as a large reservoir of cells which are rapidly mutating and genetically diverse[8]. This observation leads easily toward a model of cancer as an evolving population while also providing a potential explanation for the emergence of resistance to targeted therapy.

### 1.1.2 Emerging perspectives on clonal heterogeneity

The observation of genetic[8,9,19,20] and phenotypic[10,21,23,32] diversity within tumors has led to significant interest in fundamental investigations of biological heterogeneity. A distinction must be made between the concepts of heterogeneity and biological noise. All biological systems are subject to some degree of stochastic fluctuation[13] although the majority of biological systems are sufficiently well regulated to prevent these fluctuations from significantly affecting cellular phenotype[33]. Phenotypic heterogeneity, however, can originate from a variety of different sources. Studying monoclonal populations in which genetic heterogeneity has been eliminated as a contributing factor has revealed a broad diversity in phenotypes present in seemingly homogeneous populations[34–38]. While the origin of this heterogeneity is poorly understood, it is widely believed to play a role in increasing the resistance of cancers to targeted inhibitor therapy[3–8].

### 1.1.3 Divide and Conquer: Tackling heterogeneity in biological samples

In-vitro biological research typically relies upon two types of human and mammalian tissue samples: cultured cell lines and primary cells sampled directly from an organism. While studies of primary cells are likely to be the most biologically relevant[39–41], cultured cell lines are often more uniform in nature and are significantly easier to obtain. Primary cell samples are typically more difficult to culture, highly variable in size and mixed in composition. Due to being sampled directly from living tissue, primary samples typically contain cell types from multiple tissues of origin including muscle, vascular and immune cells. This complicates many traditional biological assays which rely on pooling analytes extracted from large numbers of cells.

Several strategies exist for tackling heterogeneous biological samples, but most can be broadly classified into two approaches: divide and conquer. ‘Divide’ approaches typically rely on cell sorting techniques to purify or enrich target cell populations from a sample while ‘Conquer’ approaches utilize markers of cellular identity to track target populations within a mixed sample. Each approach has its limitations and advantages as well as a wide variety of implementations. Some strategies and technologies that fall under this classification scheme will be discussed in greater detail in the following sections.

## 1.2 Divide: Cell Sorting

### 1.2.1 Manual manipulation

A variety of techniques for manual cell sorting have been developed of which two remain in common usage: limiting dilution and colony picking. Limiting dilution involves the serial dilution of a cell suspension and then separation of that suspension into aliquots of a size determined to maximize the probability of yielding only one cell per aliquot. The dilution and aliquoting process is a counting problem and thus well described by a Poisson distribution[42]. The Poisson distribution is shown in equation 1.1 where x is the expected number of cells per aliquot and lambda (λ) is the average number of cells per aliquot.

$$(1.1) \qquad \Pr(x = k) = \frac{\lambda^k e^{-\lambda}}{k!}$$

Based on this relationship, the probability that x = 1 is maximal when λ = 1 and is 36.79%. As a result, this process is inefficient with an additional 36.79% of aliquots expected to contain 0 cells and the remaining 26.42% of aliquots expected to contain >1 cell and therefore potentially be an impure mixture. Increased yield can thus only be achieved by increasing the number of replicates or the number of wells seeded in the case of limiting dilutions. For macroscale well plates, this significantly increases the reagent consumption and labor cost of cell isolation by limiting dilution. Additionally, the error rate inherent in the random dilution process requires that each aliquot be inspected to verify that only a single cell was collected and that the cell belongs to the targeted population. For example, isolating 100 cells from a mixture in which the target cell consists of 10% of the total population would require the generation of an average of 2,718 aliquots or 29 96-well plates and consume 543.6 mL of cell culture media.

Colony picking and cloning rings are closely related approaches in which a dilute suspension of cells is seeded onto a cell-culture substrate and allowed to proliferate into clonal colonies. The colonies must be tracked closely during this proliferation to identify adjacent colonies which may have merged and are no longer pure or clonal in nature. Once colonies have been established, clones of the target cell type can be manually collected by scraping or pipetting and transferred onto separate culture surfaces for further expansion or analysis.

Taken together, manual cell isolation techniques are labor intensive and limited in throughput. They allow for a broad selection of criteria that can be used in determining the identity of target cells including cell surface staining, cell morphology, dynamic cell phenotypes and, if colonies can be readily split, gene expression or cell-internal staining after fixation. For many difficult cell separation problems, such as the isolation of single circulating tumor cells[10] and genetically engineering stem cells[43–45], limiting dilution and colony picking remain the gold standards for sorting.

### 1.2.2 Fluorescence Activated Cell Sorting (FACS)

The flow cytometer revolutionized the study of single cells by introducing the ability to rapidly sort cells based on the simultaneous measurement of large numbers of fluorescence indicators[46]. In flow cytometry, flow focusing narrows and centers the flow of a suspension of single cells within a flow cell. One or more lasers or arc lamps are used to excite fluorophores internal to or bound to the cells and the fluorescence emitted and light scattered by individual cells is collected as they pass through an observation point and measured using photomultiplier tubes (PMTs)[46]. The use of laser excitation and PMT-detection provides flow cytometers with high sensitivity. Using multiple excitation sources and cross-channel fluorescence compensation, >20 optical parameters can be monitored simultaneously, allowing for very high levels of label multiplexing[47]. Based on user-provided thresholds in multiple channels, target cell populations can be identified to trigger a downstream sort as described below.

The use of fluorescence measurements to trigger cell sorting is referred to as Fluorescence Activated Cell Sorting (FACS). The most common method for sorting cells passing through a flow cytometer involves the agitation of the flow cell with ultrasonic vibrations, breaking the sheath and core liquid flows into discrete droplets[48]. By synchronizing droplet generation with the sample flow rate, droplets containing individual targeted cells can be charged upon passing through a ring electrode and then deflected into collection wells by charged plates. This process can be highly sensitive to calibration, however, and target cells are often missed or doublets can be collected[49–51]. The effects of this are particularly evident when attempting to sort very small starting samples of cells and performance degrades rapidly when sorting samples smaller than $10^5$ cells[52].

While FACS remains the gold standard for high throughput live cell sorting, several key limitations are of note. The use of bulk fluorescence or light scattering readouts limits the criteria that can be used to select cells to be sorted to non-toxic membrane permeable dyes, cell surface markers that can be labeled with antibodies and bulk optical properties such as scatter and absorbance. Additionally, each cell can only be interrogated once as it passes through the observation window, a time period typically on the order of microseconds[46], making it impossible to collect dynamic information about single cells let alone to sort based on those dynamic measurements.

### 1.2.3 Magnetic-Activated Cell Sorting (MACS)

MACS is a far younger technology than FACS, with its first incarnation described in 1990.[53] MACS is a passive sorting modality in which cells are functionalized by biotin-labeled antibodies which can then bind streptavidin, allowing biotin-coated magnetic nanoparticles (on the order 0.1 μm in diameter) to be attached to the cell through the streptavidin linker. The functionalized cells can then be either enriched by positive selection or depleted by negative selection by passing through a magnetic column. The use of either approach depends strongly on the prevalence of the target cell population as when the target cell population is sufficiently abundant, depletion of non-target cells can be achieved with rates of up to 1,000-fold while positive enrichment is possible up to 100-fold due to non-specific binding of nanoparticles and interactions between the cells and the magnetic column.[53]

Utilization of a passive enrichment approach dramatically simplifies the instrumentation required for enrichment, however MACS is limited relative to alternative sorting technologies in several critical manners. First, each selection step is limited to a single bulk enrichment based on the presence or absence of magnetic nanoparticles and therefore is incapable of performing selection based on the presence or absence of multiple markers. The use of antibody binding also limits the selection of labels to cell surface markers for which antibodies (or more recently, aptamers[54,55]) exist. Furthermore, as the enrichment occurs in bulk solution, isolating single cells requires subsequent isolation by an additional sorting technology.

While effective as an enrichment tool, the purity and yield of MACS suffers with very small initial samples[52] and with samples containing target cells at very low concentrations.[56] Despite these limitations, its simplicity and ability to rapidly process large sample volumes has made it a popular enrichment technique in immunology[57–60] and the study of circulating tumor cells (CTCs).[61–65] In fact, CellSearch™ (Janssen Diagnostics, LLC), the only currently FDAapproved platform for CTC enrichment, relies on MACS to enable detection and enumeration of CTCs.

### 1.2.4 Microfluidic platforms for cell sorting

A tremendous variety of microfluidic platforms have been developed for the manipulation, sorting and enrichment of mammalian cells. These platforms can be broadly categorized into three families: traps, microfluidic FACS and arrays. While many systems have been developed and demonstrated in the literature for microfluidic sorting of single cells, only one platform is currently commercially available, the $C_1$™ single-cell auto prep system by Fluidigm Corporation, which utilizes a fluidic trap to capture individual cells for analysis by polymerase chain reaction (PCR).[66] Array-based sorting platforms will be discussed in detail in Section 1.4. Of note is that these sorting modalities are not mutually exclusive and technologies have been demonstrated which employ a combination of approaches to achieve rapid and reliable cell separations.[67]

Trap-based systems for microfluidic cell sorting typically make use of one of two basic formats: filters and fluidic traps. Microfluidic filters function by physically or biochemically separating cell types based either on intrinsic properties of the cell such as size[68,69] or biochemical properties such as the presence of unique surface markers.[70–72] Fluidic traps instead rely on the physical separation of cells in continuous flow by biophysical means, taking advantage of differences in size[67] or dielectric permittivity[73–75] to achieve spatial separation in the context of fluid flow.

Physical trap based systems include hole[76–78] and post arrays[79] which separate cells based on size. These systems typically support high flow rates as they are very scalable and the maximum throughput of the trap is dependent upon the cross-sectional area of the trap array, but have a tendency to clog. Biological samples are often not monodisperse in size and trap based systems typically suffer from poor purity[80] as a consequence. Recent developments in inertial focusing of flowing cell suspensions have mitigated some of these limitations, however, allowing for continuous flow filtration to occur without clogging.[81] These systems rely on the tendency of larger particles to interact with obstacles to induce a lateral displacement of particles that is size-dependent.[82] Purity remains a concern and typically requires a second selection step[67], however size based sorting can be achieved at high flow rates without clogging.[67]

For sorting applications in which size is not a sufficiently good marker for the target cell population of interest, biochemical means for separation are typically employed. The simplest form of biochemical selection of cells involves the use of a functionalized surface that the target cell has a specific affinity for. While this has most commonly been implemented in the form of antibody functionalized surfaces[70–72,80], less specific surface interactions can be utilized for selection.[83] Performance of biochemical surface capture devices is typically limited by the affinity of the functionalized surface, the flow rate through the device and the frequency of interactions between the functionalized surface and the flowing sample. In microfluidic channels where laminar flow dominates, it is frequently the interaction between the sample and the surface that is the limiting factor. Several strategies have been explored to maximize interactions with functionalized surfaces including post arrays to increase the functionalized surface area and to increase the probability of cells colliding with a surface[80], nanoporous substrates which allow for flow perpendicular to the capture surface to be induced[70] and grooves in the capture surface to induce cell rolling[84].

Two primary biophysical methods of sorting cells have been widely demonstrated in the literature: density-dependent inertial sorting and dielectrophoretic sorting. The most common inertial microfluidic sorting approach relies upon Dean drag forces that occur in laminar flow through curved microfluidic channels which acts to orient larger particles along the inner channel wall while smaller particles remain in the core of the flow profile[85]. Dielectrophoretic sorting relies on differences in the electrical permittivity of differing cell types to sort cells by exposing a sample flowing through a microfluidic channel to a non-uniform electrical field, typically achieved by applying alternating voltages across the channel through multiple paired electrodes.[73–75] The non-uniform field generates forces on particles within the fluid-filled channel by electrically polarizing the particle in an orientation which depends on the relative polarizability of the particle and the surrounding fluid. While dielectrophoretic and inertial flow-based sorting systems allow for rapid, continuous sorting of sample streams, both require the presence of significant differences in the biophysical properties of the target cell population relative to non-target cells.

### 1.2.5 Sorting by imaging cytometry

Only a small number of integrated sorting platforms based on imaging cytometry have been demonstrated. The most commercially successful of these platforms is a technology termed laser capture microdissection (LCM) in which selected regions of a tissue slice can be dissected from its surrounding and isolated for further analysis. LCM remains the most commercially successful image based sorting platform available today. While several variants of the core technology platform exist, most follow a similar procedure for analysis and sorting. Typically, LCM begins by imaging stained tissue samples (most often fixed, but live tissue dissection techniques are now available[86–88]) and identifying regions of interest based on colorimetric or fluorescent staining. The name LCM refers to the subsequent dissection process in which targeted regions of the tissue sample are dissected from the surrounding tissue by cutting the targeted region using an IR or UV laser and removing the dissected tissue with one of three methods.

The first method makes use of an adhesive film which is pressed onto the dissected tissue slice and removed, taking the dissected tissue portions with it.[89] While the simplest approach, it is also most non-specific as removal of the adhesive film can also remove loose material from non-dissected regions of the tissue sample. The second LCM extraction technique directly utilizes the dissection laser to melt a plastic film backing onto targeted regions of the tissue sample.[89] This approach improves the specificity of tissue removal but the heating process risks degradation of critical analytes in the sample such as nucleic acids.

The third approach makes use of one a physical separation that does not require direct contact of a removal surface to the tissue sample. These include gravity-assisted microdissection and laser pressure catapult.[90] Other variants have been developed and are commercially available but will not be discussed here, more comprehensive reviews of LCM variants have been published widely.[90–95] Gravity assisted microdissection makes use of a free-standing thin film substrate onto which the tissue sample is mounted. Targeted regions of the tissue sample can be entirely released from the rest of the tissue by cutting through the substrate around the targeted region and allowing it to fall into a collection dish due to gravity. Laser pressure catapult systems work by a similar mechanism but an additional rigid substrate is placed beneath the thin film. A single laser pulse is fired beneath the dissected region after it has been dissected, catapulting the sample into a collection vessel against gravity.

The ability to sort live cells based on LCM has been a relatively recent development, albeit a powerful one. LCM has proven to be the first widely available platform to enable sorting based on image-based measurements on single cells, although it is not without its limitations. The mechanical and thermal stresses that occur during the microdissection and separation steps can result in reduced viability in sorting single cells.[86,96] Additionally, sorting throughput is reduced by the time required to write a laser path around each target cell while avoiding neighboring cells.

## 1.3 Conquer: single-cell analysis

### 1.3.1 Advances in cytometry

Flow cytometry has significantly increased the throughput and content of single-cell analysis but remains limited in several key aspects. While the use of antibody-based staining allows the identification and isolation of cells based on surface markers, many phenotypes of interest to medicine and biology are not specifically identified by surface markers. In addition, the hydrodynamic forces experienced by cells during flow sorting places stress on adherent cells, particularly a concern for mechanosensitive stem cells. The requirement that cells be analyzed in suspension at a single time-point prevents the measurement of parameters requiring spatial and temporal resolution.

Partially in response to these limitations of flow cytometry, cytometry modalities were developed based on traditional fluorescence microscopy[30,97,98] and laser scanning confocal microscopy[99–101]. In imaging cytometry, a motorized microscope capable of automated XYZ sample control is used to scan traditional tissue culture formats including slides and well-plates, measuring fluorescence on an image sensor, typically a charge coupled device (CCD). Images can then be segmented and classified based on a variety of parameters including multi-channel fluorescence data and morphology. In laser scanning cytometry (LSC), an excitation laser is swept over a sample within each field of view of a microscope and fluorescence at each position within the field of view is measured by PMTs.[99] The current output of each PMT is mapped to the intensity of an image based on the position of the laser point at the time of acquisition and thus an image is generated. The use of a laser excitation source and PMT detectors drastically increases the sensitivity and dynamic range of fluorescence measurements in LSC but also increases instrument complexity and cost relative to the use of arc-lamp excitation and image sensors for detection in fluorescence microscope.

LSC systems occupy a middle-ground between fluorescence microscopy and flow cytometry: increasing throughput over microscopy through automation while enabling more sophisticated analyses than is possible by flow cytometry. Only flow cytometry, however, is currently capable of sorting cells based on positive selection criteria. In positive selection, targeted cells are extracted from a mixed population. In contrast, negative selection involves the removal of off-target cells from a mixed population. For relatively rare cell populations of interest, positive selection is significantly more efficient than negative selection as it requires the identification and selection of a smaller total number of cells.

Dramatic advances in camera technology and the computational power of desktop computers combined with increased access to computer-controllable microscope frames have made quantitative and automated fluorescence microscopy increasingly accessible to researchers. In addition, several open-source software development initiatives have provided the groundwork for researchers to develop sophisticated automated imaging and image analysis solutions with relative ease. The Micro-Manager libraries provide a unified application programming interface (API) for controlling a wide variety of microscope bodies, cameras, stages and accessories[102], while tools like ImageJ[103] and CellProfiler[104] provide sophisticated image analysis capabilities without the need for researchers to produce their own implementations of image segmentation, tracking and classification algorithms.

In addition to ready access to instrumentation, imaging cytometry brings several key advantages over competing cytometry platforms to biomedical research. Live-cell imaging combined with automated analysis allows for the collection of rich multi-parametric dynamic measurements at single-cell resolution.[97,105,106] This enables the simultaneous tracking of diverse populations of cells over time, enabling both temporally and spatially resolved measurements to be acquired within a mixed population. Such measurements are not possible with flow cytometry. There remain, however, several major limitations to unconstrained cell tracking by imaging cytometry. While advances in access to increased computational power in desktop computers have increased the ease with which complex image analysis tasks can be performed, the tremendous amount of data that can be produced by time-lapse imaging can still pose a significant bottleneck for image analysis. Additionally, while a larger set of measurements can be drawn from image cytometry data than other cytometry modalities, only a few attempts to enable sorting from image cytometry platforms have been commercially successful.[107,108]

### 1.3.2 Continuing challenges in single-cell analysis

While imaging and flow cytometry modalities have significantly advanced single-cell analysis, only a limited set of assays can be performed with the optical readouts necessary for cytometric analysis. Clonogenic assays are challenging even when optical readouts are possible due to the computational cost and complexity of detecting mitosis and tracking daughter cells when imaging on conventional tissue culture substrates. Single cell sorting by flow cytometry remains a challenge for small samples (<$10^6$ cells) as purity and yield can be inconsistent and requires that sorts be verified before destructive single-cell assays are performed. As a consequence, three critical opportunities exist for high-impact applications of cytometric and sorting technologies:

1. Efficient and automated sorting of exceedingly small samples <$10^4$ cells would simplify the handling and analysis of a variety of primary cell samples from patient biopsies and small animal models.
2. Rapid, simple and massively parallel clonogenic assays would enable a new generation of investigations into single-cell heterogeneity.
3. Reliable, intrinsically verified single-cell separations would simplify analysis pipelines for a number of single-cell molecular assays including genome sequencing, transcriptome sequencing, PCR and chemical cytometry among others.

## 1.4 Micropallet arrays

Micropallet arrays are a promising technology for the study and manipulation of single cells and cell colonies. Micropallets are arrays of pedestals fabricated on a substrate (typically glass) by conventional ultraviolet (UV) photolithography.[109] UV photolithography allows for a wide variety of materials[110,111], geometries and functional variations[112–118] to be produced with well-established chemistries and hardware. The array substrate can readily be treated to be hydrophobic, causing air bubbles to be trapped between the micropallets upon immersion in aqueous solutions such as cell culture media.[119] These bubbles prevent cells from migrating between micropallets and can be sustained for up to 7 days for long-lasting experiments. Individual elements from micropallet arrays can be released from the substrate by focusing a nanosecond-duration laser pulse at the interface between the glass and the photoresist through a high numerical aperture (N.A.) lens. The release process is rapid, occurring in microseconds[120], and can sort sensitive primary[121] and stem cell[122] populations with high yield and high viability.

### 1.4.1 Micropallet array fabrication

Micropallet arrays were first fabricated using the epoxy-based photoresist SU-8[109]. SU-8 was initially chosen for its ability to produce high aspect ratio structures, but its high autofluorescence and poor biocompatibility led to the development of an alternative, based on the Epon resin 1002F[123]. 1002F improved significantly on SU-8 in autofluorescence and biocompatibility, at the cost of a reduced maximum achievable aspect ratio (4:1). Basic micropallet array fabrication occurs in 5 steps as shown in Figure 1.1 below. The basic process involves:

1. A uniform film of the photoresist is generated on the substrate by spin-coating.
2. Solvent is removed from the film by a 'soft-bake' at 95 °C for a duration determined by the thickness of the film.
3. The film is exposed to long-wave UV light (>360 nm) through a patterned chrome mask with a total dose determined by the thickness of the film.
4. The exposed regions of the film are cross-linked by heating to 95 °C for 10 min.
5. The uncrosslinked photoresist is removed by developing in 1-methoxy-2-propyl acetate.

Initial release experiments with SU-8 and 1002F-based micropallets required the micropallet array to be inverted over a collection dish so released micropallets could be collected by gravity.[109,124] This approach introduced contamination from weakly adherent cells which could detach from the array and settle to the collection dish as well and motivated the development of a transparent, magnetic photoresist which would allow for the collection of micropallets against gravity to improve the purity of sorting.[111] This photoresist was challenging to synthesize, however, as it required high intensity ultrasonication in order to prevent the formation of macroscopic aggregates of the iron oxide nanoparticles used to impart magnetic properties to the photoresist and thus could only produce small quantities of magnetic photoresist at a time. This limitation motivated the work presented in Chapter 2 to develop a batch-scalable process for producing a transparent, biocompatible magnetic composite photoresist for micropallet array fabrication.

### 1.4.2 Virtual air walls: clonal segregation on micropallet arrays

A critical consideration for micropallet arrays is the prevention of cell adhesion to the sidewall of the micropallet (detrimental to imaging), cell adhesion in the gap between micropallets (impossible to sort) and cell migration between adjacent micropallets (makes cell tracking difficult). This was achieved through the treatment of the micropallet array with a hydrophobic silane, (heptadecafluoro-1,1,2,2-tetrahydrodecyl)-1-trichlorosilane. When treated with the hydrophobic silane and immersed in aqueous solution, the micropallet array traps air in the gaps between micropallets, these air-filled gaps are termed 'virtual air walls'[119]. The exceedingly hydrophobic surface coupled with the air liquid interface at the micropallet gap serves to prevent cell adhesion in and migration across the virtual air-wall, allowing each individual micropallet to be maintained as a clonally isolated culture site while allowing cells to share media and exchange soluble factors. The stability of the virtual air walls was shown to be a function of the gap width, side length and thickness of a micropallet array with square elements. The transition from Wenzel (homogeneous) to Cassie-Baxter (heterogeneous) wetting[125] was observed to occur above a roughness factor (R) of 1.6 when calculated using

Equation 1.2 where b is the side length of the micropallet, a is the gap between adjacent micropallets and h is the thickness of the micropallet[119]. Additional factors that affect the stability of virtual air walls include the ionic strength (improves stability), surface tension (improves stability) and protein concentration (reduces stability) of the solution. [119]

$$(1.2) \qquad R = \frac{4bh + (a+b)^2}{(a+b)^2}$$

### 1.4.3 Micropallet release: Enabling sorting on micropallet arrays

Laser light, when focused through a high N.A. lens, produces strong electric fields within the focal volume which, if the field strength is sufficiently high, can result in bulk ionization therein.[120] The resulting plasma, if confined as at the interface between two materials, produces a high pressure gas which can expand at the interface and disrupt the adhesion between the layers. This phenomenon is utilized to effect the release of micropallets from their glass substrate in a controlled fashion. By tuning the laser energy, individual micropallets can readily be released from the array with a single pulse without affecting the adhesion or viability of the target cell which is protected by the intervening bulk material of the micropallet. Sensitive stem cells such as primary canine myoblasts[121] and murine embryonic cells[122] have been sorted using this approach without inducing differentiation or cell death.

## 1.5 Imaging and image analysis

### 1.5.1 Noise and imaging

The majority of the information presented in this section is well described in standard textbooks that discuss the fundamentals of image sensor operation as well as recent developments and their implications for microscopy and scientific imaging. The material herein is drawn from detailed discussions of image sensors and important considerations for light microscopy from **Fundamentals of Light Microscopy and Electronic Imaging**.[126] This section is intended as an overview of important considerations in the design of an imaging system for cytometry and is not meant to be an exhaustive treatment. Information found from other sources will be cited accordingly.

Noise, sensitivity, resolution and throughput are fundamentally interdependent and critical performance considerations in the design of an imaging cytometer. These parameters are a function of several physical components of the image sensor design of which two principal variants are most commonly utilized: interline charge coupled device (CCD) and complementary metal oxide semiconductor (CMOS) based cameras. There are three primary sources of noise in image sensors: dark noise, counting noise and readout noise.

Dark noise is generated by charge accumulation due to thermally induced currents in the sensor. Dark noise is typically uniform across the sensor and increases linearly with exposure, allowing for its straightforward removal through the subtraction of a 'dark frame' in which no illumination or sample is present from each subsequent image. Dark noise is typically of little consequence in modern cameras, as it has been effectively eliminated in the majority of scientific cameras by actively cooling the sensor to reduce the thermal current build-up.

Counting noise, often referred to as 'shot' noise, is a problem inherent to all light measurement and is caused by the discrete nature of light and charge. Since all light sensors are, in essence, counting photons by converting the energy of each incident photon into a charge, stochastic variations in the number of photons absorbed by each sensor pixel occur. These variations are described by the Poisson distribution whose probability mass function was shown in equation 1. A key feature of the Poisson distribution is that the variance of the distribution is equal to its mean. As a consequence, the standard deviation of photons for a mean incident photon rate of $\mu$ will be $\sqrt{\mu}$ resulting in a decrease in the relative variation in photon counts as $\mu$ increases. From a practical standpoint counting noise can thus be decreased by collecting more photons. Three approaches can be employed to this end in cytometric systems: increasing illumination, utilizing more fluorophore or a fluorophore with higher quantum efficiency, or increasing the size of each detector element. Increasing illumination can be extremely effective but must be employed with caution as photobleaching and phototoxicity can become significant at high light fluence. Increasing the concentration of fluorophore also brings similar trade-offs as non-specific labeling and dye toxicity increase at high concentrations. Fluorophores such as fluorescein and rhodamine remain popular due to their low cost and well-characterized chemistries but suffer from relatively poor quantum efficiency and photobleach readily.[127] A number of new dyes such as the Alexa Fluor family[128] and the boron-dipyrromethene (BODIPY) family[129] of dyes have been developed with significant improvements in quantum efficiency, environmental stability and wavelength tunability. Similarly, advances in fluorescent protein engineering have resulted in large number of wavelength tunable and highly efficient variants[130] of the original green fluorescent protein (GFP)[131].

Readout noise is common to all conventional image sensor architectures which make use of semiconductor-based amplifiers for image gain. High sensitivity flow cytometry was enabled in part by the development of the extremely low-noise, high-gain amplification process inherent to photomultiplier tubes (PMT). The operation of photomultiplier tubes is based on the photoelectric effect in which specially selected materials are highly efficient at converting incident photons into emitted electrons. In PMTs, a glass window to a vacuum tube is coated with such a material, referred to as the photocathode, and successively higher voltages are applied between staggered electrodes termed ‘dynodes’. Photoelectrons emitted from the photocathode are accelerated by this voltage toward the first dynode and strike it with increased kinetic energy resulting in the release of additional electrons through secondary emission. Each successive dynode further accelerates each batch of secondary electrons resulting in successive amplification of the total photocurrent. The process is extremely efficient and can amplify current with gain up to $10^8$. A similar semiconductor based approach to increasing low-noise gain in silicon photodiodes resulted in the development of the avalanche photodiode.[132] While the avalanche gain process is subject to higher readout noise than PMTs, photodiodes benefit from a higher quantum efficiency, particularly at longer wavelengths. The integration of avalanche gain principle into an imaging sensor, termed the electron multiplying CCD (or EM-CCD), was a major advance for low-light, high-speed imaging although it remains limited in resolution by the complexity of integrating the multi-stage avalanche gain mechanism on-sensor. The majority of commercially available EM-CCD cameras support a pixel resolution of 512×512 (*eg*. Evolve 512, Photometrics Inc. iXon3 897, Andor Technology) pixels although high resolution models are available up to 1024×1024 pixels (*eg*. Cascade II, Photometrics Inc. iXon3 888, Andor Technology). By comparison the current generation of scientific CMOS (often referred to as sCMOS) sensor-based cameras are available at resolutions of up to and exceeding 2048×2048 pixels (*eg.* Orca-Flash4.0, Hamamatsu Photonics. Zyla 4.2 & Zyla 5.5, Andor Technologies). Imaging resolution is also a function of the performance and design of the imaging optics, thus an appropriate camera resolution must be selected that accounts for the required maximum resolution, operating magnification and diffraction-limited performance of the optical system utilized.

### 1.5.2 Automation of image analysis

While the development of novel methods for automated image analysis is not a focus of this dissertation, a number of commonly used methods and tools in automating the segmentation and tracking of cells in fluorescence images are used and warrant discussion. The majority of image segmentation problems discussed in this dissertation made use of the open-source CellProfiler package developed at the Broad Institute at the Massachusetts Institute of Technology.[104] CellProfiler provides a set of configurable modules which can be chained together into processing pipelines and includes a number of common image processing, segmentation, tracking, and measurement algorithms. The core of CellProfiler's image segmentation algorithm is one of the most common workflows in the segmentation of fluorescence images of cells and consists of two steps: threshold and declump.

A wide variety of commonly used unsupervised thresholding algorithms have been exhaustively reviewed in the literature[133,134], each with their own advantages and disadvantages. In this dissertation, however, the one most commonly utilized was Otsu's method which attempts to cluster the pixels in an image into two or three classes by minimizing the variance of the pixel distributions within each class[135]. Thresholding a fluorescence image containing cells accomplishes a key step towards identifying cell boundaries and locations by demarking pixels comprising the image background from cellular fluorescence. In cases where fluorescence intensities vary from cell to cell or background values vary over the image, no optimal threshold may exist which can efficiently identify every cell within an image without inadvertently merging cells in contact or close proximity. In such cases it becomes necessary to use additional data from the image to identify the boundaries that separate adjacent cells within foreground-classified pixels.

One of the best studied algorithms for achieving this is the watershed transform which identifies ridges in image data that surround local minima.[136,137] The watershed transform can be used on a variety of measurements including the first or second order image gradient magnitude or object shape by computing the distance transform of thresholded foreground pixels. Each has its own advantages; the first order gradient watershed is most effective when there is sure to be a difference in image intensity at the boundary between adjacent cells, the second order gradient depends on the intensity of each cell decreasing as it approaches the boundary but is more sensitive to subtle differences in the magnitude of the intensity difference at the boundary and the distance transform is most effective when cells are of uniform shape and clusters are sufficiently sparse that curvature at cell boundaries is detectable in the thresholded image.

The combination of a well-selected threshold and watershed approach can achieve very high degrees of accuracy in segmenting clusters of cells from fluorescence images.[138] While algorithms exist which can improve performance beyond these levels, they typically come at the cost of significant increases in computational complexity and the difficulty of optimization. Well-trained shape models, for example, can achieve extremely high accuracies[139,140] but can be challenging to implement in systems where cellular morphology can vary significantly from cell to cell as is the case in the in-vitro culture of  cancer cell lines and dramatically increase computational complexity.

## 1.6 The scope of this dissertation

The work presented in this dissertation focuses on the development of an integrated imaging cytometry and cell sorting platform. Chapter 2 describes the development of a novel process for producing a magnetic photoresist to allow for the manipulation and micropallets and other microstructures using externally applied magnetic fields and has been published in the *Journal of Micromechanics and Microengineering*. Chapter 3 focuses on the development of the software required to automate two critical elements in the development of an integrated micropallet array sorting imaging cytometer: the capability to automate the imaging and localization of cells on micropallet arrays and to automate the micropallet release process. A manuscript based on the work described in Chapter 3 has been prepared and submitted for review. While automated image analysis is used heavily throughout Chapters 3 and 4, neither the development of novel image segmentation and classification approaches nor the complete optimization of existing algorithms were a goal of this dissertation. This is a direct consequence of one of the key advantages of micropallet array-based imaging cytometry and the additional challenges which emerge as a consequence. The broadened cell selection criteria and complex assays that are possible to perform using micropallet arrays require the integration of basic repeated image analysis tasks with customizable data analysis approaches. To streamline the development of new applications, a general-purpose image analysis tool (CellProfiler[104]) was utilized to automate generalizable tasks which primarily consisted of image segmentation. Segmented images were then processed using MATLAB scripts as necessitated by the specific application or assay that was being performed. Chapter 4 extends the capabilities described in Chapter 3 to a massively parallel clonogenic screening application. The goal of this work was to characterize the evolution of a reporter cell line commonly used in high throughput screens for the study of the Wnt/β-catenin pathway. The emergence of heterogeneity in cancer cell populations is a poorly understood process, although one that has garnered significant interest due to its implication in the development of resistance to chemotherapy. The characterization of small clonal colonies provides relatively weak statistical power in comparisons due to the inherently small sample sizes. In order to draw meaningful conclusions from such data a very large number of clones must be characterized, significantly larger than would be practical by limiting dilutions and conventional multi-well plate imaging. This application extends far beyond the capabilities of conventional cytometry modalities based on slide scanning or flow cytometry. This work has been prepared as a manuscript to be submitted for review.

## 1.7 Figures

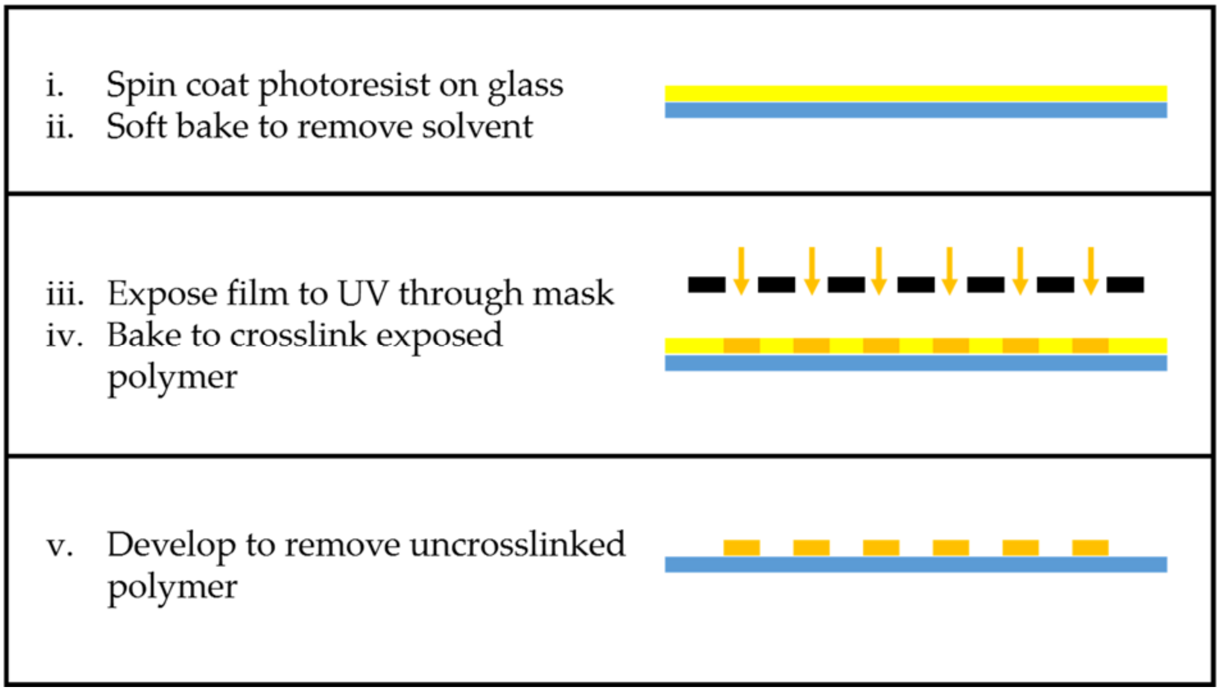

Figure 1.1. General fabrication scheme for micropallet arrays consisting of i. Generating a thin film of photoresist on a glass substrate by spin coating, ii. Soft baking the film to remove solvent, iii. Exposing the film to near UV light through a chrome mask pattern, iv. Baking the film to crosslink exposed portions of the film and v. Removal of uncrosslinked polymer by developing in 1-methoxy-2-propyl acetate.

## 1.8 References

1. Hudziak, R. M., Lewis, G. D., Winget, M., Fendly, B. M., Shepard, H. M. & Ullrich, A. *p185(HER2) monoclonal antibody has antiproliferative effects in vitro and sensitizes human breast tumor cells to tumor necrosis factor*. *Mol. Cell. Biol.* **9,** 1165–1172 (1989).

2. Druker, B. J., Tamura, S., Buchdunger, E., Ohno, S., Segal, G. M., Fanning, S., Zimmermann, J. & Lydon, N. B. Effects of a selective inhibitor of the Abl tyrosine kinase on the growth of Bcr–Abl positive cells. *Nat. Med.* **2,** 561–566 (1996).

3. Lamontanara, A. J., Gencer, E. B., Kuzyk, O. & Hantschel, O. Mechanisms of resistance to BCR-ABL and other kinase inhibitors. *Biochim. Biophys. Acta* **1834,** 1449–59 (2013).

4. Grunwald, M. R. & Levis, M. J. FLT3 inhibitors for acute myeloid leukemia: a review of their efficacy and mechanisms of resistance. *Int. J. Hematol.* **97,** 683–94 (2013).

5. Shou, J., Massarweh, S., Osborne, C. K., Wakeling, A. E., Ali, S., Weiss, H. & Schiff, R. Mechanisms of Tamoxifen Resistance: Increased Estrogen Receptor-HER2/neu Cross-Talk in ER/HER2-Positive Breast Cancer. *JNCI J. Natl. Cancer Inst.* **96,** 926–935 (2004).

6. Johnson, D. B. & Sosman, J. A. Update on the targeted therapy of melanoma. *Curr. Treat. Options Oncol.* **14,** 280–92 (2013).

7. Almendro, V., Marusyk, A. & Polyak, K. Cellular heterogeneity and molecular evolution in cancer. *Annu. Rev. Pathol.* **8,** 277–302 (2013).

8. Navin, N., Kendall, J., Troge, J., Andrews, P., Rodgers, L., McIndoo, J., Cook, K., Stepansky, A., Levy, D., Esposito, D., Muthuswamy, L., Krasnitz, A., McCombie, W. R., Hicks, J. & Wigler, M. Tumour evolution inferred by single-cell sequencing. *Nature* **472,** 90–4 (2011).

9. Navin, N. & Hicks, J. Future medical applications of single-cell sequencing in cancer. *Genome Med.* **3,** 31 (2011).

10. Yu, M., Bardia, A., Wittner, B. S., Stott, S. L., Smas, M. E., Ting, D. T., Isakoff, S. J., Ciciliano, J. C., Wells, M. N., Shah, A. M., Concannon, K. F., Donaldson, M. C., Sequist, L. V, Brachtel, E., Sgroi, D., Baselga, J., Ramaswamy, S., Toner, M., Haber, D. A. & Maheswaran, S. Circulating breast tumor cells exhibit dynamic changes in epithelial and mesenchymal composition. *Science* **339,** 580–4 (2013).

11. Tang, F., Barbacioru, C., Bao, S., Lee, C., Nordman, E., Wang, X., Lao, K. & Surani, M. A. Tracing the Derivation of Embryonic Stem Cells from the Inner Cell Mass by Single-Cell RNA-Seq Analysis. *Cell Stem Cell* **6,** 468–478 (2010).

12. Mortazavi, A., Williams, B. A., McCue, K., Schaeffer, L. & Wold, B. Mapping and quantifying mammalian transcriptomes by RNA-Seq. *Nat. Methods* **5,** 621–8 (2008).

13. Newman, J. R. S., Ghaemmaghami, S., Ihmels, J., Breslow, D. K., Noble, M., DeRisi, J. L. & Weissman, J. S. Single-cell proteomic analysis of S. cerevisiae reveals the architecture of biological noise. *Nature* **441,** 840–6 (2006).

14. Shi, Q., Qin, L., Wei, W., Geng, F., Fan, R., Shin, Y. S., Guo, D., Hood, L., Mischel, P. S. & Heath, J. R. Single-cell proteomic chip for profiling intracellular signaling pathways in single tumor cells. *Proc. Natl. Acad. Sci. U. S. A.* **109,** 419–24 (2012).

15. Irish, J. M., Kotecha, N. & Nolan, G. P. Mapping normal and cancer cell signalling networks: towards single-cell proteomics. *Nat. Rev. Cancer* **6,** 146–55 (2006).

16. Ponti, D., Costa, A., Zaffaroni, N., Pratesi, G., Petrangolini, G., Coradini, D., Pilotti, S., Pierotti, M. A. & Daidone, M. G. Isolation and in vitro propagation of tumorigenic breast cancer cells with stem/progenitor cell properties. *Cancer Res.* **65,** 5506–11 (2005).

17. Al-Hajj, M., Wicha, M. S., Benito-Hernandez, A., Morrison, S. J. & Clarke, M. F. Prospective identification of tumorigenic breast cancer cells. *Proc. Natl. Acad. Sci. U. S. A.* **100,** 3983–8 (2003).

18. Quintana, E., Shackleton, M., Sabel, M. S., Fullen, D. R., Johnson, T. M. & Morrison, S. J. Efficient tumour formation by single human melanoma cells. *Nature* **456,** 593–8 (2008).

19. Xu, X., Hou, Y., Yin, X., Bao, L., Tang, A., Song, L., Li, F., Tsang, S., Wu, K., Wu, H., He, W., Zeng, L., Xing, M., Wu, R., Jiang, H., Liu, X., Cao, D., Guo, G., Hu, X., Gui, Y., Li, Z., Xie, W., Sun, X., Shi, M., Cai, Z., Wang, B., Zhong, M., Li, J., Lu, Z.,

Gu, N., Zhang, X., Goodman, L., Bolund, L., Wang, J., Yang, H., Kristiansen, K., Dean, M., Li, Y. & Wang, J. Single-Cell Exome Sequencing Reveals Single-Nucleotide Mutation Characteristics of a Kidney Tumor. *Cell* **148,** 886–895 (2012).

20. Hou, Y., Song, L., Zhu, P., Zhang, B., Tao, Y., Xu, X., Li, F., Wu, K., Liang, J., Shao, D., Wu, H., Ye, X., Ye, C., Wu, R., Jian, M., Chen, Y., Xie, W., Zhang, R., Chen, L., Liu, X., Yao, X., Zheng, H., Yu, C., Li, Q., Gong, Z., Mao, M., Yang, X., Yang, L., Li, J., Wang, W., Lu, Z., Gu, N., Laurie, G., Bolund, L., Kristiansen, K., Wang, J., Yang, H., Li, Y., Zhang, X. & Wang, J. Single-Cell Exome Sequencing and Monoclonal Evolution of a JAK2-Negative Myeloproliferative Neoplasm. *Cell* **148,** 873–885 (2012).

21. Wang, W., Wyckoff, J. B., Frohlich, V. C., Oleynikov, Y., Huttelmaier, S., Zavadil, J., Cermak, L., Bottinger, E. P., Singer, R. H., White, J. G., Segall, J. E. & Condeelis, J. S. Single Cell Behavior in Metastatic Primary Mammary Tumors Correlated with Gene Expression Patterns Revealed by Molecular Profiling. *Cancer Res.* **62,** 6278–6288 (2002).

22. Sahai, E. & Marshall, C. J. Differing modes of tumour cell invasion have distinct requirements for Rho/ROCK signalling and extracellular proteolysis. *Nat. Cell Biol.* **5,** 711–9 (2003).

23. Heyn, C., Ronald, J. A., Ramadan, S. S., Snir, J. A., Barry, A. M., MacKenzie, L. T., Mikulis, D. J., Palmieri, D., Bronder, J. L., Steeg, P. S., Yoneda, T., MacDonald, I. C., Chambers, A. F., Rutt, B. K. & Foster, P. J. In vivo MRI of cancer cell fate at the single-cell level in a mouse model of breast cancer metastasis to the brain. *Magn. Reson. Med.* **56,** 1001–10 (2006).

24. Major, M. B., Roberts, B. S., Berndt, J. D., Marine, S., Anastas, J., Chung, N., Ferrer, M., Yi, X., Stoick-Cooper, C. L., von Haller, P. D., Kategaya, L., Chien, A., Angers, S., MacCoss, M., Cleary, M. A., Arthur, W. T. & Moon, R. T. New regulators of Wnt/beta-catenin signaling revealed by integrative molecular screening. *Sci. Signal.* **1,** ra12 (2008).

25. James, R. G., Biechele, T. L., Conrad, W. H., Camp, N. D., Fass, D. M., Major, M. B., Sommer, K., Yi, X., Roberts, B. S., Cleary, M. A., Arthur, W. T., MacCoss, M., Rawlings, D. J., Haggarty, S. J. & Moon, R. T. Bruton's tyrosine kinase revealed as a negative regulator of Wnt-beta-catenin signaling. *Sci. Signal.* **2,** ra25 (2009).

26. Berndt, J. D., Biechele, T. L., Moon, R. T. & Major, M. B. Integrative analysis of genome-wide RNA interference screens. *Sci. Signal.* **2,** pt4 (2009).

27. Chung, N., Marine, S., Smith, E. A., Liehr, R., Smith, S. T., Locco, L., Hudak, E., Kreamer, A., Rush, A., Roberts, B., Major, M. B., Moon, R. T., Arthur, W., Cleary, M., Strulovici, B. & Ferrer, M. A 1,536-well ultra-high-throughput siRNA screen to identify regulators of the Wnt/beta-catenin pathway. *Assay Drug Dev. Technol.* **8,** 286–94 (2010).

28. Durocher, Y., Perret, S., Thibaudeau, E., Gaumond, M. H., Kamen, A., Stocco, R. & Abramovitz, M. A reporter gene assay for high-throughput screening of G-protein-coupled receptors stably or transiently expressed in HEK293 EBNA cells grown in suspension culture. *Anal. Biochem.* **284,** 316–26 (2000).

29. Su, G. H., Sohn, T. A., Ryu, B. & Kern, S. E. A Novel Histone Deacetylase Inhibitor Identified by High-Throughput Transcriptional Screening of a Compound Library. *Cancer Res.* **60,** 3137–3142 (2000).

30. Conrad, C. & Gerlich, D. W. Automated microscopy for high-content RNAi screening. *J. Cell Biol.* **188,** 453–61 (2010).

31. Anderson, A. R. A., Weaver, A. M., Cummings, P. T. & Quaranta, V. Tumor Morphology and Phenotypic Evolution Driven by Selective Pressure from the Microenvironment. *Cell* **127,** 905–915 (2006).

32. Jones, C., Ford, E., Gillett, C., Ryder, K., Merrett, S., Reis-Filho, J. S., Fulford, L. G., Hanby, A. & Lakhani, S. R. Molecular cytogenetic identification of subgroups of grade III invasive ductal breast carcinomas with different clinical outcomes. *Clin. Cancer Res.* **10,** 5988–97 (2004).

33. Altschuler, S. J. & Wu, L. F. Cellular Heterogeneity: Do Differences Make a Difference? *Cell* **141,** 559–563 (2010).

34. Vindelov, L. L., Hansen, H. H., Christensen, I. J., Spang-Thomsen, M., Hirsch, F. R., Hansen, M. & Nissen, N. I. Clonal Heterogeneity of Small-Cell Anaplastic Carcinoma of the Lung Demonstrated by Flow-Cytometric DNA Analysis. *Cancer Res.* **40,** 4295–4300 (1980).

35. Litwin, V. Specificity of HLA class I antigen recognition by human NK clones: evidence for clonal heterogeneity, protection by self and non-self alleles, and influence of the target cell type. *J. Exp. Med.* **178,** 1321–1336 (1993).

36. Macdonald, H. R., Glasebrook, A. L., Bron, C., Kelso, A. & Cerottini, J.-C. Clonal Heterogeneity in the Functional Requirement for Lyt-2/3 Molecules on Cytolytic T Lymphocytes (CTL): Possible Implications for the Affinity of CTL Antigen Receptors. *Immunol. Rev.* **68,** 89–116 (1982).

37. Dalerba, P., Dylla, S. J., Park, I.-K., Liu, R., Wang, X., Cho, R. W., Hoey, T., Gurney, A., Huang, E. H., Simeone, D. M., Shelton, A. A., Parmiani, G., Castelli, C. & Clarke, M. F. Phenotypic characterization of human colorectal cancer stem cells. *Proc. Natl. Acad. Sci. U. S. A.* **104,** 10158–63 (2007).

38. Vermeulen, L., De Sousa E Melo, F., van der Heijden, M., Cameron, K., de Jong, J. H., Borovski, T., Tuynman, J. B., Todaro, M., Merz, C., Rodermond, H., Sprick, M. R., Kemper, K., Richel, D. J., Stassi, G. & Medema, J. P. Wnt activity defines colon cancer stem cells and is regulated by the microenvironment. *Nat. Cell Biol.* **12,** 468–76 (2010).

39. Cree, I. A., Glaysher, S. & Harvey, A. L. Efficacy of anti-cancer agents in cell lines versus human primary tumour tissue. *Curr. Opin. Pharmacol.* **10,** 375–379 (2010).

40. Marangoni, E., Vincent-Salomon, A., Auger, N., Degeorges, A., Assayag, F., de Cremoux, P., de Plater, L., Guyader, C., De Pinieux, G., Judde, J.-G., Rebucci, M., Tran-Perennou, C., Sastre-Garau, X., Sigal-Zafrani, B., Delattre, O., Diéras, V. & Poupon, M.-F. A new model of patient tumor-derived breast cancer xenografts for preclinical assays. *Clin. Cancer Res.* **13,** 3989–98 (2007).

41. Dong, X., Guan, J., English, J. C., Flint, J., Yee, J., Evans, K., Murray, N., Macaulay, C., Ng, R. T., Gout, P. W., Lam, W. L., Laskin, J., Ling, V., Lam, S. & Wang, Y. Patient-derived first generation xenografts of non-small cell lung cancers: promising tools for predicting drug responses for personalized chemotherapy. *Clin. Cancer Res.* **16,** 1442–51 (2010).

42. Taswell, C. Limiting dilution assays for the determination of immunocompetent cell frequencies. III. Validity tests for the single-hit Poisson model. *J. Immunol. Methods* **72,** 29–40 (1984).

43. Meissner, A., Wernig, M. & Jaenisch, R. Direct reprogramming of genetically unmodified fibroblasts into pluripotent stem cells. *Nat. Biotechnol.* **25,** 1177–81 (2007).

44. Kaji, K., Norrby, K., Paca, A., Mileikovsky, M., Mohseni, P. & Woltjen, K. Virus-free induction of pluripotency and subsequent excision of reprogramming factors. *Nature* **458,** 771–5 (2009).

45. Valenzuela, D. M., Murphy, A. J., Frendewey, D., Gale, N. W., Economides, A. N., Auerbach, W., Poueymirou, W. T., Adams, N. C., Rojas, J., Yasenchak, J., Chernomorsky, R., Boucher, M., Elsasser, A. L., Esau, L., Zheng, J., Griffiths, J. A., Wang, X., Su, H., Xue, Y., Dominguez, M. G., Noguera, I., Torres, R., Macdonald, L. E., Stewart, A. F., DeChiara, T. M. & Yancopoulos, G. D. High-throughput engineering of the mouse genome coupled with high-resolution expression analysis. *Nat. Biotechnol.* **21,** 652–9 (2003).

46. Shapiro, H. M. *Practical Flow Cytometry*. 736 (Wiley-Liss, 2003).

47. Chattopadhyay, P. K., Hogerkorp, C.-M. & Roederer, M. A chromatic explosion: the development and future of multiparameter flow cytometry. *Immunology* **125,** 441–449 (2008).

48. Bonner, W. A.; Hulett, H.R. ; Sweet, R.G. ; Herzenberg, L. A. Fluorescence Activated Cell Sorting. *Rev. Sci. Instrum.* **43,** 404 (1972).

49. Zheng, Y.-L., Demaria, M., Zhen, D., Vadnais, T. J. & Bianchi, D. W. Flow sorting of fetal erythroblasts using intracytoplasmic anti-fetal haemoglobin: Preliminary observations on maternal samples. *Prenat. Diagn.* **15,** 897–905 (1995).

50. Johnson, L. A., Flook, J. P., Look, M. V & Pinkel, D. Flow sorting of X and Y chromosome-bearing spermatozoa into two populations. *Gamete Res.* **16,** 1–9 (1987).

51. DeMaria, M. A., Zheng, Y. L., Zhen, D., Weinschenk, N. M., Vadnais, T. J. & Bianchi, D. W. Improved fetal nucleated erythrocyte sorting purity using intracellular antifetal hemoglobin and Hoechst 33342. *Cytometry* **25,** 37–45 (1996).

52. Xu, W., Sims, C. E. & Allbritton, N. L. Microcup arrays for the efficient isolation and cloning of cells. *Anal. Chem.* **82,** 3161–7 (2010).

53. Miltenyi, S., Müller, W., Weichel, W. & Radbruch, A. High gradient magnetic cell separation with MACS. *Cytometry* **11,** 231–8 (1990).

54. Herr, J. K., Smith, J. E., Medley, C. D., Shangguan, D. & Tan, W. Aptamer-conjugated nanoparticles for selective collection and detection of cancer cells. *Anal. Chem.* **78,** 2918–24 (2006).

55. Smith, J. E., Medley, C. D., Tang, Z., Shangguan, D., Lofton, C. & Tan, W. Aptamer-conjugated nanoparticles for the collection and detection of multiple cancer cells. *Anal. Chem.* **79,** 3075–82 (2007).

56. Talasaz, A. H., Powell, A. A., Huber, D. E., Berbee, J. G., Roh, K.-H., Yu, W., Xiao, W., Davis, M. M., Pease, R. F., Mindrinos, M. N., Jeffrey, S. S. & Davis, R. W. Isolating highly enriched populations of circulating epithelial cells and other rare cells from blood using a magnetic sweeper device. *Proc. Natl. Acad. Sci. U. S. A.* **106,** 3970–5 (2009).

57. Lantz, O. An invariant T cell receptor alpha chain is used by a unique subset of major histocompatibility complex class I-specific CD4+ and CD4-8- T cells in mice and humans. *J. Exp. Med.* **180,** 1097–1106 (1994).

58. Yang, D. -Defensins: Linking Innate and Adaptive Immunity Through Dendritic and T Cell CCR6. *Science (80-. ).* **286,** 525–528 (1999).

59. Stanciu, L. A., Shute, J., Holgate, S. T. & Djukanović, R. Production of IL-8 and IL-4 by positively and negatively selected CD4+ and CD8+ human T cells following a four-step cell separation method including magnetic cell sorting ( MACS). *J. Immunol. Methods* **189,** 107–115 (1996).

60. Yen, D., Cheung, J., Scheerens, H., Poulet, F., McClanahan, T., McKenzie, B., Kleinschek, M. A., Owyang, A., Mattson, J., Blumenschein, W., Murphy, E., Sathe, M., Cua, D. J., Kastelein, R. A. & Rennick, D. IL-23 is essential for T cell-mediated colitis and promotes inflammation via IL-17 and IL-6. *J. Clin. Invest.* **116,** 1310–6 (2006).

61. Paterlini-Brechot, P. & Benali, N. L. Circulating tumor cells (CTC) detection: Clinical impact and future directions. *Cancer Lett.* **253,** 180–204 (2007).

62. Riethdorf, S., Fritsche, H., Müller, V., Rau, T., Schindlbeck, C., Rack, B., Janni, W., Coith, C., Beck, K., Jänicke, F., Jackson, S., Gornet, T., Cristofanilli, M. & Pantel, K. Detection of circulating tumor cells in peripheral blood of patients with metastatic breast cancer: a validation study of the CellSearch system. *Clin. Cancer Res.* **13,** 920–8 (2007).

63. Sieben, S., Bergemann, C., Lübbe, A., Brockmann, B. & Rescheleit, D. Comparison of different particles and methods for magnetic isolation of circulating tumor cells. *J. Magn. Magn. Mater.* **225,** 175–179 (2001).

64. Molnar, B., Ladanyi, A., Tanko, L., Sreter, L. & Tulassay, Z. Circulating Tumor Cell Clusters in the Peripheral Blood of Colorectal Cancer Patients. *Clin. Cancer Res.* **7,** 4080–4085 (2001).

65. Allard, W. J., Matera, J., Miller, M. C., Repollet, M., Connelly, M. C., Rao, C., Tibbe, A. G. J., Uhr, J. W. & Terstappen, L. W. M. M. Tumor cells circulate in the peripheral blood of all major carcinomas but not in healthy subjects or patients with nonmalignant diseases. *Clin. Cancer Res.* **10,** 6897–904 (2004).

66. Taylor, P. Analytical and preparative instrumentation. *J. Biomol. Screen.* **18,** 143–5 (2013).

67. Ozkumur, E., Shah, A. M., Ciciliano, J. C., Emmink, B. L., Miyamoto, D. T., Brachtel, E., Yu, M., Chen, P., Morgan, B., Trautwein, J., Kimura, A., Sengupta, S., Stott, S. L., Karabacak, N. M., Barber, T. A., Walsh, J. R., Smith, K., Spuhler, P. S., Sullivan, J. P., Lee, R. J., Ting, D. T., Luo, X., Shaw, A. T., Bardia, A., Sequist, L. V, Louis, D. N., Maheswaran, S., Kapur, R., Haber, D. A. & Toner, M. Inertial focusing for tumor antigen-dependent and -independent sorting of rare circulating tumor cells. *Sci. Transl. Med.* **5,** 179ra47 (2013).

68. Gossett, D. R., Weaver, W. M., Mach, A. J., Hur, S. C., Tse, H. T. K., Lee, W., Amini, H. & Di Carlo, D. Label-free cell separation and sorting in microfluidic systems. *Anal. Bioanal. Chem.* **397,** 3249–67 (2010).

69. MacDonald, M. P., Spalding, G. C. & Dholakia, K. Microfluidic sorting in an optical lattice. *Nature* **426,** 421–4 (2003).

70. Mittal, S., Wong, I. Y., Deen, W. M. & Toner, M. Antibody-Functionalized Fluid-Permeable Surfaces for Rolling Cell Capture at High Flow Rates. *Biophys. J.* **102,** 721–730 (2012).

71. Phillips, J. A., Xu, Y., Xia, Z., Fan, Z. H. & Tan, W. Enrichment of cancer cells using aptamers immobilized on a microfluidic channel. *Anal. Chem.* **81,** 1033–9 (2009).

72. Sin, A., Murthy, S. K., Revzin, A., Tompkins, R. G. & Toner, M. Enrichment using antibody-coated microfluidic chambers in shear flow: model mixtures of human lymphocytes. *Biotechnol. Bioeng.* **91,** 816–26 (2005).

73. Li, Y., Dalton, C., Crabtree, H. J., Nilsson, G. & Kaler, K. V. I. S. Continuous dielectrophoretic cell separation microfluidic device. *Lab Chip* **7,** 239–48 (2007).

74. Huang, Y., Joo, S., Duhon, M., Heller, M., Wallace, B. & Xu, X. Dielectrophoretic Cell Separation and Gene Expression Profiling on Microelectronic Chip Arrays. *Anal. Chem.* **74,** 3362–3371 (2002).

75. Taff, B. M. & Voldman, J. A scalable addressable positive-dielectrophoretic cell-sorting array. *Anal. Chem.* **77,** 7976–83 (2005).

76. Valero, A., Merino, F., Wolbers, F., Luttge, R., Vermes, I., Andersson, H. & van den Berg, A. Apoptotic cell death dynamics of HL60 cells studied using a microfluidic cell trap device. *Lab Chip* **5,** 49–55 (2005).

77. Gao, Y., Bhattacharya, S., Chen, X., Barizuddin, S., Gangopadhyay, S. & Gillis, K. D. A microfluidic cell trap device for automated measurement of quantal catecholamine release from cells. *Lab Chip* **9,** 3442–6 (2009).

78. Zhu, L., Zhang, Q., Feng, H., Ang, S., Chau, F. S. & Liu, W.-T. Filter-based microfluidic device as a platform for immunofluorescent assay of microbial cells. *Lab Chip* **4,** 337–41 (2004).

79. Siciliano, P., Forleo, A., Chen, X., Cui, D. F., Liu, C. C. & Li, H. Microfluidic chip for blood cell separation and collection based on crossflow filtration. *Sensors Actuators B Chem.* **130,** 216–221 (2008).

80. Nagrath, S., Sequist, L. V, Maheswaran, S., Bell, D. W., Irimia, D., Ulkus, L., Smith, M. R., Kwak, E. L., Digumarthy, S., Muzikansky, A., Ryan, P., Balis, U. J., Tompkins, R. G., Haber, D. A. & Toner, M. Isolation of rare circulating tumour cells in cancer patients by microchip technology. *Nature* **450,** 1235–9 (2007).

81. Pamme, N. Continuous flow separations in microfluidic devices. *Lab Chip* **7,** 1644–59 (2007).

82. Huang, L. R., Cox, E. C., Austin, R. H. & Sturm, J. C. Continuous particle separation through deterministic lateral displacement. *Science* **304,** 987–90 (2004).

83. Gach, P. C., Attayek, P. J., Herrera, G., Yeh, J. J. & Allbritton, N. L. Isolation and in vitro culture of rare cancer stem cells from patient-derived xenografts of pancreatic ductal adenocarcinoma. *Anal. Chem.* **85,** 7271–8 (2013).

84. Nishimura, T., Miwa, J., Suzuki, Y. & Kasagi, N. Label-free continuous cell sorter with specifically adhesive oblique micro-grooves. *J. Micromechanics Microengineering* **19,** 125002 (2009).

85. Kuntaegowdanahalli, S. S., Bhagat, A. A. S., Kumar, G. & Papautsky, I. Inertial microfluidics for continuous particle separation in spiral microchannels. *Lab Chip* **9,** 2973–80 (2009).

86. Vogel, A., Horneffer, V., Lorenz, K., Linz, N., Hüttmann, G. & Gebert, A. Principles of Laser Microdissection and Catapulting of Histologic Specimens and Live Cells. *Methods Cell Biol.* **82,** 153–205 (2007).

87. Nelson, T., Tausta, S. L., Gandotra, N. & Liu, T. Laser microdissection of plant tissue: what you see is what you get. *Annu. Rev. Plant Biol.* **57,** 181–201 (2006).

88. Stich, M., Thalhammer, S., Burgemeister, R., Friedemann, G., Ehnle, S., Lüthy, C. & Schütze, K. Live Cell Catapulting and Recultivation. *Pathol. - Res. Pract.* **199,** 405–409 (2003).

89. Nakazono, M. Laser-Capture Microdissection, a Tool for the Global Analysis of Gene Expression in Specific Plant Cell Types: Identification of Genes Expressed Differentially in Epidermal Cells or Vascular Tissues of Maize. *PLANT CELL ONLINE* **15,** 583–596 (2003).

90. AHMED, F. E. Laser Microdissection: Application to Carcinogenesis. *Cancer Genomics Proteomics* **3,** 217–225 (2006).

91. Espina, V., Wulfkuhle, J. D., Calvert, V. S., VanMeter, A., Zhou, W., Coukos, G., Geho, D. H., Petricoin, E. F. & Liotta, L. A. Laser-capture microdissection. *Nat. Protoc.* **1,** 586–603 (2006).

92. Simone, N. L., Bonner, R. F., Gillespie, J. W., Emmert-Buck, M. R. & Liotta, L. A. Laser-capture microdissection: opening the microscopic frontier to molecular analysis. *Trends Genet.* **14,** 272–276 (1998).

93. Fend, F., Emmert-Buck, M. R., Chuaqui, R., Cole, K., Lee, J., Liotta, L. A. & Raffeld, M. Immuno-LCM: Laser Capture Microdissection of Immunostained Frozen Sections for mRNA Analysis. *Am. J. Pathol.* **154,** 61–66 (1999).

94. Banks, R. E., Dunn, M. J., Forbes, M. A., Stanley, A., Pappin, D., Naven, T., Gough, M., Harnden, P. & Selby, P. J. The potential use of laser capture microdissection to selectively obtain distinct populations of cells for proteomic analysis--preliminary findings. *Electrophoresis* **20,** 689–700

95. Nakazono, M. Laser-Capture Microdissection, a Tool for the Global Analysis of Gene Expression in Specific Plant Cell Types: Identification of Genes Expressed Differentially in Epidermal Cells or Vascular Tissues of Maize. *PLANT CELL ONLINE* **15,** 583–596 (2003).

96. Mayer, A., Stich, M., Brocksch, D., Schütze, K. & Lahr, G. Going in vivo with laser microdissection. *Methods Enzymol.* **356,** 25–33 (2002).

97. Ball, D. A., Marchand, J., Poulet, M., Baumann, W. T., Chen, K. C., Tyson, J. J. & Peccoud, J. Oscillatory dynamics of cell cycle proteins in single yeast cells analyzed by imaging cytometry. *PLoS One* **6,** e26272 (2011).

98. Chan, L. L., Zhong, X., Qiu, J., Li, P. Y. & Lin, B. Cellometer vision as an alternative to flow cytometry for cell cycle analysis, mitochondrial potential, and immunophenotyping. *Cytometry. A* **79,** 507–17 (2011).

99. Kamentsky, L. a & Kamentsky, L. D. Microscope-based multiparameter laser scanning cytometer yielding data comparable to flow cytometry data. *Cytometry* **12,** 381–7 (1991).

100. Kamentsky, L. A., Kamentsky, L. D., Fletcher, J. A., Kurose, A. & Sasaki, K. Methods for automatic multiparameter analysis of fluorescence in situ hybridized specimens with a laser scanning cytometer. *Cytometry* **27,** 117–25 (1997).

101. Kamentsky, L. A., Burger, D. E., Gershman, R. J., Kamentsky, L. D. & Luther, E. Slide-based laser scanning cytometry. *Acta Cytol.* **41,** 123–43

102. Edelstein, A., Amodaj, N., Hoover, K., Vale, R. & Stuurman, N. Computer control of microscopes using µManager. *Curr. Protoc. Mol. Biol.* **Chapter 14,** Unit14.20 (2010).

103. Abramoff, M. D., Magalhães, P. J. & Ram, S. J. Image processing with ImageJ. *Biophotonics Int.* **11,** 36–42 (2004).

104. Carpenter, A. E., Jones, T. R., Lamprecht, M. R., Clarke, C., Kang, I. H., Friman, O., Guertin, D. A., Chang, J. H., Lindquist, R. A., Moffat, J., Golland, P. & Sabatini, D. M. CellProfiler: image analysis software for identifying and quantifying cell phenotypes. *Genome Biol.* **7,** R100 (2006).

105. Cerignoli, F., Charlot, D., Whittaker, R., Ingermanson, R., Gehalot, P., Savchenko, A., Gallacher, D. J., Towart, R., Price, J. H., McDonough, P. M. & Mercola, M. High throughput measurement of Ca2+ dynamics for drug risk assessment in human stem cell-derived cardiomyocytes by kinetic image cytometry. *J. Pharmacol. Toxicol. Methods* **66,** 246–256 (2012).

106. Bartfeld, S., Hess, S., Bauer, B., Machuy, N., Ogilvie, L. A., Schuchhardt, J. & Meyer, T. F. High-throughput and single-cell imaging of NF-kappaB oscillations using monoclonal cell lines. *BMC Cell Biol.* **11,** 21 (2010).

107. Szaniszlo, P., Rose, W. A., Wang, N., Reece, L. M., Tsulaia, T. V, Hanania, E. G., Elferink, C. J. & Leary, J. F. Scanning cytometry with a LEAP: laser-enabled analysis and processing of live cells in situ. *Cytometry. A* **69,** 641–51 (2006).

108. Emmert-Buck, M. R., Bonner, R. F., Smith, P. D., Chuaqui, R. F., Zhuang, Z., Goldstein, S. R., Weiss, R. A. & Liotta, L. A. Laser Capture Microdissection. *Science (80-. ).* **274,** 998–1001 (1996).

109. Salazar, G. T., Wang, Y., Young, G., Bachman, M., Sims, C. E., Li, G. P. & Allbritton, N. L. Micropallet arrays for the separation of single, adherent cells. *Anal. Chem.* **79,** 682–7 (2007).

110. Campo, a Del & Greiner, C. SU-8: a photoresist for high-aspect-ratio and 3D submicron lithography. *J. Micromechanics Microengineering* **17,** R81–R95 (2007).

111. Gach, P. C., Sims, C. E. & Allbritton, N. L. Transparent magnetic photoresists for bioanalytical applications. *Biomaterials* **31,** 8810–7 (2010).

112. Benlarbi, M., Blum, L. J. & Marquette, C. A. SU-8-carbon composite as conductive photoresist for biochip applications. *Biosens. Bioelectron.* **38,** 220–5 (2012).

113. Xu, J. & Wong, C. P. High Dielectric Constant SU8 Composite Photoresist for Embedded Capacitors. 8–13 (2006). doi:10.1002/app

114. Shah, P. K., Hughes, M. R., Wang, Y., Sims, C. E. & Allbritton, N. L. Scalable synthesis of a biocompatible, transparent and superparamagnetic photoresist for microdevice fabrication. *J. Micromechanics Microengineering* **23,** 107002 (2013).

115. Cong, H. & Pan, T. Photopatternable Conductive PDMS Materials for Microfabrication. *Adv. Funct. Mater.* **18,** 1912–1921 (2008).

116. Jiguet, S., Bertsch, A., Judelewicz, M., Hofmann, H. & Renaud, P. SU-8 nanocomposite photoresist with low stress properties for microfabrication applications. *Microelectron. Eng.* **83,** 1966–1970 (2006).

117. Jiguet, S., Bertsch, a., Hofmann, H. & Renaud, P. Conductive SU8 Photoresist for Microfabrication. *Adv. Funct. Mater.* **15,** 1511–1516 (2005).

118. Li, T. & Hsu, S. L. Preparation and Properties of Conductive Silver / Photosensitive Polyimide Nanocomposites. 1575–1583 (2009). doi:10.1002/pola

119. Wang, Y., Bachman, M., Sims, C. E., Li, G. P. & Allbritton, N. L. Stability of virtual air walls on micropallet arrays. *Anal. Chem.* **79,** 7104–9 (2007).

120. Quinto-Su, P. a, To'a Salazar, G., Sims, C. E., Allbritton, N. L. & Venugopalan, V. Mechanisms of pulsed laser microbeam release of SU-8 polymer "micropallets" for the collection and separation of adherent cells. *Anal. Chem.* **80,** 4675–9 (2008).

121. Detwiler, D. A., Dobes, N. C., Sims, C. E., Kornegay, J. N. & Allbritton, N. L. Polystyrene-coated micropallets for culture and separation of primary muscle cells. *Anal. Bioanal. Chem.* **402,** 1083–91 (2012).

122. Shadpour, H., Sims, C. E., Thresher, R. J. & Allbritton, N. L. Sorting and expansion of murine embryonic stem cell colonies using micropallet arrays. *Cytometry. A* **75,** 121–9 (2009).

123. Pai, J.-H., Wang, Y., Salazar, G. T., Sims, C. E., Bachman, M., Li, G. P. & Allbritton, N. L. Photoresist with low fluorescence for bioanalytical applications. *Anal. Chem.* **79,** 8774–80 (2007).

124. Wang, Y., Young, G., Aoto, P. C., Pai, J.-H., Bachman, M., Li, G. P., Sims, C. E. & Allbritton, N. L. Broadening cell selection criteria with micropallet arrays of adherent cells. *Cytometry. A* **71,** 866–74 (2007).

125. Marmur, A. Wetting on Hydrophobic Rough Surfaces: To Be Heterogeneous or Not To Be? *Langmuir* **19,** 8343–8348 (2003).

126. Murphy, D. B. & Davidson, M. W. *Fundamentals of light microscopy and electronic imaging*. 538 p. (Wiley-Blackwell, 2013).

127. Giloh, H. & Sedat, J. Fluorescence microscopy: reduced photobleaching of rhodamine and fluorescein protein conjugates by n-propyl gallate. *Science (80-. ).* **217,** 1252–1255 (1982).

128. Berlier, J. E., Rothe, A., Buller, G., Bradford, J., Gray, D. R., Filanoski, B. J., Telford, W. G., Yue, S., Liu, J., Cheung, C.-Y., Chang, W., Hirsch, J. D., Beechem Rosaria P. Haugland, J. M. & Haugland, R. P. Quantitative Comparison of Long-wavelength Alexa Fluor Dyes to Cy Dyes: Fluorescence of the Dyes and Their Bioconjugates. *J. Histochem. Cytochem.* **51,** 1699–1712 (2003).

129. Loudet, A. & Burgess, K. BODIPY dyes and their derivatives: syntheses and spectroscopic properties. *Chem. Rev.* **107,** 4891–932 (2007).

130. Sullivan, K. F., Kay, S. A. & Haseloff, J. GFP Variants for Multispectral Imaging of Living Cells. *Methods Cell Biol.* **58,** 139–151 (1998).

131. Tsien, R. Y. The green fluorescent protein. *Annu. Rev. Biochem.* **67,** 509–44 (1998).

132. Bourgeois, P., El Mamouni, H., Goret, P., LeD&ucirc;, P., Limousin, O., Nédélec, P., Puill, V., Vanel, J. C. & Renker, D. Geiger-mode avalanche photodiodes, history, properties and problems. *Nucl. Instruments Methods Phys. Res. Sect. A Accel. Spectrometers, Detect. Assoc. Equip.* **567,** 48–56 (2006).

133. Glasbey, C. A. An Analysis of Histogram-Based Thresholding Algorithms. *CVGIP Graph. Model. Image Process.* **55,** 532–537 (1993).

134. Zhang, H., Fritts, J. E. & Goldman, S. A. Image segmentation evaluation: A survey of unsupervised methods. *Comput. Vis. Image Underst.* **110,** 260–280 (2008).

135. Otsu, N. A Threshold Selection Method from Gray-Level Histograms. *IEEE Trans. Syst. Man. Cybern.* **9,** 62–66 (1979).

136. Malpica, N., de Solórzano, C. O., Vaquero, J. J., Santos, a, Vallcorba, I., García-Sagredo, J. M. & del Pozo, F. Applying watershed algorithms to the segmentation of clustered nuclei. *Cytometry* **28,** 289–97 (1997).

137. Ng, H. P., Ong, S. H., Foong, K. W. C., Goh, P. S. & Nowinski, W. L. Medical Image Segmentation Using K-Means Clustering and Improved Watershed Algorithm. *2006 IEEE Southwest Symp. Image Anal. Interpret.* 61–65 (2006). doi:10.1109/SSIAI.2006.1633722

138. Coelho, L. P., Shariff, A. & Murphy, R. F. Nuclear segmentation in microscope cell images: A hand-segmented dataset and comparison of algorithms. *Proc. IEEE Int. Symp. Biomed. Imaging* **5193098,** 518–521 (2009).

139. Ivins, J. & Porrill, J. Active region models for segmenting medical images. in *Proc. 1st Int. Conf. Image Process.* **2,** 227–231 (IEEE Comput. Soc. Press).

140. Bamford, P. & Lovell, B. Unsupervised cell nucleus segmentation with active contours. *Signal Processing* **71,** 203–213 (1998).

# Chapter 2 Scalable synthesis of a biocompatible, transparent and superparamagnetic photoresist for microdevice fabrication

## 2.1 Introduction

The generation of nanocomposite photoresists with modified properties has dramatically expanded the toolbox available for the integration of active and passive components into microdevices. Nanocomposites have been developed to confer properties of ferro- and superparamagnetism for mechanically actuatable devices[1–5], conductivity for the integration of electrodes[6–9], high dielectric constants for integrated capacitors[10], low internal stress for improving mechanical properties[11] and a low index of refraction for the generation of on-chip optical waveguides[12]. These composites have typically relied upon the addition of insoluble components, often nanoparticles, into the photoresist. A common feature among nanocomposites incorporating metallic colloids is reduced accuracy in reproducing mask features, diminished fabrication quality and poor optical clarity. This undesirable optical property is generally due to an uneven distribution of the colloid in the photoresist as a result of aggregation. For biological applications where optical clarity is critical for analysis and imaging, transparent nanocomposite photoresists would prove valuable. Gach et al[1] demonstrated a method for dispersing iron oxide nanoparticles in photoresist that yielded high-fidelity, optically clear structures. This method, however, required high-intensity ultrasonication to prevent nanoparticle aggregation and was not amenable to production in large batches. In addition, the resulting photoresist was limited to aspect ratios of 4:1, offering no improvement in mechanical properties over the native 1002F photoresist it was based upon.[13]

To address these issues, we present a novel photoresist composite incorporating the epoxide-based photoresist 1002F and poly(methyl methacrylate-co-methacrylic acid) (PMMA/MMA). To test the photolithographic performance of the PMMA/1002F-based photoresist, arrays of microposts of varying diameters were fabricated and imaged by scanning electron microscopy (SEM). The dispersion of the maghemite nanoparticles in the PMMA/1002F composite was evaluated by imaging 100 nm-thick sections of the cross-linked composite by transmission electron microscopy (TEM). The spectral transmittance of the 0.25% (w/w) maghemite PMMA/1002F composite was measured by UV-Vis spectroscopy and the reaction of PMMA/MMA with the 1002F epoxy was confirmed by differential scanning calorimetry (DSC). The effect of the maghemite PMMA/1002F composite surface on cellular metabolism was tested by tracking the metabolic activity of HeLa cells over 72 h. Additionally, the compatibility of the composite surface with primary cell culture was evaluated by culturing murine mesenchymal stem cells for 72 h and observing cell morphology. The functionality of the magnetic composite was assessed by isolating single adherent cells cultured on an array of individually removable magnetic cell carriers.[14,15]

## 2.2 Materials and Methods

### 2.2.1 Synthesis of maghemite nanoparticles

A solution of 10-nm maghemite nanoparticles in toluene was prepared using the method described by Gach et al.[1] Iron salts (23.82 g $FeCl_2$ and 38.94 g $FeCl_3$ in 3 L of deionized (DI) water) were precipitated by the addition of a strong base (240 mL of 14.5 M $NH_4OH$), and washed three times with DI water by magnetic decantation. After resuspension in 480 mL of 1.5 M $HNO_3$, 104 g of $Fe(NO_3)_2$ was added to the solution which was then heated to boiling for 1 h. After cooling to 25 °C the precipitate was again washed by magnetic decantation once with 480 mL of 1.5 M $HNO_3$, once with 2500 mL of 0.1 M $NH_4OH$ and resuspended in 1500 mL of DI water. 90 g of oleic acid was added to the suspension and mixed for 15 minutes. The excess oleic acid and water were removed from the precipitate by three successive extractions with 200 mL of 100% ethanol. The precipitate was then dissolved in 800 mL of toluene and stored in amber glass bottles until use.

### 2.2.2 Composite preparation

Maghemite nanoparticles (3 g) were diluted with toluene (800 mL total volume). The weight percentage of maghemite nanoparticles in toluene was determined by evaporating solvent from a sample by heating at 120 °C for 30 min and weighing the dry solids. PMMA/MMA (100 g of methyl methacrylate:methacrylic acid at a molar ratio of 1:0.016, PMMA/MMA molecular weight =34,000, Sigma Aldrich, St. Louis, MO) was added to the nanoparticle solution and allowed to dissolve overnight while stirring. γ-butyrolactone (233.3 g) was added drop-by-drop using a separatory funnel and stirred further for an additional 24 h. The toluene in the solution was then removed by roto-evaporation at 60 °C leaving a deep red, highly viscous polymer suspension. The superparamagnetic PMMA/MMA solution was then added directly to 1002F-50 photoresist (1:2.6 by mass, PMMA/MMA:1002F-50) which had been prepared as previously described.[13] The mixture was then placed on a bottle roller for 4 days. The resulting PMMA/1002F photoresist was deep red in color.

### 2.2.3 Characterization of PMMA/1002F photoresist and magnetic composite

Melting point and glass transition temperatures were determined by DSC with a Q200 calorimeter (TA Instruments, New Castle, DE). 1002F and PMMA/MMA samples were analyzed as pure powders packed into the DSC sample pans. The PMMA/1002F was analyzed after 100 μL of the polymer suspension was baked into the sample pan at 120 °C for 72 h under vacuum to completely remove the solvent. For optical characterization, 50 μm thick films of 1002F photoresist, PMMA/1002F, and PMMA/1002F with 0.25% (w/w) maghemite nanoparticles were prepared by spin coating onto plasma-cleaned #2 glass coverslips. These films were treated as described below for micropallet fabrication before use except that no mask was used in producing UV-cross-linked films. Transmission spectra for triplicate preparations of each film were measured with a bare coverslip as a blank using a SpectraMax M5 spectrophotometer (Molecular Devices Corporation, Sunnyvale, CA). Working curves were generated by producing films of different thickness by varying the speed of the spin-coat step. The exposure needed to fully cross-link the films and form microstructures was then optimized and the final thickness of the film measured using a P-6 stylus profilometer (KLA Tencor, Milpitas, CA). The maximum aspect ratio of the PMMA/1002F with 0.25% maghemite nanoparticles composite was determined by fabricating a post-array using the protocol described below for fabrication of micropallet arrays. The fabricated structures were then imaged by SEM using a Quanta 200 environmental-SEM (FEI, Hillsboro, OR). The dispersion of maghemite nanoparticles into the PMMA/1002F photoresist was characterized by imaging transverse slices of a 50-μm thick film of the magnetic PMMA/1002F composite photoresist by TEM (JEOL 100CX II). The film was set in Polybed 812 resin and cured at 65 °C overnight. 100 nm thick sections of the film were cut with an ultramicrotome prior to imaging.

### 2.2.4 Cell culture and proliferation assay

Uniform films of PMMA/MMA, 1002F-50 and PMMA/1002F with 0.25% (w/w) maghemite nanoparticles as well as bare glass slides were treated with an air plasma (Harrick

Plasma, Ithaca, NY) for 5 min after being affixed to 4-well arrays fabricated from polylactic acid (PLA) with a benchtop 3D-printer (BFB-3000, Bits from Bytes Inc., Clevedon, UK). Polydimethylsiloxane (PDMS) was used to glue the wells to the surfaces. HeLa cells were plated in 3 of 4 wells of each array at a density of 2000 cells per well in 100 µL of culture media and cultured for 24, 48 or 72 h. Medium in each well was replaced every 24 h. A standard cell proliferation assay (MTT) was performed at multiple time points in accordance with the manufacturer's instructions (Life Technologies, Grand Island, NY). Briefly, 10 µL of 5 mg/mL (3-(4,5-dimethylthiazol-2-yl)-2,5-diphenyltetrazolium bromide (MTT) was added to each of 3 sample wells and one control well containing no cells and incubated at 37 º C for 4 h. MTT is metabolized by cells into an insoluble purple formazan which is then solubilized by the addition of 100 µL of 100 mg/mL sodium dodecyl sulfate (SDS) in 0.01 M HCl followed by incubation at 37 ºC for 4 h. 100 µL of fluid from each well was sampled and absorbance measurements were taken at 570 nm using a spectrophotometer. To test the compatibility of the composite with primary cell growth, mesenchymal stem cells (MSC) were derived from the long bone of a mouse[14] and plated on conventional tissue-culture dishes or films of the magnetic PMMA/1002F composite in Dulbecco's Modified Eagle Medium (DMEM) with 10% fetal bovine serum and cultured for 72 h.

### 2.2.5 Single-cell isolation by magnetic micropallet release

Micropallet arrays were fabricated according to previously reported protocols.[14-17] A 70 µm thick film of PMMA/1002F 0.25% (w/w) maghemite nanoparticles was spin coated onto 75×25 mm glass slides. The solvent was evaporated from the film by baking in a 95 °C oven for 60 min. The PMMA/1002F with 0.25% (w/w) maghemite nanoparticles required 7× higher exposure energies to fully cross-link the polymer as compared to similar features fabricated in native 1002F-50. Fabricated arrays were then treated with air plasma for 5 min prior to coating the arrays by low-pressure vapor deposition of (heptadecafluoro-1, 1, 2, 2-tetrahydrodecyl)trichlorosilane as previously described.[15]

The micropallet array was then glued with PDMS onto a cassette fabrictated from acrylonitrile butadiene styrene (ABS) by means of a 3-D printer. The PDMS was cured in a 70 °C oven for 30 min. Prior to use, the array was sterilized by rinsing with 70% ethanol and air-drying under a germicidal UV lamp for 30 min. The surface of the micropallet array was coated with fibronectin by incubating the array in 1 mL of 25 μg/mL fibronectin in phosphate-buffered saline (PBS) for 30 min at 25 °C. The array was then rinsed 3 times with PBS and finally immersed in Dulbecco's Modified Eagle Medium (DMEM) with 10% fetal bovine serum. A suspension of HeLa cells expressing GFP (10,000 cells in 3 mL) was added to each cassette and the cells were allowed to settle and adhere to the pallets overnight. The cells were imaged the following day, and cultured on the micropallet array for 2 additional days to allow clonal colonies to form. Prior to release, the micropallet cassette was mated to the bottom of a 47 mm diameter Petri dish (BD Biosciences, San Jose, CA) which had been treated with air plasma for 10 min and sterilized using the protocol described above. The magnetic collection experiment was carried out as described by Gach et al.[1] The clonal colonies were released by focusing a 5 ns pulse from an Nd:YAG laser at the photoresist-glass interface through a 20× , 0.7 N.A. objective and collected against gravity by a ring-shaped rare earth magnet (K&J Magnetics) placed on the collection plate. The cassette was designed to reduce the gap between the array and the collection plate to 3 mm. After collection, the Petri dish was removed from the cassette with the magnet, inverted and filled with an expansion media consisting of 50% FBS, 25% HeLa-GFP conditioned DMEM and

25% fresh DMEM. The conditioned media was generated by incubating 20 mL of fresh DMEM on a culture of HeLa cells on a 75 $mm^2$ tissue culture flask at 50% confluency for 24 hours. The conditioned media was then aspirated and filtered through a 0.22 µm nylon filter and stored at 4 °C for less than 72 h before use. The released clonal colonies were imaged again after 3 days to confirm their viability and to observe the expansion of the colony onto the Petri dish surface.

## 2.3. Results

### 2.3.1 Characterization of PMMA/1002F photoresists

Previous protocols to stably disperse maghemite nanoparticles into pure 1002F photoresist proved difficult to scale. Polymer additives were explored for their potential to stabilize the maghemite nanoparticles while forming a single phase with the photoresist. PMMA/MMA was selected as an additive to the 1002F photoresist system for its optical clarity, high glass transition temperature and the presence of acidic groups which could react with epoxides in the 1002F as well as stabilize the nanoparticles. The glass transition of PMMA/MMA occurred at 110 °C (Figure 2.1A). Un-crosslinked 1002F was observed to melt at 56.8 °C. When a mixture of PMMA/MMA and 1002F was heated from 40 °C to 140 °C, the material did not melt and a single glass transition was observed at 110 °C, supporting the conclusion that covalent bonds were formed between the 1002F and PMMA/MMA to form a single phase.

In order to maintain optical clarity for imaging and photolithographic fidelity, maghemite nanoparticles <20 nm in diameter were used to generate a magnetic photoresist. Oleic acid-capped nanoparticles rapidly aggregated when mixed directly into the GBL-based solutions of PMMA/MMA or 1002F and cured (Figure 2.1C). To prevent particle aggregation during solvent mixing, the PMMA/MMA was initially dissolved in toluene followed by addition of nanoparticles in the same solvent. GBL was then slowly introduced into this toluene-based solution. The magnetic nanoparticles remained dispersed in the solvent mixture and after evaporation of the toluene leaving the PMMA/MMA and nanoparticles dissolved in GBL alone. The PMMA/MMA/nanoparticle solution was then mixed into a solution of 1002F with GBL as the solvent. The nanoparticles showed no visible aggregation or phase separation after the composite photoresist was cured when examined by light microscopy (Figure 2.1D). When viewed by electron microscopy, the cross-linked magnetic PMMA/1002F composite possessed nanoparticle aggregates of 200 nm or less (Figure 2.1E). When examined by spectrophotometry, the cross-linked photoresist remained transparent at visible wavelengths greater than 500 nm (Figure 2.1B). The marked absorbance increase in the UV wavelengths resulted in a 4-fold increase in the exposure dose required for photolithography of the nonmagnetic PMMA/1002F photoresist and a 7-fold increase relative to that of 1002F photoresist. The 0.25% (w/w) maghemite PMMA/1002F composite showed no signs of visible aggregation or flocculation after more than 6 months of storage at room temperature in an amber glass bottle. The magnetic PMMA/1002F composite was produced in batches as large as 1 kg.

### 2.3.2 Photolithographic performance of PMMA/1002F photoresists

Previous reports of 1002F-based photoresists demonstrated an aspect ratio of 4:1.[14] Higher aspect ratios up to 20:1 have been demonstrated for SU-8, a related photoresist.[18] The maximum aspect ratio achievable by conventional UV photolithography with the PMMA/1002F photoresist was evaluated by preparing films of varying thickness and optimizing the total UV exposure energy through a test pattern containing circular holes ranging from 1 to 10 μm in diameter. When circular posts were fabricated, the PMMA/1002F composite with 0.25% (w/w) maghemite nanoparticles provided aspect ratios exceeding 10:1 (Figure 2.2C). The maghemite nanoparticle content of 0.25% (w/w) was selected as it was previously determined as the minimum weight percentage required to reliably collect release micropallets from a distance of greater than 2 mm.[1] The smallest feature successfully produced in these photoresists was 4 μm, the smallest diameter tested and a reasonable size limit for bioanalytical microdevices. The features shown (Figure 2.2C and D) were fabricated 3 months after the initial preparation of the maghemite PMMA/1002F composite demonstrating the long-term stability of the photoresist. The PMMA/1002F composite has been utilized with no apparent loss in performance up to 1 year after the initial preparation of the photoresist, comparable to the shelf life of commercially available SU-8 photoresist (13 months).

### 2.3.3 Cell culture on PMMA/1002F photoresist surfaces

Biocompatibility is an important consideration in selecting materials for fabricating microdevices for biological applications.[19,20] Data in the literature suggests that iron oxide nanoparticles can be cytotoxic.[21,22] A series of metabolic assays using MTT were performed over a 72-h period to assess the effects of the magnetic PMMA/1002F composite and its various components on cell growth and metabolism. Three substrates were prepared from each of the following, PMMA/MMA, PMMA/1002F, PMMA/1002F with 0.25% (w/w) maghemite particles, 1002F, and untreated glass. An MTT assay was performed on HeLa cells cultured on the substrates at 24, 48 and 72 h after seeding (Figure 2.3A). The PMMA/1002F with nanoparticles showed no statistically significant ($\alpha = 0.05$) effect on the growth and metabolism of these cells relative to a glass surface. Additionally, mesenchymal stem cells (MSC) derived from murine long bone grown on films of the magnetic PMMA/1002F composite displayed typical morphologies compared with that exhibited by cells grown in conventional tissue-culture dishes (Figure 2.3B).

### 2.3.4 Single-cell isolation using magnetic micropallet arrays.

Recent improvements in the sensitivity of molecular assays and growing recognition of the importance of heterogeneity in biological systems have highlighted the need for parallel improvements in single-cell isolation platforms.[23] Micropallet arrays have been demonstrated as an efficient platform for performing single-cell isolation from samples of varying size and diversity.[15-17] The use of a transparent, magnetic photoresist in the fabrication of micropallet arrays enables the facile collection of cells, preventing contamination with undesired cells and allowing multiplexed isolation by collecting released micropallets into microwell arrays.[1]

A cassette for single-cell isolation was developed by mating micropallet arrays fabricated superparamagnetic PMMA/1002F with polystyrene Petri dishes (Figure 2.4A). The upper lid of the Petri dish was used as a pallet-collection plate (Figure 2.4A). HeLa cells stably expressing a histone-H2B-GFP fusion protein were seeded onto an array of superparamagnetic micropallets (200 elements X 200 elements) coated with fibronectin, incubated at 37 °C overnight, and imaged (Figure 2.4B). After 2 d in culture, the individual cells expanded into clonal colonies on each micropallet (Figure 2.4C). After laser-based release, Selected micropallets with cells were released by a laser (n=5) and then collected onto the Petri dish lid by application of a magnetic force. The isolated colonies were followed over time and 100% of the colonies continued to proliferate with increased cell numbers (Figure 2.4D).

## 2.4. Conclusions

A highly scalable process for producing transparent, magnetic photoresist was developed enabling kilogram-sized batches to be synthesized. The resulting magnetic composite photoresist was capable of forming microstructures with aspect ratios greater than 10. Microstructures formed from the magnetic composite photoresist were highly transparent in the visible spectrum, were compatible with conventional fluorescence imaging and mammalian cell culture (including primary cell culture) and were used to fabricate magnetically active structures with demonstrated applications in single-cell isolation. The excellent optical and biological properties of the magnetic composite photoresist demonstrate its potential value for a wide variety of applications such as cell manipulation, the production of magnetic meta-materials, and fabrication of magnetically actuatable microsystems.

## 2.5 Figures

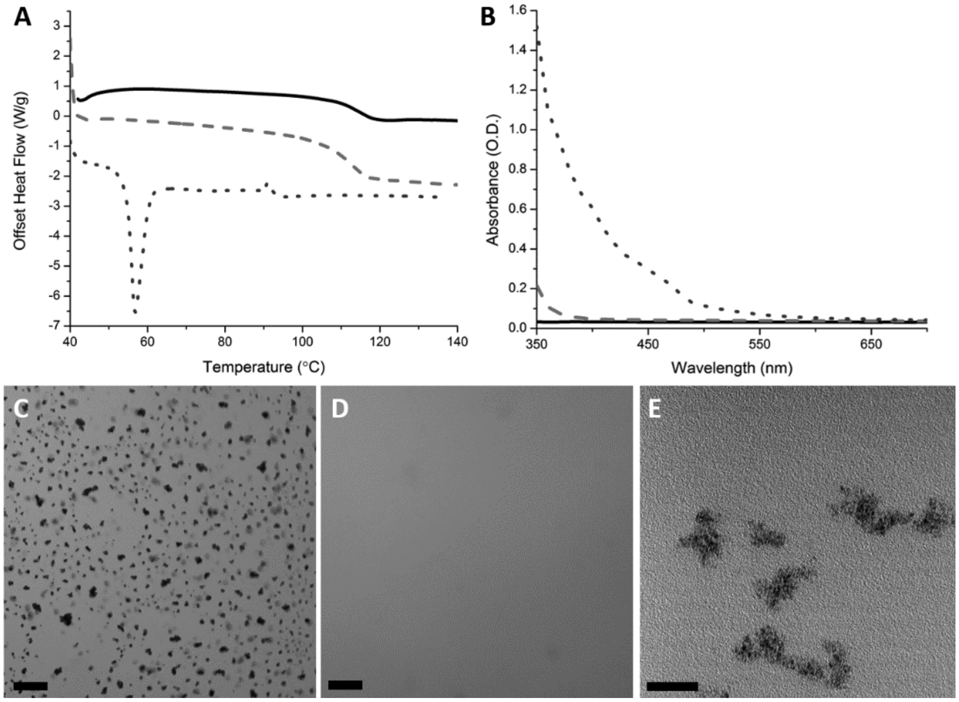

Figure 2.1 Properties of PMMA/1002F (A) Heat flow curves of PMMA/MMA (dashed line), 1002F (dotted line) and PMMA/1002F (solid line) photoresist as measured by differential scanning calorimetry while heating at a rate of 10 °C/min. The curves for PMMA/MMA and PMMA/1002F photoresist have been offset by 3 and 4.5 W/g, respectively. (B) Absorbance spectra of 50-µm thick films of PMMA/MMA (solid line), PMMA/1002F (dashed line) photoresist and PMMA/1002F with 0.25% (w/w) maghemite nanoparticles (dotted line). (C,D) Optical micrograph of a cured film produced from the direct addition of maghemite nanoparticles into 1002F photoresist (C) and of a film of PMMA/1002F with 0.25% (w/w) maghemite nanoparticles (D). The scale-bar is 50 µm. (E) TEM of a transverse slice of a cured film of PMMA/1002F with 0.25% (w/w) maghemite nanoparticles. The scale-bar is 100 nm.

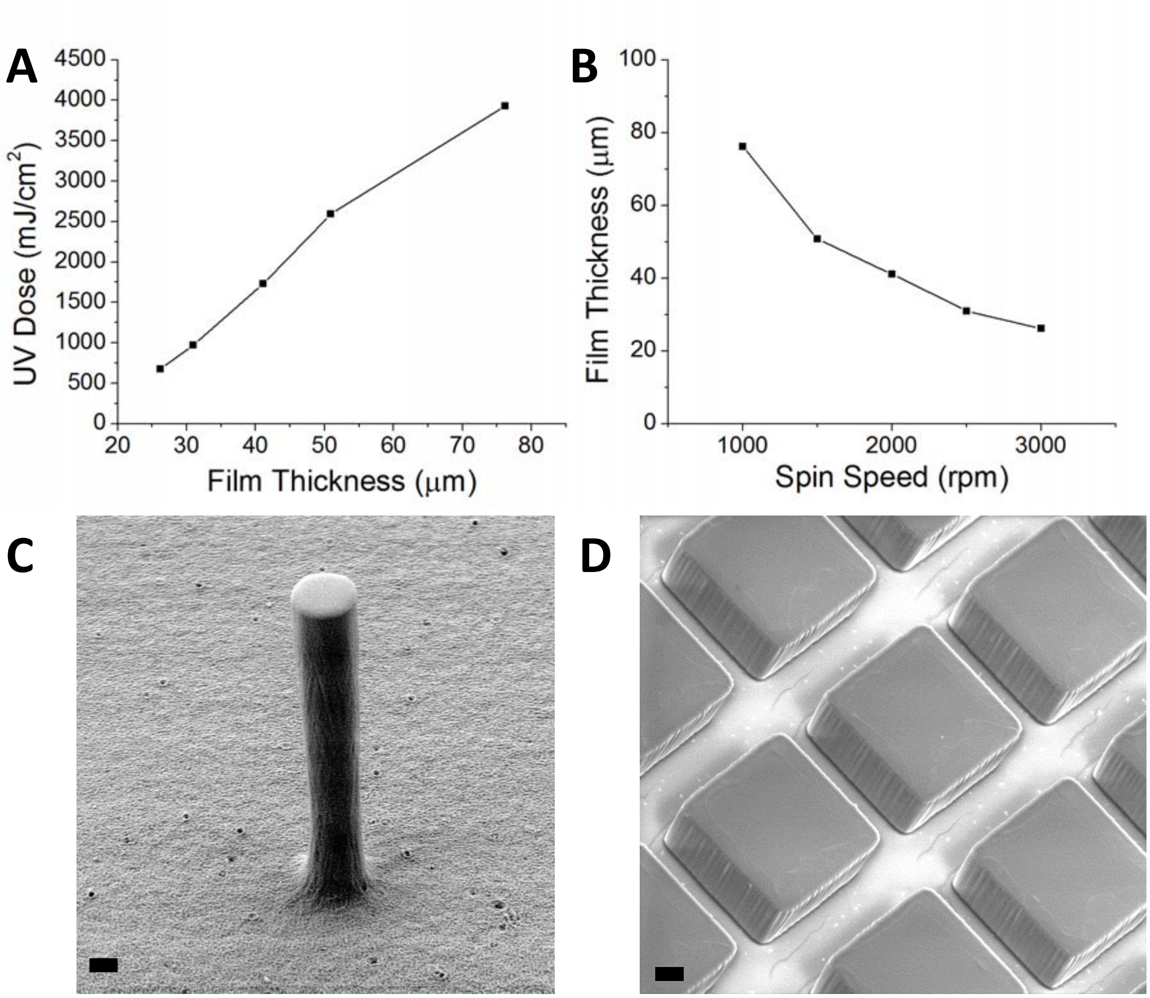

Figure 2.2. SEM micrographs of microstructures fabricated from PMMA/1002F photoresists. (A) Working curve showing required UV dose to cross-link films of PMMA/1002F with 0.25% (w/w) maghemite nanoparticles of varying thicknesses. (B) Relationship between spin speed and film thickness of PMMA/1002F with 0.25% (w/w) maghemite nanoparticles (N=3, error bars not visible). (C) Micropost (6×72 μm, diameter×height, aspect ratio = 12) fabricated from PMMA/1002F photoresist with 0.25% (w/w) maghemite nanoparticles. The scale-bar is 6 μm. (D) Arrays of micropallets (100×100×50 μm, L×W×H). The scale-bar is 10 μm.

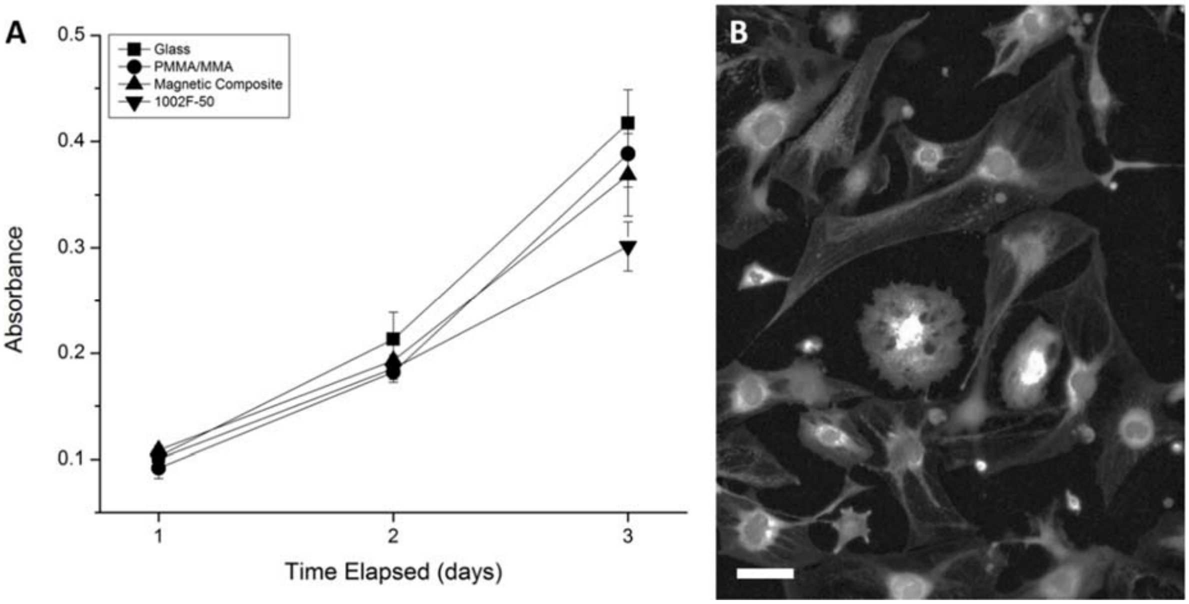

Figure 2.3. Biocompatibility of PMMA-containing photoresists. (A) Measurement of MTT metabolism by HeLa cells cultured on test substrates over 72 h. (B) Murine MSCs cultured on a film of PMMA/1002F with 0.25% (w/w) maghemite nanoparticles. The scale-bar is 100 μm.

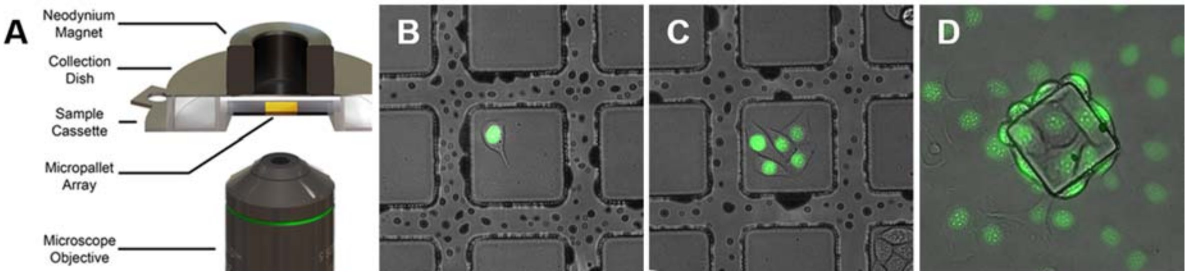

Figure 2.4. Workflow for micropallet isolation (A) Schematic of experimental setup for singe-cell isolation. Cells were loaded onto a micropallet array (each micropallet is 100×100×50 µm L×W×H) mounted in a cassette. A laser pulse focused at the photoresist-glass interface through a 0.7 N.A. objective was used to release individual micropallets from the array which were then attracted upward to the collection dish by the neodymium magnet. (B) A single HeLa cell possessing a fluorescent nucleus indicating expression of the histone-H2B-GFP fusion protein growing for 24 h on a micropallet array fabricated from the magnetic PMMA/1002F composite. (C) After 48 h in culture, the single cell expanded into a colony. (D) The micropallet in “C” shown 96 h after release and collection demonstrating that the colony continued to expand with cells migrating from the micropallet onto the collection well surface. Panels B-D are overlaid brightfield and fluorescence images.

## 2.6 References

1. Gach, P. C., Sims, C. E. & Allbritton, N. L. Transparent magnetic photoresists for bioanalytical applications. *Biomaterials* 31, 8810–7 (2010).

2. Damean, N., Parviz, B. a, Lee, J. N., Odom, T. & Whitesides, G. M. Composite ferromagnetic photoresist for the fabrication of microelectromechanical systems. *J. Micromechanics Microengineering* 15, 29–34 (2005).

3. Gunn, N. M., Chang, R., Westerhof, T., Li, G. P., Bachman, M., Nelson, E.L. Ferromagnetic micropallets for magnetic capture of single adherent cells. *Langmuir* 26, 17703–11 (2010).

4. Sakar, M. S., Steagar, E. B., Kim, D. H., Kim, M. J., Pappas, G. J., Single cell manipulation using ferromagnetic composite microtransporters. *Appl. Phys. Lett.* 96, 043705 (2010).

5. Suter, M., Graf, S., Ergeneman, O., Schmid, S., Camendzind, A., Nelson, B. J., & Hierold, C. Superparamagnetic photosensitive polymer nanocomposite for microactuators. *IEEE Transducers* 869–872 (2009).

6. Benlarbi, M., Blum, L. J. & Marquette, C. A. SU-8-carbon composite as conductive photoresist for biochip applications. *Biosens. Bioelectron.* 38, 220–5 (2012).

7. Cong, H. & Pan, T. Photopatternable Conductive PDMS Materials for Microfabrication. *Adv. Funct. Mater.* 18, 1912–1921 (2008).

8. Jiguet, S., Bertsch, a., Hofmann, H. & Renaud, P. Conductive SU8 Photoresist for Microfabrication. *Adv. Funct. Mater.* 15, 1511–1516 (2005).

9. Li, T. & Hsu, S. L. Preparation and Properties of Conductive Silver / Photosensitive Polyimide Nanocomposites. 1575–1583 (2009). doi:10.1002/pola

10. Xu, J. & Wong, C. P. High Dielectric Constant SU8 Composite Photoresist for Embedded Capacitors. 8–13 (2006). doi:10.1002/app

11. Jiguet, S., Bertsch, A., Judelewicz, M., Hofmann, H. & Renaud, P. SU-8 nanocomposite photoresist with low stress properties for microfabrication applications. *Microelectron. Eng.* 83, 1966–1970 (2006).

12. Ruano-López, J. M., Aguirregabiria, M, Tijero, M., Arroyo, M. T., Elizalde, J., Berganzo, J., Aranburu, I., Blanco, F. J., & Mayora, K. A new SU-8 process to integrate buried waveguides and sealed microchannels for a Lab-on-a-Chip. *Sensors Actuators B Chem.* 114, 542–551 (2006).

13. Zhu, H., Guo, Z. K., Jiang, X. X., Li, H., Wang, X. Y., Yao, H. Y., Zhang, Y., & Mao, N. A protocol for isolation and culture of mesenchymal stem cells from mouse compact bone. *Nat. Protoc.* 5, 550–60 (2010).

14. Pai, J. H., Wang, Y., Salazar, G. T., Sims, C. E., Bachman, M., Li, G. P., & Allbritton, N. L. Photoresist with Low Fluorescence for Bioanalytical Applications analytical devices. *Anal. Chem*. 79, 8774–8780 (2007).

15. Wang, Y., Sims, C. E., Marc, P., Bachman, M., Li, G. P., & Allbritton, N. L. Micropatterning of Living Cells on a Heterogeneously Wetted Surface. *Langmuir* 22, 8257–8262 (2006).

16. Wang, Y., Young, G., Bachman, M., Li, G. P., & Allbritton, N. L. Collection and expansion of single cells and colonies released from a micropallet array. *Anal. Chem.* 79 2359–66 (2007)

17. Wang, Y., Sims, C. E., Bachman, M., Li, G. P. & Allbritton, N. L. Micropatterning of living cells on a heterogeneously wetted surface *Langmuir* 22 8257–62 (2006)

18. Campo, a Del & Greiner, C. SU-8: a photoresist for high-aspect-ratio and 3D submicron lithography. *J. Micromechanics Microengineering* 17, R81–R95 (2007).

19. Walker, G. M., Zeringue, H. C. & Beebe, D. J. Microenvironment design considerations for cellular scale studies. *Lab Chip* 4, 91–7 (2004).

20. Voskerician, G., Shive, M. S., Shawgo, R. S., von Recum, H., Anderson, J. M., Cima, M. J., Langer, R. Biocompatibility and biofouling of MEMS drug delivery devices. *Biomaterials* 24, 1959–1967 (2003).

21. Brunner, T. J., Wick, P., Manser, P., Spohn, P., Grass, R. N., Limbach, L. K., Bruinink, A., & Stark, W. J. In Vitro Cytotoxicity of Oxide Nanoparticles: Comparison to Asbestos, Silica, and the Effect of Particle Solubility. *Environ. Sci. Technol.* 40, 4374–4381 (2006).

22. Pisanic, T. R., Blackwell, J. D., Shubayev, V. I., Fiñones, R. R. & Jin, S. Nanotoxicity of iron oxide nanoparticle internalization in growing neurons. *Biomaterials* 28, 2572–81 (2007).

23. Almendro, V., Marusyk, A. & Polyak, K. Cellular heterogeneity and molecular evolution in cancer. *Annu. Rev. Pathol.* 8, 277–302 (2013).

# Chapter 3: Small Sample Sorting of Primary Adherent Cells by Automated Micropallet Imaging and Release

## 3.1 Introduction

Improvements in the sensitivity of molecular characterization tools have driven advances in our appreciation of the role that cellular heterogeneity plays in human disease [1,2]. Little improvement has been seen, however, in techniques to prepare and process the small and often heterogeneous samples produced by in-vivo experiments and biopsies. While single-purpose microfluidic platforms exist for processing small samples [3], many researchers and clinicians still rely on manual and onerous cell and colony picking approaches [1,4]. A number of primary tissue sources pose significant challenges in yielding sufficiently large cell samples for conventional FACS sorting, often resulting in a need to pool tissue from a large number of organisms [5]. Primary patient samples remain the ideal for biomedical research, yet the cost and complexity of acquiring them as well as an inability to source uniform samples over the course of an investigation limits their utility. Patient-derived tumor xenografts (PDX) in nude mice fill this gap by providing a consistent source of tumor tissue from an in-vivo context that, while less scalable than conventional tissue culture techniques, better maintains the phenotype and gene expression patterns of the originating tumor [6–9]. Similar to patient samples, however, tumor biopsies and excisions from PDX mice are heterogeneous, having been infiltrated by murine immune, blood and vascular tissue [6], and are often limited in size.

Fluorescence activated cell sorting (FACS) remains the gold standard for high throughput cell sorting. Current generation FACS instruments are capable of measuring more than 20 parameters simultaneously [10] and achieve sort throughputs of greater than 50,000 cells/s [11] but are typically operated on the order of 1,000's of cells/s [12,13]. The use of hydrodynamically focused flow to generate a stream of single cells for analysis and sorting has several key disadvantages. Single point observation precludes repeated measurements of individual cells to track dynamic properties. Adherent cells must be detached from a tissue culture surface, significantly altering cell morphology and cytoskeletal organization which may perturb intracellular signaling [14–16]. Finally, the need to initialize sort gates combined with single point observation requires that a large number of cells be analyzed before a sort is possible, prohibitively decreasing the net effective sort yield for the very small samples that are typically obtained from primary tissue biopsies and small animal models [17]. Several variants of laser capture microdissection (LCM) have been demonstrated for sorting small samples of live cells including gravity assisted microdissection and laser pressure catapult microdissection [18]. Damage from the UV and IR lasers used in these approaches remains a concern [19]. As a consequence, manual cell picking and limiting dilution remain the most commonly used techniques for sorting such exceedingly small primary cell samples. These approaches are laborious, time-consuming and, in the case of limiting dilution, can consume significant quantities of reagents.

Micropallet arrays are an attractive and flexible platform for sorting and isolating cells from mixed samples [20]. They consist of arrays of transparent and individually releasable pedestals fabricated by single-step photolithography on a glass substrate [21]. Micropallets can be fabricated of various dimensions and array sizes optimized for sorting samples of varying size- from $10^2$ to $10^6$ cells [21,22]. The micropallets serve as culture sites for cells and function as cell carriers upon release from the array. Individual micropallets are released by focusing a low energy laser pulse at the photoresist-glass interface at high magnification and numerical aperture (20×, 0.7 N.A.) [23]. Treating the glass substrate with a fluorinated silane renders the gaps between adjacent micropallets hydrophobic, trapping air when submerged in buffer or media [24]. This trapped air, termed ‘virtual air walls’, prevents the migration of cells between adjacent micropallets. Additionally, the micropallets can be fabricated using a composite magnetic photoresist which enables the collection of micropallets against gravity by placing a permanent magnet above the array during laser release [25]. Previous applications of micropallet array technology depended upon time-consuming manual inspection of the array to identify cells of interest followed by the manually triggered release of target micropallets, limiting the throughput and accessibility of the technology [26,27].

Here we present an integrated platform for the automated imaging, analysis and release of micropallets from arrays. A software package was developed that supports rapid user initialization and automated multi-channel and multi-time-point imaging of uniform arrays of microstructures including, but not limited to, micropallet arrays, microraft arrays and microwell arrays. The package consists of two components: “Scan” and “Release” which incorporate the necessary functionality to allow for the identification of array elements bearing target cells and the release of identified target micropallets from the array. Scan throughput is a function of magnification and array geometry while release throughput is a function of the distance between targeted micropallets. The utility of the platform was demonstrated by sorting cells from very small samples (less than $10^4$ cells) obtained from PDX models of a pancreatic ductal adenocarcinoma and a liver metastasis of a colorectal carcinoma. Cell selection was based upon fluorescent staining of human EpCAM (CD326) which is expressed in colorectal cancers [28] and many pancreatic tumors [29].

## 3.2 Materials and Methods

### 3.2.1 Micropallet array fabrication

Micropallet arrays were fabricated using PMMA/1002F photoresist containing 0.25% (w/w) maghemite nanoparticles which had been prepared as previously described [25]. Briefly; a glass slide was coated with a 75 µm thick film of photoresist by spin coating in 2 steps: 10 s at 500 rpm followed by 30 s at 1,000 rpm. The photoresist film was baked to remove solvent at 95 °C for 1 h after which it was exposed to long-wave UV (360 nm longpass) for 6 min in 2 min intervals with 1 min between exposures to prevent sample heating. After exposure the photoresist was cross-linked by heating to 95 °C for 10 min and the unexposed photoresist was dissolved by developing in 1-methoxy-2-propyl acetate for 5-7 min, rinsed with 2-propanol and dried under a nitrogen stream. The resulting array was then cut to size in order to fit into a sample cassette which had been 3D printed out of acrylonitrile butadiene styrene (ABS) using a conventional extrusion-based printer (BFB-3000, Bits from Bytes Ltd, now 3D Systems Inc. Rock Hill, SC). The array was then oxidized in an air plasma (Harrick Plasma, Ithaca, NY) and reacted with (heptadecafluoro-1,1,2,2-tetrahydrodecyl) trimethoxysilane (Gelest Inc. Morrisville, PA) in a low-pressure chamber for 24 h to generate the virtual air walls as previously characterized [24]. After silanization the arrays were rinsed with 75% ethanol, dried under a stream of nitrogen and baked for 10 min on a 120 °C hot plate. The arrays were then glued into 3D printed cassettes with polydimethylsiloxane (PDMS) which was then cured for 30 min in a 70 °C oven. The glued cassettes were sterilized with 75% ethanol prior to use.

### 3.2.2 Automation of array scanning

An automated array scanning (process flow shown in Figure 3.1A) utility was implemented in the open-source, cross-platform Python programming language (Python

Software Foundation, python.org) with a user interface (Figure 3.1B) built using the Qt framework (Qt Project, qt-project.org). Microscope, stage and camera control libraries were provided by the open source microscopy control package Micro-Manager [30] through its Python interface. The microscope platform consisted of an inverted frame (Olympus IX81, Olympus Corporation of the Americas, Center Valley, PA), a motorized XY stage (MS-2000, Applied Scientific Instrumentation, Eugene, OR), a metal arc lamp excitation source (Lumen 200, Prior Scientific, Rockland, MA), high speed shutter (Lambda 10-2, Sutter Instrument Company, Novato, CA) and cooled interline CCD camera (CoolSnap HQ2, Photometrics, Tucson, AZ). For live-cell imaging, the microscope was enclosed in a custom fabricated black Delrin housing with temperature, humidity (AirTherm ATX-H, World Precision Instruments, Sarasota, FL) and $CO_2$ (Pro$CO_2$, BioSpherix, Lacona, NY) regulation.

Array scan automation was implemented in three steps: array geometry initialization, focus plane initialization, and array scanning. Array geometry initialization is a user-assisted process. The user inputs the general geometry of the array (the height and width of each element, the gap between each element and the number of rows and columns in the array) and positions the field-of-view at one corner of the array. A linear slider adjusts an intensity threshold which is applied to the image and the results overlaid on the video display, options are provided to limit the minimum and maximum object size as well as to close holes by mathematical morphology. The user identifies which corner of the array (top left, top right, bottom left or bottom right) is currently in the field of view. Based on the corner selected, three thresholded array elements are identified: the element closest in the image to the corner selected and the two elements closest to the adjacent corners of the image relative to the corner selected. The position of the corner element is stored and the vectors from the centroid of the corner element to the adjacent corners of the field of view are measured and used to estimate the position of the remaining three corners of the array. The user then selects one of two methods to measure the positions of the remaining corners: navigating to and measuring the position of the two corners adjacent to the first corner, or navigating to and measuring the position of the corner opposite of the first corner to be initialized.

The initialization process (adjust threshold, close holes and identify active corner) is repeated at each corner to confirm their positions after quickly seeking to their approximate position based on the estimate made during the initialization of the first corner. The initialization of the focus plane can be carried out before, after or simultaneously with the array geometry initialization. To initialize the focus plane, the user selects at least 4 positions in the array (recommended to be near the array corners) to manually focus on a cell present on the micropallet surface. After initialization, singular value decomposition (SVD) is used to calculate the normal vector of the plane of best fit that passes through the user-initialized point-cloud. The eigenvector with the smallest corresponding eigenvalue from the SVD of the point-cloud is selected as the normal vector used to calculate the equation of the plane of best fit which passes through the centroid of the point-cloud.

In the final step, discrete fields of view are identified beginning with the upper left corner of the array and providing full coverage of the array without dividing any elements between adjacent fields of view to prevent errors from inaccurate stitching. Each field of view is imaged sequentially based on the selected exposure, gain and filter positions and segmented into images of each individual element of the array present in the image based on their calculated positions from the array geometry initialization. A nested directory structure is generated for each time-point (if multiple are selected) containing separate folders for each channel to which are saved individual 16-bit grayscale tif images of each micropallet with its absolute row and column position within the array indicated in the image filename. The nested directory structure allows the use of a variety of common image analysis tools such as CellProfiler [31], ImageJ [32] and custom scripts implemented in MATLAB (The Mathworks Inc. Natick, MA).

### 3.2.3 Image analysis

Nuclear segmentation of PDX cells stained with Hoechst 33342 (Sigma Aldrich, St. Louis MO) was implemented using a CellProfiler pipeline. The image fluorescence background was estimated using a 40 pixel diameter grayscale opening operation and subtracted from the original image. A 3 × 3 pixel wide median smoothing filter was applied to the background-subtracted image to reduce over-segmentation of nuclei. A global two-class Otsu method was selected for automatic thresholding with an empirically tuned threshold correction factor and minimum threshold to adjust for variations in Hoechst staining and background fluorescence between arrays. CellProfiler's shape-based watershed method was used to declump nuclei. Finally, an attempt was made to reduce false positives from debris remaining in the sample after enrichment by filtering the segmented objects based on their size (10 – 40 pixel allowable diameter), maximum eccentricity (0.9) and an empirical threshold on the integrated fluorescence of the candidate nucleus (adjusted based on variations in staining intensity between experiments). An image mask was then generated from the filtered object list and saved to disk to be used by a custom MATLAB script to process the resulting data. The CellProfiler pipeline developed is provided in supplementary files. A MATLAB script was utilized to identify images containing a single cell as segmented by CellProfiler. The segmented masks were then dilated by 10 pixels and phycoerythrin (PE) fluorescence within the dilated neighborhood was integrated after background subtracting by grayscale opening (a 40 pixel diameter disk structuring element was used). The distribution of integrated PE fluorescence intensities was then displayed to the user and a threshold fluorescence was empirically selected based on the observed distribution and inspection of representative images of cells at different intensity values in the distribution. The row and column coordinates of cells that met both criteria (identification of a single nucleus by CellProfiler and greater than threshold fluorescence in the PE channel) were then exported into a plain text file to be read by the micropallet release utility.

### 3.2.4 Automation of micropallet release

Micropallet release was automated using a similar approach to scanning. First, a user initialized the array positions by locating two opposing or three adjacent corners of the array after inputting the array geometry into the release interface. A focus plane was also initialized using a minimum of 4 points to calculate a plane of best fit by SVD. This focus plane was initialized by the user at the base of the micropallets rather than their top surface as the laser must be focused at the glass-photoresist interface to effect micropallet release. Once the array positions and focal plane were initialized the user could either move to manually specified micropallets or load a list of target micropallets by their row and column coordinates. If a list of target micropallets was loaded, the release program successively moved to the position of each target micropallet, focus the 20× objective and trigger a 532 nm Nd:YAG pulse laser (Polaris, New Wave Research, Fremont, CA) to fire. The appropriate laser pulse energy to achieve reliable micropallet release varied from batch to batch and ranged from 5 to 8 µJ. An Arduino Uno microcontroller board (SparkFun Electronics, Boulder, CO) controlled with serial commands over USB by the Python release program was used to trigger the pulsed laser by delivering a 1 ms long 5 V pulse to the laser trigger input port. Fully automated release of a large number of micropallets was demonstrated by reproducing several images on micropallet arrays. This was achieved by converting the images into lists of target micropallets by down-sampling the image to the same number of rows and pixels as were present in the micropallet array, applying an empirical threshold to the resulting image and finding the row and column indices of every pixel with a value of 0 using a MATLAB script.

### 3.2.5 Micropallet array fabrication and collagen coating

Micropallet arrays were fabricated from a composite of poly(methylmethacrylate-co-methacrylic acid) (PMMA/MMA) and 1002F photoresist containing 0.25% (w/w) maghemite nanoparticles which had been prepared as previously described [25]. Arrays of 10,000 micropallets (100 × 100, rows × columns) measuring 100 × 100 × 35 µm (length × width × height) each were fabricated using spin coating, baking and UV exposure parameters that were previously identified. After fabrication, virtual air walls were generated by vapor coating the arrays with (heptadecafluoro-1,1,2,2-tetrahydrodecyl)-1-trichlorosilane in a low-pressure reactor for 16 h [24]. The silanized micropallet arrays were then glued into custom sample holders fabricated by 3D printing polylactic acid (PLA) on a fused deposition modeling printer (see above) with a small amount of polydimethylsiloxane (PDMS) which was cured for 30 min at 75 °C. After curing the glue, the array and cassette were sterilized by spraying with 75% ethanol and air drying.

After sterilization, the arrays were coated with collagen to promote PDX cell adhesion by a previously described physical deposition method [20]. Briefly, the arrays were incubated in 0.01% poly-L-lysine (Sigma-Aldrich, St. Louis, MO) at 25 °C for 16 h. Excess poly-L-lysine was removed by rinsing 3× with de-ionized water and replaced with a solution of 400 ng/mL of type I collagen from rat tail (Becton Dickinson, Franklin Lakes, NJ) and incubated at 25 °C for 1 min. The collagen solution was then aspirated from the array and the remaining droplets of the solution trapped on the hydrophilic micropallet surfaces were allowed to air-dry for 15 min. After drying, the collagen film was rendered insoluble by immersing in phosphate buffered saline (PBS; 137 mM NaCl, 10 mM $Na_2HPO_4$, 27 mM KCl, 1.75 mM $KH_2PO_4$, pH 7.4) and used within 24 h.

### 3.2.6 Patient-Derived Xenografts

Fresh tumor samples from pancreatic ductal adenocarcinoma and colorectal carcinoma patients were obtained under protocols approved by the University of North Carolina Institutional Review Board. The tumors were subcutaneously implanted into the flanks of immunocompromised mice and subsequently expanded and passaged, using protocols approved by the Institutional Animal Care and Use Committee. At the time of passage, a section of the tumor was cut into <3 mm pieces and rinsed with PBS containing penicillin and streptomycin (P/S). The tissue was minced with using the gentleMACS™ Dissociator (Miltenyi Biotec, Bergisch Gladbach, Germany) and incubated for 30 min in a 1 mg/ml collagenase/dispase (Roche 11097113001) solution. After incubation, mincing was repeated, the dissociation media was removed and the tissue was seeded as described below.

### 3.2.7 Culture and staining of PDX cells

PDX samples were received in suspension after enzymatic digestion and dissociation. After transport on ice, the samples were pelleted by centrifugation at 800 RCF for 2.5 min and resuspended in 5 mL of Dulbecco's Modified Eagle Medium (DMEM, Gibco® Life Technologies, Carlsbad, CA) supplemented with 10% fetal bovine serum (FBS, Thermo Scientific, Waltham, MA), 500 ng/mL gentamicin sulfate and 250 ng/mL amphotericin B (Life

Technologies, Carlsbad, CA). Due to the large amounts of tissue debris and dead cells generated from the PDX extraction and disaggregation, the samples were enriched by plating the suspension onto a 25 $cm^2$ tissue culture treated flask for 48 h to permit live cells to adhere. After 48 h, the cells were rinsed 3× with PBS to remove dead cells and debris and enzymatically released from the tissue culture surface (10 min at 37 °C in 0.05% Trypsin). The cells were then pelleted and re-suspended in 3 mL of culture medium of which 1 mL was plated onto the prepared collagen-coated micropallet array for staining, imaging and sorting.

After plating the suspension of PDX cells onto the collagen-coated micropallet array, the arrays were incubated for 48 h to allow the cells to attach. After 48 h, the arrays were rinsed 3× with PBS to remove remaining debris and dead cells and immersed in 37 °C extracellular buffer (ECB; 135 mM NaCl, 5 mM KCl, 1 mM MgCl2, 1 mM CaCl2, and 10 mM HEPES, pH 7.4). Hoechst 33342 (500 ng/mL) and PE-conjugated anti-CD326 (750 ng/mL, clone VU-1D9 mouse anti-human, Life Technologies, Carlsbad, CA) were added to the array and incubated at 37 °C for 15 min. The array was then rinsed 3× with fresh ECB and covered with an ethanol sterilized glass slide held 1 mm above the array surface by the sample cassette in direct contact with the ECB to maintain fluid contact during imaging and sorting.

### 3.2.8 Automated identification and sorting of EpCAM+ PDX cells

After initializing the array geometry and focus plane as described above, the array was scanned using DAPI and Texas Red filter cubes (Chroma Technology, Bellows Falls, VT). After scanning, the Hoechst fluorescence images were segmented by a CellProfiler pipeline and processed by a custom MATLAB script which then integrated fluorescence from the PE channel. An empirical threshold was determined based on the distribution of fluorescence intensities measured and direct inspection of representative raw images, and the coordinates (row and column number) of micropallets bearing a single cell with greater than threshold PE fluorescence were exported in a plain text file to be read by the release script. After initializing the release application, the target micropallet list was loaded and release of the first micropallet in the list was triggered manually to verify that laser focus and pulse energy were sufficient to effect release. The automated release program was then started and the video feed was observed throughout the process to confirm the successful release of each targeted micropallet. Released micropallets were collected using a magnet (K&J Magnetics, Pipersville, PA) placed above a collection plate overlaying the array. After the completion of the automated release, the collected micropallets were inspected to verify the retention of the targeted cell during micropallet release as well as its PE fluorescence.

## 3.3 Results

### 3.3.1 Automated array scanning

Micropallet array scanning was set up in 2 key steps: user initialization of the array geometry and user initialization of focus points in the array (Figure 3.1). Based on the geometry of the array (size and number of micropallets) and the user-initialized locations the array's corners, the scan system interpolated the position of every micropallet in the array. Autofocus was simplified by the planar nature of the top surface of the micropallet array- a plane of best fit was calculated by singular value decomposition from a set of user-initialized focus points distributed over the array. The plane-of-best fit reduced autofocus within the array to a look-up table problem, dramatically improving throughput over image-based autofocus solutions with typical errors (as compared to manual focus) smaller than the depth of field of a 20× objective (2.74 ± 1.37 μm, n=3). Scans could be configured over multiple time-points with up to 5 fluorescence channels per field of view. Each field of view was automatically segmented into images of the individual micropallets based on their interpolated positions and known geometry. The throughput of array scanning depended on 4 variables: field of view, dwell time, array geometry (element dimensions) and the travel time between adjacent fields of view. The travel time between adjacent fields of view was a function of the distance between adjacent fields of view and therefore magnification. At 10× magnification the travel time was 750 ms. The travel time could be reduced by increasing the acceleration of the stage, but this resulted in decreased positional accuracy and repeatability. For an array with 100 µm square elements and a 30 µm gap between adjacent elements, a single field of view at 10× magnification contained 35 elements. For a 500 ms dwell time at each field of view, the effective throughput was 28 elements/s and a 10,000 element array could be scanned in under 6 min per channel. Since the density of cell seeding onto arrays is governed by Poisson statistics, the maximization of single-cell occupancy of an array occurs at a ratio of 1 seeded cell per array element and corresponds to an average of 36.8% of micropallets possessing a single cell. This yielded an expected maximum theoretical scanning throughput of 10.3 cells/s at 10× magnification with a 500-ms dwell time. This throughput can be increased dramatically by reducing array element size since throughput is dependent on the cross-sectional area of each array element.

### 3.3.2 Automated micropallet release

The general workflow for automated micropallet release was very similar to that of micropallet array scanning with one key difference. Rather than initializing the focus plane at the top surface of the micropallets, the photoresist-glass interface was used as the focal plane since the laser pulse must be delivered at this interface to effect micropallet release. After initialization of the array geometry and focus plane, there were two modes of operation for release: manual and automated targeting. In manual operation the user could seek to specific row and column coordinates within the array and initiate release directly. In automated operation, the user loaded a plain text file containing a list of row and column numbers with commas separating the row and column and line breaks separating each targeted micropallet. The release utility then stepped through each position, focused the objective and fired the laser once to effect micropallet release (Figure 3.2A). Released micropallets were then attracted upwards to a collection plate by a ring-shaped permanent magnet placed above the array. To demonstrate the automated identification and release of a large number of targeted micropallets, a pattern was generated by releasing specific elements from micropallet arrays by processing a black and white image in MATLAB. The image was re-sized to contain the same number of pixels as micropallets were present in the array (200 rows × 200 columns, 40,000 elements or pixels total) and a list of the coordinates of pixels with value 0 was generated and used as the release input file (Figure 3.2B). The target list was then loaded into the release utility and the automated release process was initiated. A peak release throughput of 3 micropallets/s was achieved which was limited primarily by the time required for stage motion which was a function of the distance between subsequent micropallets targeted for release. Over 10,000 micropallets were released in each of the arrays to reproduce the graphical images on the micropallet array (Figure 3.2C). In all three examples shown, 100% of targeted micropallets were confirmed to have successfully released by visual inspection.

### 3.3.3 Automated identification of PDX cells on micropallet arrays

PDX cells were seeded onto micropallet arrays in suspension and allowed to adhere for 48 h. The arrays were then stained with Hoechst 33342 and PE-conjugated anti-EpCAM and imaged using the automated micropallet array scanning utility. Images from the Hoechst channel were segmented using CellProfiler and PE fluorescence was measured for micropallets that were identified as having only one cell. An empirical threshold for PE fluorescence was determined from the distribution of PE fluorescence intensity and by manually inspecting representative images to classify EpCAM+ cells. All micropallets identified as having a single EpCAM+ cell were released from their respective arrays using the automated release utility.

In total, three PDX samples were analyzed and sorted using the automated system. Two PDX samples were derived from the same patient tumor: a liver metastasis of a colorectal carcinoma (CRC1 and CRC2) but cultured in different mice. The third PDX sample originated from a pancreatic ductal adenocarcinoma (PDAC) and yielded 8× as many total cells per volume of sample as either the CRC1 or CRC2 samples. A total of 7,584 cells were identified on the array seeded from PDAC whereas the CRC1 and CRC2 arrays possessed 875 and 1087 cells, respectively. In total, 1,750 (PDAC), 403 (CRC1) and 764 (CRC2) micropallets were identified as containing a single cell.

To evaluate the accuracy of the segmentation pipeline for each of the three samples, 100 randomly selected micropallets were manually inspected from the population to determine whether the image analysis pipeline correctly identified a single cell. In addition, 100 randomly selected micropallets identified as containing no cells were also manually inspected to confirm the absence of cells. From the micropallets that were identified as bearing a single cell, the false positive rate (FPR) was determined to be 0%, 9% and 8% for PDAC, CRC1 and CRC2, respectively. For both CRC samples, looser criteria to filter potential single cells were used to maximize the number of EpCAM+ cells identified due to the significantly lower total number of cells available in the sample. As a consequence, however, this resulted in a higher FPR due to the misclassification of fluorescent debris and light scatter from micropallet edges. 6% of the micropallets identified from PDAC as having a single cell were found to be undersegmented and contained 2 nuclei, although it was not clear what fraction of these were true doublets as opposed to single multinucleated cells. For the micropallets identified as containing no cells, only a single micropallet from the PDAC image set was identified as being a false negative, resulting in a false negative rate (FNR) of 1% for PDAC and 0% for both CRC1 and CRC2, and an aggregate FNR of 0.33%.

After identifying micropallets containing single cells, the PE fluorescence of each cell was measured by a MATLAB script which integrated pixel values in the PE channel image within a 10-pixel radius of the segmented images produced by CellProfiler. The distribution of the number of cells per micropallet is shown in Figure 3.3A-C. Of the micropallets identified as containing a single cell, 257 (14.7%, PDAC), 7 (1.7%, CRC1) and 16 (2.1%, CRC2) micropallets were determined to contain a single EpCAM+ cell based on the empirically determined thresholds identified from the distributions shown in Figure 3.3D-F. Differences in the percentage of EpCAM+ cells are believed to be due to variations in the degree of infiltration of host stromal tissue into the xenograft tumor while the total number of live cells isolated likely depended on the relative size of each tumor as well as the degree of necrosis and fibrosis present.

### 3.3.4 Sorting EpCAM+ PDX cells from host tissue contamination

All micropallets with a single EpCAM+ cell on the arrays seeded with the CRC1, CRC2 and PDAC PDX samples were released and collected using the automated micropallet release utility. The largest scale release, 257 micropallets from the array seeded by the PDAC PDX, sample completed in 3.75 min and achieved a mean throughput of 1.14 cells/s. The release of 7 cells from the CRC1 array and 16 cells from CRC2 array achieved much lower effective throughputs due to the greater distance between adjacent targeted micropallets and required 25 s and 42 s to complete, respectively. The automated release process was monitored visually for all three arrays and 99.6% of all micropallets that were targeted for release were successfully released. The single micropallet that failed to release from the CRC2 array was observed to be trapped by a thick layer of collagen gel due to a defect produced during the coating process. The purity and yield of each sort was confirmed by directly inspecting collected micropallets. For the micropallets released from the PDAC array, a subset of 17 collected micropallets were re-imaged (Figure 3.4). Two micropallets were observed to each have two nuclei present (and presumably two cells). One micropallet was observed that was collected without a cell attached. All cells on these micropallets were EpCAM+ resulting in a purity of 100%. The yield for correctly identified and collected pallets with a single PDAC EpCAM+ cell was 82% (14 of 17). For CRC1 and CRC2, all 7 and 15 successfully released micropallets were confirmed to have been collected. All 7 micropallets collected from the CRC1 sample were observed to carry a single, EpCAM+ cell, resulting in 100% yield and purity. For CRC2, all collected cells were EpCAM+ indicating 100% purity. However, a single micropallet possessed two nuclei resulting in a net yield of 93% *i.e.*14 of 15 micropallets correctly possessed a single EpCAM+ cell following collection.

## 3.4 Discussion

In this study, we describe the integration of the micropallet-array technology with an automated microscopy platform to enable flexible analysis and sorting of very small primary tissue samples. A software package was developed with a graphical interface that permits rapid and easy array configuration and imaging. At 10× magnification, an overhead of 750 ms was necessary for stage motion, image acquisition and writing the acquired images to disk per field-of-view. A single channel scan over an array of 10,000 micropallets (100 × 100 μm) with a

500 ms dwell time for each field-of-view was completed in under 6 min with less than 2 min typically required for the initial set-up of the scan. Since the seeding of cells onto micropallet arrays is described by Poisson statistics, an average of 36.79% of micropallets in an array are expected to contain a single cell and therefore an ideally seeded array of similar geometry would achieve a mean imaging throughput of 10.3 cells/s. While this aggregate throughput is lower than that possible by imaging cells seeded at higher densities on a planar or arrayed surface, micropallet arrays enable these cells to be sorted based on both image measurements and temporal criteria, dramatically expanding the selection criteria that can be used (13). Furthermore, the retention of adherent cells seeded onto the micropallet array surface enables extremely small samples to be sorted with higher yield than existing automated solutions [17] and significantly faster than manual approaches such as limiting dilution or cell picking.

Increased use of cytogenetics in clinical oncology and cancer research [33–35] has highlighted a need for advances in cell selection, enrichment and purification techniques compatible with the often heterogeneous and small samples that can readily be obtained from patient biopsies and animal models. To demonstrate the ability of micropallet array technology to characterize and sort small working samples, a proof-of-concept was implemented using PDX models of pancreatic and colorectal cancers. Samples acquired from the tumors used exhibit differing levels of purity due to the variable infiltration of tumor cells with that of the murine host tissue. The high cost of maintaining PDX mouse colonies, the relatively short usable lifespan of a xenograft (recommended <10 passages[6]) and the need to minimize the number of animals sacrificed lend significant value to the ability to increase the number of experiments that can be performed from each PDX. The proof-of-concept sort was performed with initial sample sizes ranging from 875 to 7,584 cells. Three samples were ultimately sorted with a mean yield of 90% and purity of 100%. This performance greatly exceeded previously published attempts with MACS and FACS to sort similarly sized samples in both effective yield and purity (for $10^3$ cells, FACS: 0% yield, MACS: 14% purity, 30% yield)[17]. The integration of the micropallet sorting automation with automated imaging and image analysis also enables applications requiring a time-series or morphological data from adherent cells, selection criteria for which no alternatives exist in either MACS or FACS. Previous studies with micropallet array-based sorting have also demonstrated very high rates of post-sort viability [21,36,37]. As a single laser-pulse is required per released micropallet, the potential exists for the development of instruments with significantly higher sorting throughput than LCM-based live-cell sorting technologies.

## 3.5 Figures

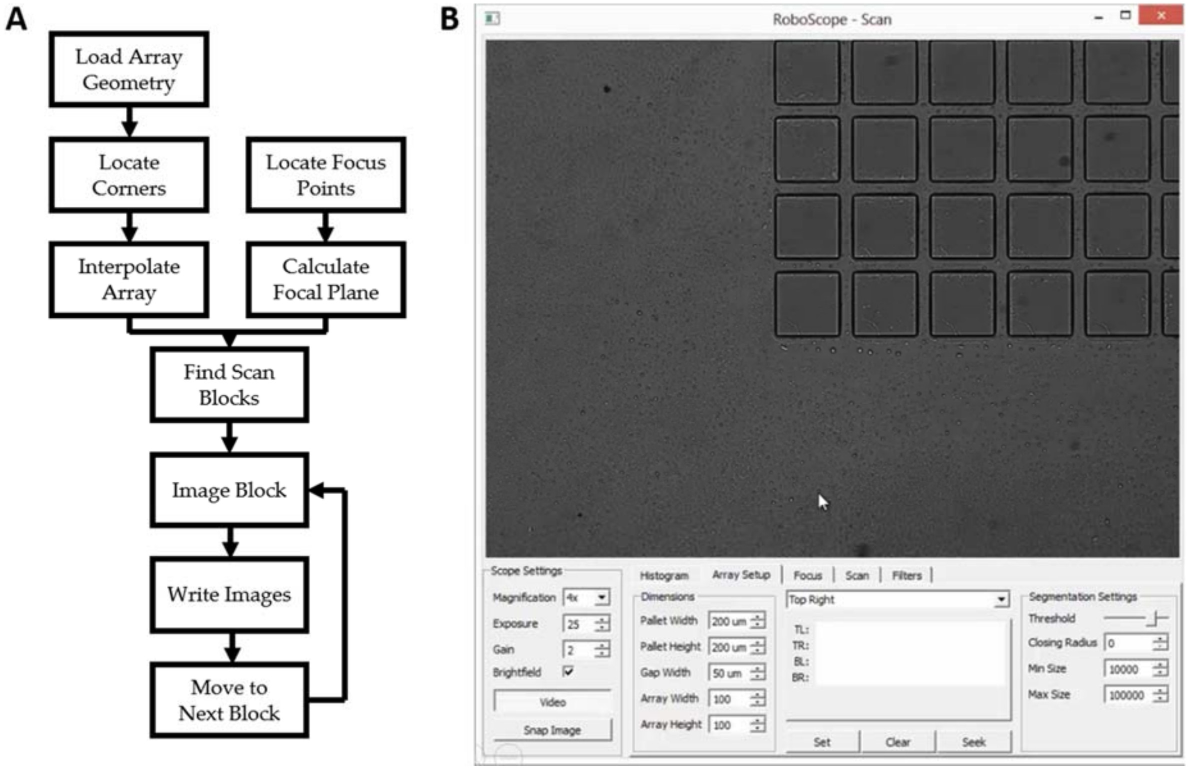

Scope Settings
Magnification: 4x
Exposure: 25
Gain: 2
Brightfield: ☑

Dimensions
Pallet Width: 200 um
Pallet Height: 200 um
Gap Width: 50 um
Array Width: 100
Array Height: 100

Top Right
TL:
TR:
BL:
BR:

Segmentation Settings
Threshold
Closing Radius: 0
Min Size: 10000
Max Size: 100000

Figure 3.1. Overview of micropallet array scan automation (A) The process flow by which the implemented utility scans over micropallet arrays. The two initial steps (Load Array Geometry and Locate Focus Points) were user-assisted, following which the initialized array could be scanned in a fully automated fashion. (B) A screenshot of the Scan utility user interface showing image acquisition settings as well as the panel for configuring the micropallet array geometry.

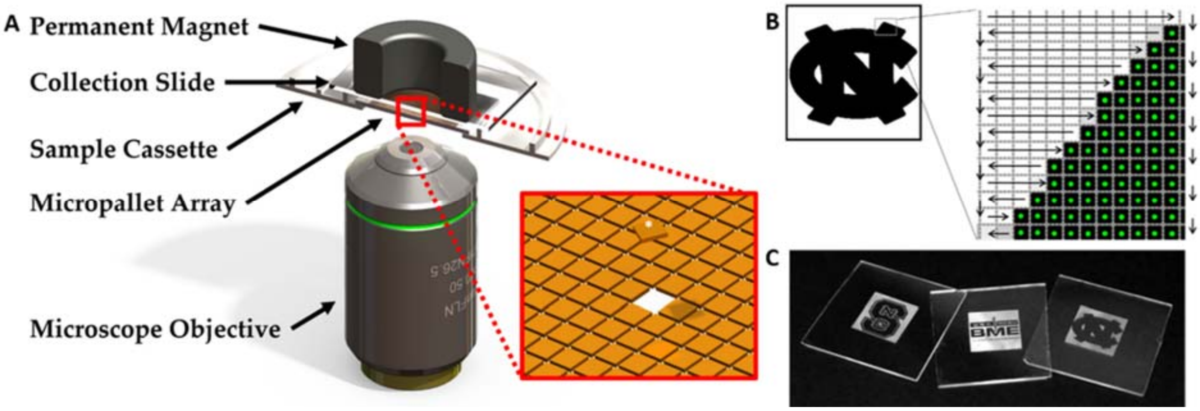

Figure 3.2. Overview of micropallet release automation (A) Schematic rendering of micropallet array experimental setup showing an array mounted in a 3D-printed cassette with a glass slide and permanent magnet placed on the cassette for micropallet collection after release. The inset shows an expanded view of the micropallet array. The white asterisk marks a released and collected micropallet. (B) A graphical representation of the process by which target micropallets are located through a list generated from a “mask” of the array pixel-by-pixel. The release utility sequentially steps through the target list and fires a laser pulse at each micropallet. (C) Examples of micropallet arrays (50 µm cube micropallets, 200 × 200 micropallets per array) from which large numbers of micropallets were released in an automated fashion (>10,000). The target lists were generated from mask images with the same number of pixels as micropallets present in the array.

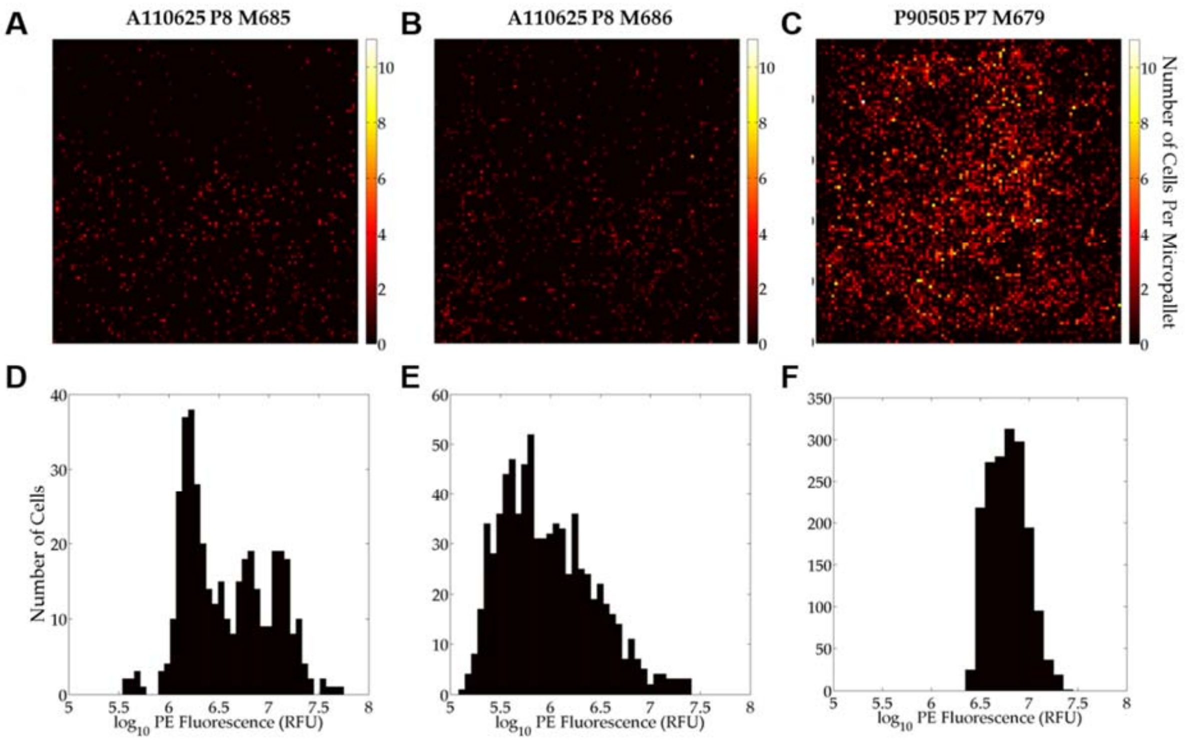

Figure 3.3. Image analysis of PDX samples (A-C) Heat-maps showing the number of PDX cells identified on each micropallet in the array (each pixel corresponds to a single micropallet) by CellProfiler. (D-F) Histograms of the log-transformed integrated PE fluorescence (marking EpCAM) for each micropallet identified as containing a single-cell.

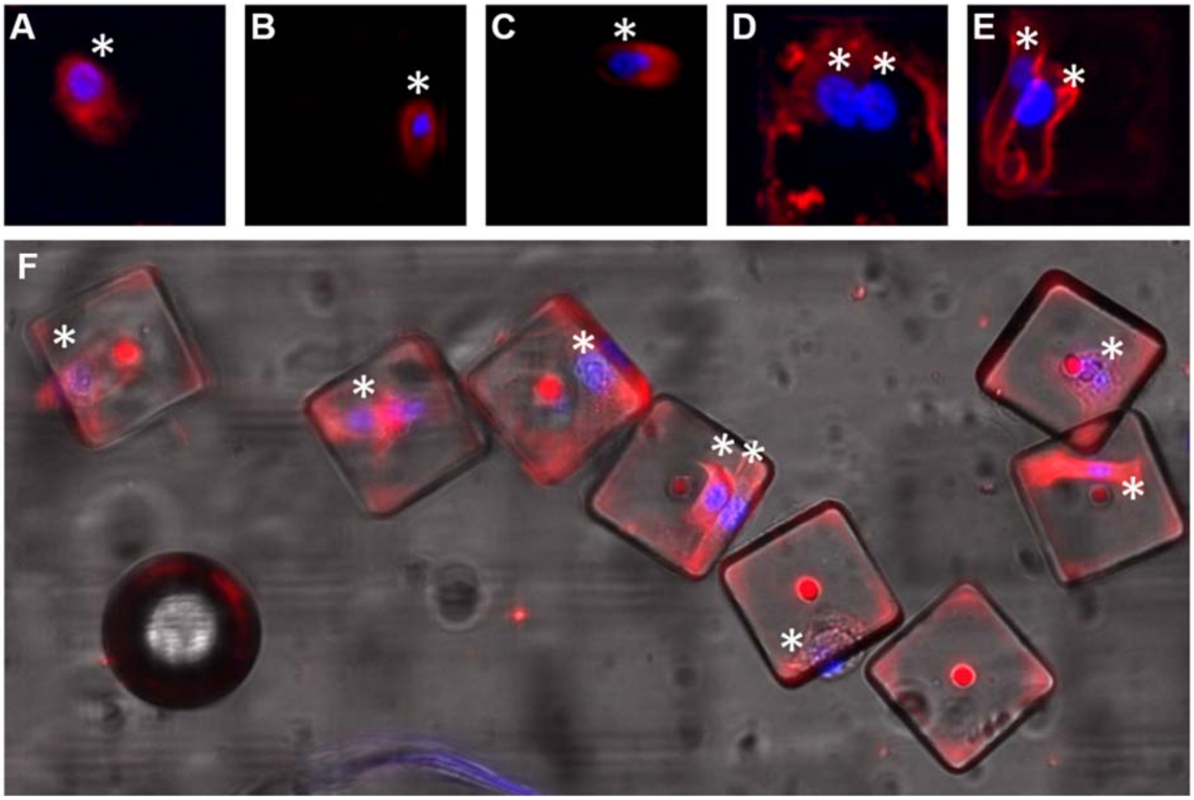

Figure 3.4. PDX cells sorted using micropallets (A-C) Example images of individual EpCAM+ cells successfully identified on micropallets prior to release. (D-E) Example images of micropallets with EpCAM+ cells but greater with than one nuclei which were not successfully declumped by the CellProfiler pipeline. (F) Released micropallets successfully collected from the PDAC sample. Asterisks mark identified cell nuclei, showing 1 micropallet with two nuclei and 1 micropallet without a nuclei. The visible red spot at the center of each pallet is the laser impact site which strongly scatters light.

## 3.6 References

1. Yu, M., Bardia, A., Wittner, B. S., Stott, S. L., Smas, M. E., Ting, D. T., Isakoff, S. J., Ciciliano, J. C., Wells, M. N., Shah, A. M., Concannon, K. F., Donaldson, M. C., Sequist, L. V, Brachtel, E., Sgroi, D., Baselga, J., Ramaswamy, S., Toner, M., Haber, D. A. & Maheswaran, S. Circulating breast tumor cells exhibit dynamic changes in epithelial and mesenchymal composition. *Science* **339,** 580–4 (2013).

2. Navin, N., Kendall, J., Troge, J., Andrews, P., Rodgers, L., McIndoo, J., Cook, K., Stepansky, A., Levy, D., Esposito, D., Muthuswamy, L., Krasnitz, A., McCombie, W. R., Hicks, J. & Wigler, M. Tumour evolution inferred by single-cell sequencing. *Nature* **472,** 90–4 (2011).

3. Wheeler, A. R., Throndset, W. R., Whelan, R. J., Leach, A. M., Zare, R. N., Liao, Y. H., Farrell, K., Manger, I. D. & Daridon, A. Microfluidic Device for Single-Cell Analysis. *Anal. Chem.* **75,** 3581–3586 (2003).

4. Gore, A., Li, Z., Fung, H.-L., Young, J. E., Agarwal, S., Antosiewicz-Bourget, J., Canto, I., Giorgetti, A., Israel, M. A., Kiskinis, E., Lee, J.-H., Loh, Y.-H., Manos, P. D., Montserrat, N., Panopoulos, A. D., Ruiz, S., Wilbert, M. L., Yu, J., Kirkness, E. F., Izpisua Belmonte, J. C., Rossi, D. J., Thomson, J. A., Eggan, K., Daley, G. Q., Goldstein, L. S. B. & Zhang, K. Somatic coding mutations in human induced pluripotent stem cells. *Nature* **471,** 63–7 (2011).

5. Berger, C., Harzer, H., Burkard, T. R., Steinmann, J., van der Horst, S., Laurenson, A.-S., Novatchkova, M., Reichert, H. & Knoblich, J. A. FACS purification and transcriptome analysis of drosophila neural stem cells reveals a role for Klumpfuss in self-renewal. *Cell Rep.* **2,** 407–18 (2012).

6. Siolas, D. & Hannon, G. J. Patient-derived tumor xenografts: transforming clinical samples into mouse models. *Cancer Res.* **73,** 5315–9 (2013).

7. Marangoni, E., Vincent-Salomon, A., Auger, N., Degeorges, A., Assayag, F., de Cremoux, P., de Plater, L., Guyader, C., De Pinieux, G., Judde, J.-G., Rebucci, M., Tran-Perennou, C., Sastre-Garau, X., Sigal-Zafrani, B., Delattre, O., Diéras, V. & Poupon, M.-F. A new model of patient tumor-derived breast cancer xenografts for preclinical assays. *Clin. Cancer Res.* **13,** 3989–98 (2007).

8. Fichtner, I., Rolff, J., Soong, R., Hoffmann, J., Hammer, S., Sommer, A., Becker, M. & Merk, J. Establishment of patient-derived non-small cell lung cancer xenografts as models for the identification of predictive biomarkers. *Clin. Cancer Res.* **14,** 6456–68 (2008).

9. Dong, X., Guan, J., English, J. C., Flint, J., Yee, J., Evans, K., Murray, N., Macaulay, C., Ng, R. T., Gout, P. W., Lam, W. L., Laskin, J., Ling, V., Lam, S. & Wang, Y. Patient-derived first generation xenografts of non-small cell lung cancers: promising tools for predicting drug responses for personalized chemotherapy. *Clin. Cancer Res.* **16,** 1442–51 (2010).

10. Chattopadhyay, P. K., Hogerkorp, C.-M. & Roederer, M. A chromatic explosion: the development and future of multiparameter flow cytometry. *Immunology* **125,** 441–449 (2008).

11. Iglesias-Ussel, M., Marchionni, L. & Romerio, F. Isolation of microarray-quality RNA from primary human cells after intracellular immunostaining and fluorescence-activated cell sorting. *J. Immunol. Methods* **391,** 22–30 (2013).

12. Yang, G., Rich, J. R., Gilbert, M., Wakarchuk, W. W., Feng, Y. & Withers, S. G. Fluorescence activated cell sorting as a general ultra-high-throughput screening method for directed evolution of glycosyltransferases. *J. Am. Chem. Soc.* **132,** 10570–7 (2010).

13. Cheng, Q., Ruebling-Jass, K., Zhang, J., Chen, Q. & Croker, K. M. Use FACS sorting in metabolic engineering of Escherichia coli for increased peptide production. *Methods Mol. Biol.* **834,** 177–96 (2012).

14. Fujio, Y. Akt Mediates Cytoprotection of Endothelial Cells by Vascular Endothelial Growth Factor in an Anchorage-dependent Manner. *J. Biol. Chem.* **274,** 16349–16354 (1999).

15. Howe, A. K., Aplin, A. E. & Juliano, R. . Anchorage-dependent ERK signaling – mechanisms and consequences. *Curr. Opin. Genet. Dev.* **12,** 30–35 (2002).

16. Chen, Q. Cell Anchorage Permits Efficient Signal Transduction Between Ras and Its Downstream Kinases. *J. Biol. Chem.* **272,** 8849–8852 (1997).

17. Xu, W., Sims, C. E. & Allbritton, N. L. Microcup arrays for the efficient isolation and cloning of cells. *Anal. Chem.* **82,** 3161–7 (2010).

18. Niyaz, Y., Stich, M., Sägmüller, B., Burgemeister, R., Friedemann, G., Sauer, U., Gangnus, R. & Schütze, K. Noncontact laser microdissection and pressure catapulting: sample preparation for genomic, transcriptomic, and proteomic analysis. *Methods Mol. Med.* **114,** 1–24 (2005).

19. Gjerdrum, L. M., Lielpetere, I., Rasmussen, L. M., Bendix, K. & Hamilton-Dutoit, S. Laser-Assisted Microdissection of Membrane-Mounted Paraffin Sections for Polymerase Chain Reaction Analysis. *J. Mol. Diagnostics* **3,** 105–110 (2001).

20. Wang, Y., Young, G., Aoto, P. C., Pai, J.-H., Bachman, M., Li, G. P., Sims, C. E. & Allbritton, N. L. Broadening cell selection criteria with micropallet arrays of adherent cells. *Cytometry. A* **71,** 866–74 (2007).

21. Salazar, G. T., Wang, Y., Young, G., Bachman, M., Sims, C. E., Li, G. P. & Allbritton, N. L. Micropallet arrays for the separation of single, adherent cells. *Anal. Chem.* **79,** 682–7 (2007).

22. Gach, P. C., Attayek, P. J., Herrera, G., Yeh, J. J. & Allbritton, N. L. Isolation and in vitro culture of rare cancer stem cells from patient-derived xenografts of pancreatic ductal adenocarcinoma. *Anal. Chem.* **85,** 7271–8 (2013).

23. Quinto-Su, P. A., To'a Salazar, G., Sims, C. E., Allbritton, N. L. & Venugopalan, V. Mechanisms of pulsed laser microbeam release of SU-8 polymer "micropallets" for the collection and separation of adherent cells. *Anal. Chem.* **80,** 4675–9 (2008).

24. Wang, Y., Bachman, M., Sims, C. E., Li, G. P. & Allbritton, N. L. Stability of virtual air walls on micropallet arrays. *Anal. Chem.* **79,** 7104–9 (2007).

25. Shah, P. K., Hughes, M. R., Wang, Y., Sims, C. E. & Allbritton, N. L. Scalable synthesis of a biocompatible, transparent and superparamagnetic photoresist for microdevice fabrication. *J. Micromechanics Microengineering* **23,** 107002 (2013).

26. Dobes, N. C., Dhopeshwarkar, R., Henley, W. H., Ramsey, J. M., Sims, C. E. & Allbritton, N. L. Laser-based directed release of array elements for efficient collection into targeted microwells. *Analyst* **138,** 831–8 (2013).

27. Wang, Y., Young, G., Bachman, M., Sims, C. E., Li, G. P. & Allbritton, N. L. Collection and expansion of single cells and colonies released from a micropallet array. *Anal. Chem.* **79,** 2359–66 (2007).

28. Dalerba, P., Dylla, S. J., Park, I.-K., Liu, R., Wang, X., Cho, R. W., Hoey, T., Gurney, A., Huang, E. H., Simeone, D. M., Shelton, A. A., Parmiani, G., Castelli, C. & Clarke, M. F. Phenotypic characterization of human colorectal cancer stem cells. *Proc. Natl. Acad. Sci. U. S. A.* **104,** 10158–63 (2007).

29. Went, P. T. ., Lugli, A., Meier, S., Bundi, M., Mirlacher, M., Sauter, G. & Dirnhofer, S. Frequent EpCam protein expression in human carcinomas. *Hum. Pathol.* **35,** 122–128 (2004).

30. Edelstein, A., Amodaj, N., Hoover, K., Vale, R. & Stuurman, N. Computer control of microscopes using µManager. *Curr. Protoc. Mol. Biol.* **Chapter 14,** Unit14.20 (2010).

31. Carpenter, A. E., Jones, T. R., Lamprecht, M. R., Clarke, C., Kang, I. H., Friman, O., Guertin, D. A., Chang, J. H., Lindquist, R. A., Moffat, J., Golland, P. & Sabatini, D. M. CellProfiler: image analysis software for identifying and quantifying cell phenotypes. *Genome Biol.* **7,** R100 (2006).

32. Abramoff, M. D., Magalhães, P. J. & Ram, S. J. Image processing with ImageJ. *Biophotonics Int.* **11,** 36–42 (2004).

33. Gunawan, B., Huber, W., Holtrup, M., von Heydebreck, A., Efferth, T., Poustka, A., Ringert, R. H., Jakse, G. & Füzesi, L. Prognostic impacts of cytogenetic findings in clear cell renal cell carcinoma: gain of 5q31-qter predicts a distinct clinical phenotype with favorable prognosis. *Cancer Res.* **61,** 7731–8 (2001).

34. Jones, C., Ford, E., Gillett, C., Ryder, K., Merrett, S., Reis-Filho, J. S., Fulford, L. G., Hanby, A. & Lakhani, S. R. Molecular cytogenetic identification of subgroups of grade III invasive ductal breast carcinomas with different clinical outcomes. *Clin. Cancer Res.* **10,** 5988–97 (2004).

35. Grimwade, D., Walker, H., Oliver, F., Wheatley, K., Harrison, C., Harrison, G., Rees, J., Hann, I., Stevens, R., Burnett, A. & Goldstone, A. The Importance of Diagnostic Cytogenetics on Outcome in AML: Analysis of 1,612 Patients Entered Into the MRC AML 10 Trial. *Blood* **92,** 2322–2333 (1998).

36. Shadpour, H., Sims, C. E., Thresher, R. J. & Allbritton, N. L. Sorting and expansion of murine embryonic stem cell colonies using micropallet arrays. *Cytometry. A* **75,** 121–9 (2009).

37. Ma, H., Mismar, W., Wang, Y., Small, D. W., Ras, M., Allbritton, N. L., Sims, C. E. & Venugopalan, V. Impact of release dynamics of laser-irradiated polymer micropallets on the viability of selected adherent cells. *J. R. Soc. Interface* **9,** 1156–67 (2012).

# Chapter 4 Dynamics and evolution of b-catenin-dependent Wnt signaling revealed through massively parallel clonogenic screening

## 4.1 Introduction

Wnt/β-catenin signaling is an evolutionarily conserved signaling pathway that is involved in development, adult tissue homeostasis, tissue regeneration, and disease. In the absence of Wnt ligand signaling, β-catenin levels are kept low through ubiquitination and proteosome-dependent degradation. Specifically, cytosolic β-catenin is captured by a complex of proteins comprising GSK3β, CK1a, APC and AXIN, which promote its phosphorylation and subsequent ubiquitination by the β-TrCP ubiquitin ligase. Binding of the Wnt ligand to the frizzled receptor inhibits GSK3b-dependent phosphorylation of b-catenin, leading to increased b-catenin levels and stability. β-catenin is then translocated to the nucleus and acts as a co-activator for TCF/LEF family transcription factors. Wnt signaling interacts with a large number of signaling pathways in normal and pathological contexts and large-scale screening efforts continue to identify many novel regulators and potential therapeutic targets.[1–4] The importance of single-cell measurements in the study of tumor systems and signaling pathways has been highlighted by the observation of significant heterogeneity in Wnt signaling at the single-cell level in primary tumor-derived spheroid cultures[5] as well as by mounting evidence for the role of genomic and phenotypic heterogeneity in the evolution and adaptation of tumors.[6–9]

Transcriptional reporters based on the production of chemiluminescence and fluorescence signals have been used successfully in the study of a wide variety of signaling pathways.[10–13] Transcriptional reporters of Wnt/β-catenin signaling have been employed with great success leading to the discovery of several novel regulators of Wnt signaling.[1–3,11] Since Wnt/β-catenin signaling culminates in the co-activation of TCF/LEF family members, transcriptional reporters of Wnt/β-catenin signaling typically contain multiple TCF/LEF binding sites upstream of a reporter gene. While transcriptional reporters measure Wnt pathway activation by virtue of the induced activity of downstream transcription factors, direct measurements of signaling activation are also possible by tracking the localization of β-catenin. Immunohistochemical methods permit observation of nuclear accumulation of β-catenin as a readout for Wnt pathway activation[14], however the dynamic range and the strength of the signal can vary widely as Wnt signaling is highly sensitive to changes in nuclear β-catenin levels rather than the absolute amount present.[15] Additionally, staining can only be performed in fixed cells and significant amounts of β-catenin will be present in adherens junctions at the cell membrane making measurement of nuclear concentrations challenging. Fusions of β-catenin and fluorescent proteins enable high-contrast, real-time tracking of signaling in live cells[16]; however, this strategy suffers from many of the same disadvantages of immunohistochemistry with respect to dynamic range and signal strength. In addition, there remains the risk that the fusion protein significantly alters the function and dynamics of protein degradation and translocation due to potential steric hindrance from the addition of the bulky fluorescent protein component. For these reasons, transcriptional reporters of Wnt/β-catenin signaling remains the most widely used method to measure pathway activation in living cells.

Modern techniques for the study of intracellular signaling depend on the availability of robust and rapid measures of intracellular signaling activity. The quantitative biomolecular and biophysical characterization of intracellular signaling is highly dependent on the dynamic range and intensity of the reporter signal. While luminescent reporters (through the use of firefly luciferase as the reporter gene[17]) remain the most sensitive readout for reporter activation, fluorescent protein-based reporters permit measurement of reporter activation in single, live cells.[18] In an attempt to reduce cell-to-cell variability to permit more sensitive measurements pooled over multiple cells, monoclonal cell lines are often employed for fluorescent reporters.[19–23] Noise from polyclonal variability can also be reduced by averaging measurements over a larger number of cells but this leads to increased reagent consumption, reduced throughput and limited dynamic range. These dynamics and variability of fluorescent transcriptional reporters for β-catenin have not been well characterized in the literature, particularly in the context of the evolution of reporter performance in monoclonal cell lines.

This study presents a detailed characterization of a β-catenin activated reporter driving expression of a nuclear localization signal tagged red fluorescent protein (BAR-mCherry) in A375, a cell line derived from human melanoma[24] that does not exhibit abnormal nuclear accumulation of β-catenin.[25] The dynamics of BAR-mCherry activation and relaxation were measured in 6 monoclonal cell lines expanded from single isolated A375-BAR-mCherry cells. A parallel clonogenic assay was implemented using microfabricated cell arrays to characterize the emergence of heterogeneous reporter activation over time-scales significantly shorter than that required to expand single cells into monoclonal cell lines. A detailed study of the dynamics of transcriptional reporter activation in monoclonal populations would be of significant value in the design and optimization of assays utilizing similar reporter systems. Additionally, parallel clonogenic screening of reporter cell line colonies may shed light on the mechanisms by which reporter cell lines evolve and enable the generation of more stable and uniform reporter libraries.

## 4.2 Materials and Methods

### 4.2.1 Plasmids, Cell Culture and Transfection

A375 human melanoma cells were sourced from the American Type Culture Collection (ATCC). pSL9-BAR-NLS-mCherry was made by mutating pSL9-BAR-Luciferase using site directed mutagenesis to allow for subcloning of NLS-mCherry. The NLS-mCherry construct was a gift of Jon Lane. A375 cells were infected with pSL9-BAR-NLS-mCherry as described previously and will be referred to as A375-BAR-mCherry for brevity.[13] Cells were cultured in Dulbecco's Modified Eagle Medium (DMEM, Life Technologies, Carlsbad, CA) with 10% fetal bovine serum (FBS, Thermo Scientific, Waltham, MA), 500 ng / mL gentamicin sulfate and 250 ng / mL amphotericin B (Life Technologies, Carlsbad, CA).

### 4.2.2 Microraft Array Fabrication

The 6 monoclonal A375-BAR-mCherry cells were isolated using a microraft array platform. Microraft arrays were fabricated as previously described.1 Briefly; microraft master molds were prepared by single layer photolithography using 1002F photoresist and a chrome mask with a pattern of 110×110 200 µm square apertures with a 30 µm gap.2 After fabrication of the master, the microraft array substrate was prepared by casting polydimethylsiloxane (PDMS; Sylgard 184, Dow Corning Corp., Midland MI) onto the mold and curing at 95 ºC for 1 hour. The PDMS well array was then demolded from the master and filled by overlaying a solution of 30% polystyrene in γ-butyrolactone with 3% iron oxide nanoparticles by weight and applying vacuum. The filled microwell array was then lowered into a bath of excess magnetic polystyrene solution and slowly withdrawn at a rate of 25 mm/h to achieve discontinuous dewetting. The dip-coated microwell array was then baked overnight at 95 ºC to remove solvent from the polystyrene and harden the microrafts. The fabricated microraft arrays were mounted to cassettes, oxidized in an air plasma (Harrick Plasma, Ithaca, NY) for 5 min and sterilized with 75% ethanol and air-dried immediately prior to use.

### 4.2.3 Micropallet Array Fabrication

Micropallet arrays were utilized for the parallel clonogenic screening due to the ability of stable virtual air walls to prevent migration of the cell type employed for extended periods of culture. Micropallet arrays were fabricated as previously described using a composite photoresist of poly(methyl methacrylate-co-methacrylic acid) and 1002F termed PMMA/1002F.3,4 Briefly, a 35 µm thick layer of photoresist was generated on glass slides by spin coating in two steps: 500 rpm for 10 s followed by 2500 rpm for 30 s. The film was then dried by soft baking at 95 ºC for 1 h. The film was then exposed using a 360 nm long-pass filter for 3 exposures lasting 1 min each with a 1 min gap between each exposure to prevent excessive heating of the photoresist. After exposure the film was cross-linked by baking at 95 ºC for 10 min and developed in 2-methoxypropylacetate for 4 min. After developing the micropallet arrays were oxidized in an air plasma for 5 min prior to silanization. To establish stable virtual air walls, 100 µL of (Heptadecafluoro-1,1,2,2-tetrahydrodecyl)trichlorosilane (Gelest Inc, Morrisville PA) was added to a dish adjacent to micropallet arrays placed in a dry-seal vacuum dessicator (Wheaton, Millville NJ) and a vacuum was applied using an oil-free pump for 2 min. The dessicator was then sealed and incubated for 16 h. After 16 h, vacuum was again applied for 30 minutes to remove excess silane and the treated micropallet arrays were removed. The micropallet arrays were then immediately mounted into cassettes and sterilized with 75% ethanol prior to use.

### 4.2.4 Conditioned Media and Reagents

Control and Wnt-3a transfected L-cells were obtained from the ATCC and conditioned media was prepared according to ATCC protocol. Murine recombinant Wnt-3a was purchased from Sigma-Aldrich and reconstituted at 1 mg/mL in deionized (DI) water with 0.1% bovine serum albumin and stored in aliquots at -80 °C. Aliquots were thawed and diluted further with phosphate buffered saline (PBS; 137 mM NaCl, 10 mM $Na_2HPO_4$, 27 mM KCl, 1.75 mM $KH_2PO_4$, pH 7.4) and used immediately. The GSK3β inhibitor CT 99021 (CHIR 99021, Axon Medicinal Chemistry, Vienna, VA) was stored as a 10 mM solution in DMSO at -20 °C.

### 4.2.5 Cell Cloning Using Arrays of Releasable Microstructures

Single A375-NLS-mCherry cells were isolated and expanded using arrays of releasable microstructures as a cloning platform.[26] The arrays were sterilized by rinsing with 70% ethanol and air-drying prior to use. A suspension of 4,000 A375-NLS-mCherry cells was seeded into two arrays and incubated for 16 h to allow the cells to adhere. After 16 h the media was exchanged and replaced with 1:1 Wnt-3a conditioned media and fresh DMEM and incubated for 36 h. After 36 h the arrays were stained with 500 ng/mL Hoechst 33342 in PBS for 15 min which was then replaced with fresh DMEM. The array was moved to an inverted microscope (TE-2000-U, Nikon Instruments Inc. Melville, NY) mounted with a custom fabricated collar to hold a 150 μm diameter needle (Roboz Surgical Instrument Co. Gaithersburg, MD) above the 4× objective. Array elements containing a single cell (as identified by the presence of a single fluorescent nucleus in the Hoechst channel) that exhibited strong reporter activation (nuclear localization of mCherry fluorescence) were dislodged from the array as described previously.[26] The released, magnetic microstructures were collected individually with a permanent magnet and transferred to separate wells in a 96-well plate, each containing 100 µL of expansion media (50% A375 conditioned media, 25% fresh DMEM and 25% FBS). A375 conditioned media was prepared by sterile filtering 20 mL of DMEM which had been overlaid on a T75 flask seeded with A375 cells at 50% confluence and aspirated after incubation for 48 h. Media was exchanged every 72 h until expanding colonies greater than 1 mm in diameter were observed. The colonies were then released with 0.15% trypsin and transferred to a 6-well plate for further expansion in standard DMEM. After 3 weeks of total expansion, cells were present at sufficient density to passage and aliquots were cryopreserved in FBS with 10% DMSO. A total of 6 monoclonal cell lines were generated and maintained for characterization. Fresh aliquots of monoclonal cells were used for at least 1 passage after thawing and within 3 passages after thawing.

### 4.2.6 Single Cell Tracking and Reporter Dynamics Measurement

All 6 monoclonal A375-BAR-mCherry cell lines were screened on 3 cell culture substrates: tissue culture treated polystyrene (TC), fibronectin (Fbn) and gelatin (Gel). To prepare the fibronectin-coated surface, wells of a tissue culture treated 96-well plate were incubated at 25 °C in 50 µL of 20 µg/mL of human plasma fibronectin (EMD Millipore, Billerica, MA) for 1 h then rinsed 3× with PBS before use. Gelatin coated wells were prepared by incubating at 25 °C in 0.1% gelatin in water (EMD Millipore) for 1 h, then rinsed 3× with PBS before use. 1000 cells from each monoclonal line were seeded into two wells each with identical surface treatments containing 100 µL of DMEM and incubated for 16 h to allow the cells to adhere and stabilize. The media was aspirated and replaced with 50 µL of DMEM with 1 µg/mL of recombinant Wnt-3a and 250 ng/mL of Hoechst 33342 and incubated at 37 °C for 2 h. In control wells, media was replaced with DMEM containing 250 ng/mL of Hoechst 33342 and a volume of 0.1% BSA in water identical to the volume added in media containing Wnt-3a. After 2 h the media was aspirated, the wells rinsed gently 3× with warm PBS (37 °C) and replaced with 100 µL of fresh DMEM and 250 ng/mL of Hoechst 33342. The 96-well array was then transferred to an inverted microscope (IX-81, Olympus America, Center Valley, PA) enclosed in a custom fabricated black Delrin housing with temperature, humidity (AirTherm ATX-H, World Precision Instruments, Sarasota, FL) and $CO_2$ (Pro$CO_2$, BioSpherix, Lacona, NY) regulation maintained at 37 °C, 60% relative humidity and a 5% $CO_2$ atmosphere. The inverted microscope was outfitted with a motorized XY stage (MS-2000, Applied Scientific Instrumentation, Eugene, OR), a metal arc lamp excitation source (Lumen 200, Prior Scientific, Rockland, MA), high speed shutter (Lambda 10-2, Sutter Instrument Company, Novato, CA) and cooled interline CCD camera (CoolSnap HQ2, Photometrics, Tucson, AZ). Multiple positions within each well were imaged at 10× magnification in the Hoechst and mCherry channels every 10 min for 62 h using the multidimensional acquisition tool in the open source microscope control software, Micro-Mananger.[27] A reference well was seeded with beads containing a fluorescent standard (MultiSpeck, Life Technologies) and was also imaged every 10 min in both channels.

The Hoechst channel image at each position and time-point was segmented using a custom pipeline implemented in CellProfiler[28]. Briefly, background fluorescence in the image was estimated by grayscale morphological opening and subtracted from the original image. The image was then smoothed with a 6 pixel median filter to reduce over segmentation of nuclei. The smoothed image was then converted to a black and white image with a threshold determined by the two-class implementation of Otsu's method[29] and segmented nuclei were declumped using a watershed method based on the shape of the detected nuclei. The segmented images were then exported with each object labeled by a 16-bit integer number for tracking. A custom tracking script was implemented in MATLAB (The Mathworks Inc. Natick, MA) using the overlap method. Briefly, the intersection of every time-adjacent pair of images was calculated and nuclei in each image were assigned a shared label with the segmented nuclei from the previous time-point with which it shared the largest overlap. A second search was implemented to identify nuclei which shared no overlap with a nucleus in a previous time-point by searching for unmatched nuclei within a 20 µm neighborhood from the detected nucleus' position. In cases where no match was found by overlap or distance (for example when a cell migrated from outside of the field of view), a new label was generated and used to track that object in subsequent frames although measurements were only made for cells that could be tracked uninterrupted over all time-points. The labeled images of cell nuclei were then dilated by 5 pixels and used to integrate fluorescence in the mCherry channel for each corresponding nucleus at each time-point. Images of the reference well containing fluorescence standard beads were segmented in both channels using an empirical threshold and the mean fluorescence density (object intensity / object area in pixels) of the beads in each channel were measured at each time-point to control for variations in arc lamp intensity.

### 4.2.7 Array Scan Automation

Microfabricated arrays were scanned using an automated software utility that provided a customized interface to the µManager microscope control libraries. Array scanning required four steps: user input of the array geometry (number of rows and columns, array element dimensions), user-assisted localization of 2 opposing or 3 adjacent array corners, user-assisted focus at 4 or more positions in the array to calculate the plane of best fit and the sequential imaging of each field of view within the array. Images from each field of view were segmented based on the position of each microstructure which was calculated by interpolating from the user-identified corner positions and images of each individual microstructure were saved separately for image analysis.

### 4.2.8 Clonogenic Screening

Microfabricated cell arrays (110×110 array, rows × columns, 200×200×35 μm elements, length × width × height) were fabricated and prepared as previously described (detailed methods provided in supplement).[30,31] For clonogenic screening, the arrays were mounted in custom cassettes fabricated by 3D printing polylactic acid with a convention fusion deposition modeling printer (BFB-3000, Bits from Bytes Ltd, now 3D Systems Inc. Rock Hill, SC) by gluing with a small amount of PDMS. The mounted arrays were sterilized by rinsing with 75% ethanol in water and air-dried prior to coating with fibronectin. The fibronectin coating was prepared by incubating the arrays in 20 μg/mL fibronectin in PBS for 2 h at 25 °C. The arrays were then rinsed 3× with PBS and immediately seeded with cells.

A total of 3,000 cells from the polyclonal A375-BAR-mCherry line were seeded onto each of 4 arrays and incubated for 16 h. After 16 h, the media was exchanged and the cells were incubated in 500 ng/mL of Hoechst 33342 in DMEM for 15 min at 37 °C and rinsed 3× with PBS. Two arrays were overlaid with DMEM containing 1 μg/mL of recombinant Wnt-3a and 2 arrays were overlaid with DMEM containing 5 μM CT 99021. The arrays were immediately scanned at 4× magnification to measure Hoechst and basal mCherry fluorescence. After scanning, the arrays were incubated for 36 h at 37 °C, rinsed 3× with PBS and incubated in DMEM containing 500 ng/mL of Hoechst 33342 in DMEM for 15 min at 37 °C. The arrays were again rinsed 3× with PBS and immediately scanned. After an additional 36 h, the arrays were re-stained with Hoechst 33342, rinsed and the media was replaced prior to scanning. The media was exchanged 48 h later but the arrays were not scanned. A total of 5 d after the previous scan and after single cells on the array had expanded into colonal colonies, the media was exchanged, the arrays stained with Hoechst 33342, and overlaid with solutions of recombinant Wnt-3a and CT 99021 as described above and the arrays were again scanned. After 36 h, the arrays were rinsed, stained and overlaid with DMEM prior to the final scan. Images from scanned arrays were segmented using the CellProfiler pipeline described above with parameters empirically adjusted to account for the higher background fluorescence from the photoresist substrate and lower magnification of the images. The integrated mCherry fluorescence was processed in terms of fluorescence density (RFU / pixel) using MATLAB since the mean fluorescence density of a colony will not be affected by under or over-segmentation errors caused by densely clustered cell nuclei. The purity of monoclonal colonies was assessed by manually inspecting the images of 25 microstructures on each array which had at least 2 adjacent microstructures with no cells at the first time-point of the experiment.

## 4.3 Results and Discussion

### 4.3.1 Description of BAR-mCherry Reporter

Monoclonal cell lines are widely utilized in quantitative biomolecular and biophysical assays in an attempt to reduce biological variability as a source of noise.[19–23] The generation of monoclonal cell lines requires the expansion of single cells over tens of generations to provide a sufficiently large number of cells to process using conventional tissue culture techniques. The evolution of monoclonal cell lines over these timescales has not been well characterized. To characterize a reporter system in monoclonal cell lines, A375 cells were infected with a β-catenin activated reporter (BAR) driving expression of a nuclear localization signal-tagged mCherry red fluorescent protein (NLS-mCherry). The BAR-mCherry reporter utilizes 12× TCF/LEF binding sites upstream of an NLS-tagged mCherry construct to function as a readout for Wnt/β-catenin signaling (Figure 4.1A). In A375-BAR-mCherry cells, NLS-mCherry is not produced at levels detecTable 4.by fluorescence microscopy (Figure 4.1B) until treatment with Wnt3A ligand (Figure 4.1C). The nuclear localization signal leads to accumulation of mCherry in the nucleus, simplifying automated image analysis as only segmentation of the nucleus is required to quantify mCherry fluorescence.

### 4.3.2 Variability in Wnt Signaling Reporter Activity

Six monoclonal cell lines were generated from a polyclonal population of A375 cells transfected with BAR-mCherry for the characterization of reporter dynamics. These clones were expanded over multiple generations (3 weeks, >25 generations) on a conventional polystyrene surface to populations large enough to be passaged and manipulated conventionally and the dynamics of reporter activation were measured at the single cell level within each clone. Cells were tracked for 62 h with or without a brief treatment of recombinant Wnt-3a (1 µg/mL, 2 h). The production of mCherry over time was measured from a total of 1,895 treated cells (Figure 4.7) and 781 untreated cells (Figure 4.8) cultured on polystyrene by fluorescence microscopy and single-cell tracking.

Significant variability was observed in both the kinetics (Figure 4.2A) and magnitude (Figure 4.2B) of Wnt reporter activation between A375-BAR-mCherry clones, however the magnitude of activation (12 pair-wise differences, $p < 0.01$, p-values listed in Table 4.1) was seen to vary more between clones than the kinetics of activation (6 pair-wise differences, $p < 0.01$, p-values listed in Table 4.2). Clone 2 was observed to be the most unique of all 6, showing significant differences in the median magnitude of activation and the time to reach peak activation relative to all other clones tested. Clones 1, 3, 5 and 6 exhibited pairwise differences in their median peak magnitude of activation between all but one other clone with similarities observed between clones 1 and 3 and clones 5 and 6. The kinetics of activation varied minimally in clones 2 through 6, with the only additional pair-wise difference existing between clones 2 and 4. The signal relaxation kinetics of single A375-BAR-mCherry cells, while highly varied ($\mu = 6.5$ h, $\sigma = 5.6$ h), did not exhibit many differences between clones (Figure 4.2C). Only 2 statistically significant pair-wise differences were observed in the median time for signal to relax to half peak fluorescence ($p < 0.01$, p-values listed in Table 4.3); between clones 2 and 4 and clones 4 and 6. The activation kinetics, peak activation magnitude and signal relaxation rate of BAR-mCherry are believed to be a function of 3 basic processes: induction of Wnt signaling and activation of the BAR-mCherry reporter, synthesis and nuclear transport of NLS-mCherry and the non-specific proteasomal degradation of NLS-mCherry. In addition to significant intraclonal variability in the magnitude and kinetics of reporter activation and inactivation, the interclonal variability observed (primarily in peak activation magnitude and to a lesser extent in activation kinetics) is suggestive of the presence of fundamental differences in Wnt signaling, transcriptional, translational and degradation phenotypes between individual monoclonal cell lines.

### 4.3.3 Variations in Reporter Dynamics Are Regulated by Independent Processes

Hoechst fluorescence, a measure of DNA concentration, and reporter activation kinetics were not correlated with reporter activation magnitude for any individual clone (Table 4.4) or for the measurements of all clones pooled together (Figure 4.3A, B). The nuclear size and Hoechst fluorescence intensity of cells was observed to vary significantly even within monoclonal populations, indicative of aneuploidy. Wnt signaling is modulated during the cell cycle[32,33], however it is not possible to correlate progression through the cell cycle with DNA concentration measured by Hoechst fluorescence in an aneuploid population. In comparing the mean intensity of nuclear Hoechst fluorescence over the course of the experiment against the peak activation magnitude (Figure 4.3A), no correlation between the two measurements was seen for any of the clones ($r^2 = 0.09$). Thus the amount of DNA present in each cell did not appear to influence the magnitude of reporter activation and the magnitude of reporter activation was independent of DNA content or degree of aneuploidy. The kinetics of activation (as measured by the time require to reach peak fluorescence intensity) were also uncorrelated with the magnitude of activation ($r^2 = 0.15$; Figure 4.3B). While the rate of signal accumulation varied significantly from cell-to-cell, it was not dependent on or influenced by the activation magnitude of the reporter. This suggests that the rate and magnitude of reporter activation were regulated by distinct processes. It is likely that the rate of signal accumulation was a function of the kinetics of NLS-mCherry translation and degradation while the magnitude of reporter activation was a function of the fold-change in the nuclear concentration of β-catenin.[15] The signal relaxation kinetics of all 6 clones varied widely from cell to cell, but was observed to be uncorrelated with either peak activation magnitude (Figure 4.3C, $r^2 = 0.01$) or the time required to reach peak activation (Figure 4.3D, $r^2 = 0.006$). In tumor cells, non-specific proteasomal degradation likely dictates the reporter signal decay rate due to the critical role protein degradation plays in survival.[34–36] In totality, these observations strongly support the interpretation that the kinetics of reporter activation, the magnitude of reporter activation and the kinetics of signal relaxation were independently regulated and highly variable processes in A375-BAR-mCherry. While we could not test for correlations between cell cycle and reporter activation magnitude, Hoechst fluorescence, a measure of DNA concentration was not correlated with reporter activation magnitude.

### 4.3.4 Matrix-dependence of Wnt/β-catenin Reporter Activation

The influence of extracellular matrix (ECM) mediated signaling on the reporter phenotype was also characterized for each clone as a potential indicator of inter-clonal phenotypic variability as integrin signaling is known to promote Wnt activity.[37–40] Differential integrin binding to polystyrene, gelatin and fibronectin surfaces was expected to produce different degrees of reporter modulation in cells treated with Wnt. Three culture substrates were evaluated: tissue-culture polystyrene, human-plasma fibronectin, and gelatin. Cells cultured on each substrate were tracked for 62 h with or without a brief treatment of recombinant Wnt-3a (1 μg/mL, 2 h). The production of mCherry over time was measured from a total of 5,598 treated cells (Figure 4.7) and 2,647 untreated cells (Figure 4.8) by fluorescence microscopy and single-cell tracking. Reporter activation kinetics, peak activation magnitude and signal relaxation kinetics for cells cultured on fibronectin and gelatin were observed to be similarly uncorrelated as compared to cells cultured on polystyrene (Figure 4.S3A-C). Reporter activation magnitude was also similarly uncorrelated with mean Hoechst fluorescence (Figure 4.S3D). This further reinforces our conclusion that these components of overall reporter dynamics are independent of each other as well as of ECM-mediated effects on Wnt signaling in A375-BAR-mCherry.

While significant intraclonal heterogeneity was present in all clones on all cell culture substrates in terms of reporter activation kinetics (Figure 4.4A) and relaxation kinetics (Figure 4.4C), the ECM did not possess a strong impact on these attributes in most clones. In terms of reporter kinetics, activation rates (Figure 4.4A) exhibited a dependence on cell culture substrate in only two clones ($p < 0.01$, p-values listed in Table 4.5), while signal relaxation rates (Figure 4.4C) exhibited no dependence on ECM interactions ($p < 0.01$, p-values listed in Table 4.6). Within clones 3 and 4, a statistically significant difference was observed in the time required to reach peak mCherry fluorescence between cells cultured on fibronectin and cells cultured on gelatin. Within clone 4, a difference was also observed in the time required to reach peak fluorescence between cells cultured on polystyrene and cells cultured on gelatin. The presence of only 3 statistically significant pair-wise differences out of 12 comparisons in the dependence of reporter activation kinetics on ECM interactions demonstrated that that intraclonal variability in reporter activation and signal relaxation kinetics was generally much greater than the variability caused by ECM-dependent interactions.

In contrast to activation and relaxation kinetics, reporter activation magnitude was observed to depend on cell culture substrate (Figure 4.4B) with significant variations in magnitude both within and between clones (12 pair-wise differences out of 18 comparisons, $p < 0.01$, p-values listed in Table 4.7). For clones 1-3, cells cultured on fibronectin reached a significantly higher peak fluorescence intensity ($p < 0.01$, p-values listed in Table 4.8) than on polystyrene or gelatin. Clones 4-6 departed from this trend, again suggesting the presence of distinct signaling phenotypes within the A375-BAR-mCherry population from which the clones were selected.

### 4.3.5 Characterization of Reporter Cell Lines by Clonogenic Screening

The dangers of phenotypic and genetic drift of in-vitro cultured cell lines over time have been widely discussed.[41,42] In light of the time required to expand monoclonal cell lines to sufficient size for manipulation with conventional cell culture techniques, there is some question as to whether the heterogeneity observed in reporter systems for Wnt/β-catenin signaling are inherent to the pathway, artifacts of the reporter, a product of long-term drift or a combination of all three. Regardless of the origins of this diversity, there are significant practical implications for the use of monoclonal cell lines and transcriptional reporters. Studying monoclonal colonies a smaller number of generations removed from the originating mother cell could reduce the impact of long-term phenotypic drift and provide evidence as to the origins of inter- and intra-clonal heterogeneity, but would also reduce the statistical power of measurements made on the smaller number of cells available. Analyzing a large number of monoclonal colonies in parallel would enable statistical comparisons to be made while also increasing the likelihood of capturing a representative sample of the diverse signaling phenotypes which may be present. To characterize the diversity of monoclonal colonies early in their evolution, we screened a large number of A375-BAR-mCherry clones in a massively parallel fashion using microfabcricated cell arrays.[43–45] With these arrays, cells are prevented from migrating between adjacent microstructures by a long-lived intervening air bubble.[31] The maintenance of clonal isolation was assessed by manually examining 25 microstructures and their neighboring unoccupied microstructures on each of 4 arrays (100 microstructures in total) over 8 days. Across all 100 positions examined and over the 8 days, no cells ever appeared on microstructures that were unoccupied on day 1.

The clonogenic screen consisted of 3 steps: an initial activation assay on single A375-BAR-mCherry cells after 16 h of culture on cell arrays, a 5 day expansion period in which the single cells grew into monoclonal colonies and a final activation assay performed on the monoclonal colonies at day 8 of culture (Figure 4.5). The activation assays were performed by addition of Wnt-3a or CT99021 (an inhibitor of GSK3β) to the arrayed cells followed imaging of Hoechst and mCherry fluorescence 36 h later. The 5-day expansion period was selected so that colonies could undergo up to 6 rounds of cell division (A375 doubling time is <20 h[46]). By assaying both single A375-BAR-mCherry cells and their clonal progeny, reporter activation of the clones could be correlated to the activity of the mother cell to track divergence. In addition to imaging the arrays for mCherry expression before and after the initial and final activation assays, a scan was performed 36 h after completion of the first activation assay to track signal relaxation; however, no cells were observed to be detectably more fluorescent than basal levels at this time-point. A total of 1,119 clones were assayed over four arrays. Of these, 684 clones were tracked on two arrays treated with Wnt-3a and 435 clones were tracked on two arrays treated with CT 99021.

### 4.3.6 Evidence of Cell Division-Dependent Wnt Signaling Feedback

On average, daughter cells treated with Wnt-3a (Figure 4.6A) showed 13.9% lower peak fluorescence relative to their corresponding mother cells. Reporter activation magnitude was observed to vary with the number of cell divisions a colony underwent in A375-BAR-mCherry clones treated with Wnt-3a (Figure 4.6A, C). Cells which were viable but remained non-proliferative (corresponding to 0 divisions) exhibited significantly ($p < 0.01$) weaker mCherry fluorescence during the second treatment step relative to the first treatment. Cells that did not divide did not exhibit detectably greater basal levels of activation prior to the second treatment. This observation directly supports previous evidence of the self-inhibition by Wnt/β-catenin pathway activation[47] (Figure 4.1A). Multiple downstream gene targets of β-catenin include Wnt signaling inhibitors such as DKK[48], which causes Frizzled receptor internalization, β-transducin repeat containing protein[49] (β-TrCP), which mediates ubiquitination of phosphorylated β-catenin, and Axin2[50], a key scaffold for the destruction complex.

Cell division or associated signaling processes regulate Wnt self-inhibition. Colonies treated with Wnt-3a that underwent multiple cell divisions (>2) exhibited significantly increased reporter activation levels relative to the overall population (Figure 4.6C; $p < 0.01$). A number of positive feedback loops for Wnt pathway activation have been identified with oncogenic implications.[51–54] These feedback loops regulate Wnt signal transduction at both the receptor and destruction complex level and can lead to increased β-catenin expression levels. The link between positive feedback and cell division is less clear although several of the signaling pathways responsible for positive feedback in Wnt signaling are also tied to proliferative phenotypes including hepatocyte growth factor receptor[51,55] (HGFR), extracellular signal-regulated kinases[52] (ERK), c-Myk[56] and phospholipase D1[54] (PLD1). The observed correlation with cells undergoing multiple divisions (Figure 4.6C) suggests that increased proliferation may be an effect of increased feedback activity from these or other Wnt signaling partners rather than a cause. At least some of the heterogeneity we observed can likely be attributed to epigenetic silencing or activation of reporter integration sites[57], however epigenetic silencing of the reporter should be randomly distributed over a sufficiently large number of sub-clones and should not exhibit a bias that is dependent on the point of pathway activation or cell division.

### 4.3.7 Inhibition of GSK3β Removes Cell Division-Dependence of Reporter Activation

In A375-BAR-mCherry clones treated with CT99021, reporter activation magnitude was seen to decrease by an average of 8.34% relative to the activation magnitude of the mother cells. Reporter activation magnitude did not vary with the number of divisions a colony underwent (Figure 4.6B, D). The lack of a trend in clones treated with CT99021 ($p > 0.01$, Figure 4.6D) agrees with proposed mechanisms of Wnt self-inhibition as this feedback is integrated at or before the level of the destruction complex. Since GSK3β inhibition directly inhibits the function of the destruction complex, desensitization to Wnt by increased expression of DKK, β-TrCP or Axin2 in cells would have no effect on the induction of signaling in cells treated with CT 99021. Positive feedback was also not evident in colonies treated with CT99021 as the distribution of the fold-change in reporter activation magnitude was homogenous with respect to the number of cell divisions each colony underwent (Figure 4.6D). Since the known mechanisms of Wnt sensitization and positive feedback also function at or upstream of the destruction complex, their effects on reporter activation by treatment with CT 99021 would be expected to have been significantly reduced. While increased β-catenin expression levels might still result in positive feedback, recent evidence suggests that Wnt signaling is defined by a fold-change in nuclear β-catenin concentration, not the absolute concentration and the magnitude of reporter activation we observed was likely dominated by the activity of CT 99021.[15]

## 4.4 Conclusions

Our observations present a cautionary tale regarding the reliance on monoclonal cell lines as reporter systems for the study of intracellular signaling. Conventional in-vitro reporter-based assays probe simplified systems in which the dynamics of cellular signaling and interactions are suppressed or reduced through strategies such as the generation of monoclonal cell lines, however this is fraught with risk. We observed the selection of distinct signaling phenotypes in the generation of monoclonal cell lines which may represent (or miss) rare subpopulations in the polyclonal population or which may not exist in-vivo. In the characterization of ECM-dependent modulation of reporter activation, we observed significant differences in the pattern of signal enhancement and inhibition between clones. As extracellular signaling is integrated into Wnt signaling through multiple intermediates[37–40], it is possible that these distinct phenotypes may be defined by differences in expression levels or mutations in intermediate signaling cascades or receptor signaling complexes. This is an alarming observation for signaling investigations which rely on monoclonal cell lines as characterization of individual clones with different signaling phenotypes could lead to seemingly contradictory observations. For example, selection of a single clone could provide evidence that fibronectin-mediated integrin signaling enhances Wnt-induced reporter activation (*eg.* clone 1) or, if a different clone had been selected, the same experiments could suggest the opposite relationship (*eg.* clone 5). The use of single monoclonal cell lines should thus be avoided in the study of signaling pathways as phenotypes and interactions identified may vary significantly between different clones, even those prepared from the same cell line, reducing the generalizability of findings and making their replication challenging. We observed reporter activation levels diverge within 5 generations of the isolation of clonal populations over a 2-log range (0.1-10× the relative signal response of the mother cells). This range matches closely with observations in a different biological and reporter system for β-catenin[5], suggesting that our observations are not unique to A375-BAR-mCherry. Single-cell resolution measurements of polyclonal populations are likely a more robust platform for screening and discovery. Combining single-cell measurements with a platform for performing cell isolations, such as arrays of releasable microstructures, would allow sub-populations exhibiting distinct phenotypes to be separated and further studied. This would enable a more robust and complete characterization of heterogeneous samples without bias towards specific phenotypes which may be present.

Our observations strongly support the existence of both positive and negative feedback in Wnt/β-catenin signal activation, at least in the A375 cell line. The observation of changing signaling phenotypes in cells stimulated with Wnt-3a over different colony sizes suggests a potential role of cell division or a combination of associated molecular signaling events in modulating both the negative and positive self-regulation of Wnt signaling. To perform a clonogenic screen on the scale that was presented here by limiting dilution would require an average of 3,042 wells to be seeded, consuming eight 384-well plates, 245.8 mL of media per exchange and 245.8 μg of Wnt-3a. Cell array technology enables the rapid performance of a massively parallel clonogenic screen with comparatively little reagent consumption; in ideal cases up to a 99.5% reduction in reagent consumption on a per-clone basis relative to well-plate screening (Table 4.9). Additionally, the ability to sort individual selected clones can be utilized in future studies to trace the mechanisms of emergent heterogeneity as well as in the identification of novel regulators of Wnt signaling.

Our observation of multiple clones with diverse signaling phenotypes within a single cell line (Figure 4.2A & B) highlights the risks of artificially reducing diversity within a reference population, particularly for tumor cells which are known to host diverse subpopulations.[6,7] High throughput screens[20,21,58], fundamental investigations of intracellular signaling[59,60] and single-cell measurements[8,19] performed using a small number of clones could be dramatically affected by the unintentional selection of distinct phenotypes and their results may prove difficult to reproduce or contradictory to the investigations of other groups as a consequence, despite their accuracy within their respective reference systems.

## 4.5 Figures

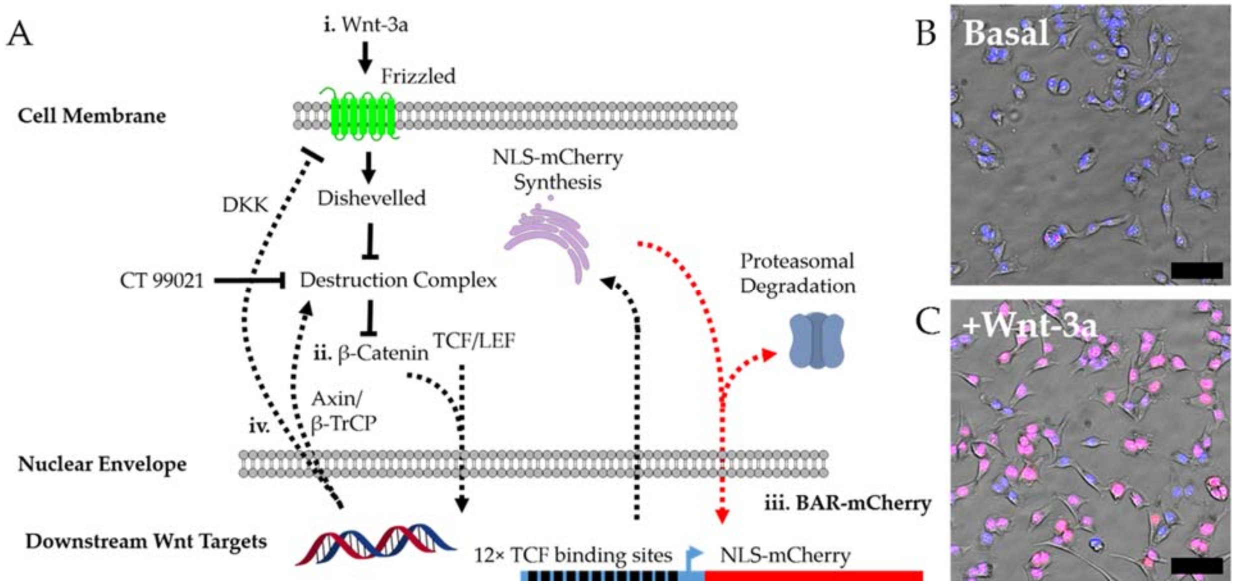

Figure 4.1. Overview of BAR-mCherry reporter. (A) Simplified schematic of BAR-mCherry integration into the canonical Wnt/β-catenin signaling cascade. (i) Wnt-3a binding to Frizzled results in inhibition of the destruction complex. (ii) β-catenin translocated to the nucleus drives gene expression in concert with TCF/LEF transcription factors. (iii) BAR-mCherry is produced from active β-catenin signaling and builds up as long as production exceeds degradation. (iv) Downstream targets of Wnt include several of its own regulators including Axin and β-TrCP which mediate β-catenin degradation and DKK which causes Frizzled receptor internalization. Example images showing A375-BAR-mCherry cells treated with L-cell conditioned media (no Wnt-3a) (B) and Wnt-3a conditioned media (C) for 24 h. Nuclei are counterstained with Hoechst 33342 (blue) to show nuclear localization of NLS-mCherry (red, merge = pink). Scale bar is 100 µm.

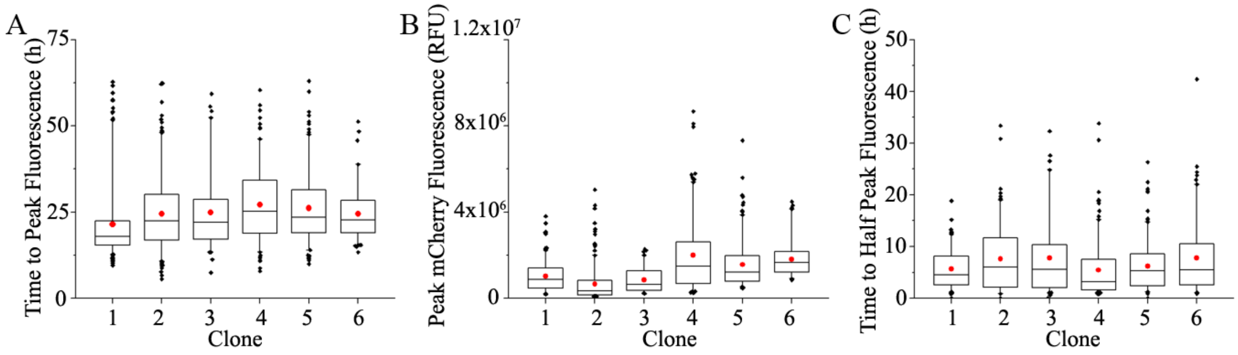

Figure 4.2. Box and whisker plots showing the characterization of A375 clones. (A) Times required to reach peak fluorescence, (B) the peak mCherry fluorescence achieved and (C) the time required for signal to decay to half peak fluorescence for single A375-BAR-mCherry cells cultured on polystyrene. Red circles mark the population mean for each distribution. Outliers shown are observations above the 5th and below the 95th percentile. The boxes mark the 25th, 50th (median) and 75th percentiles within the distribution while the whiskers mark the 5th and 95th percentiles.

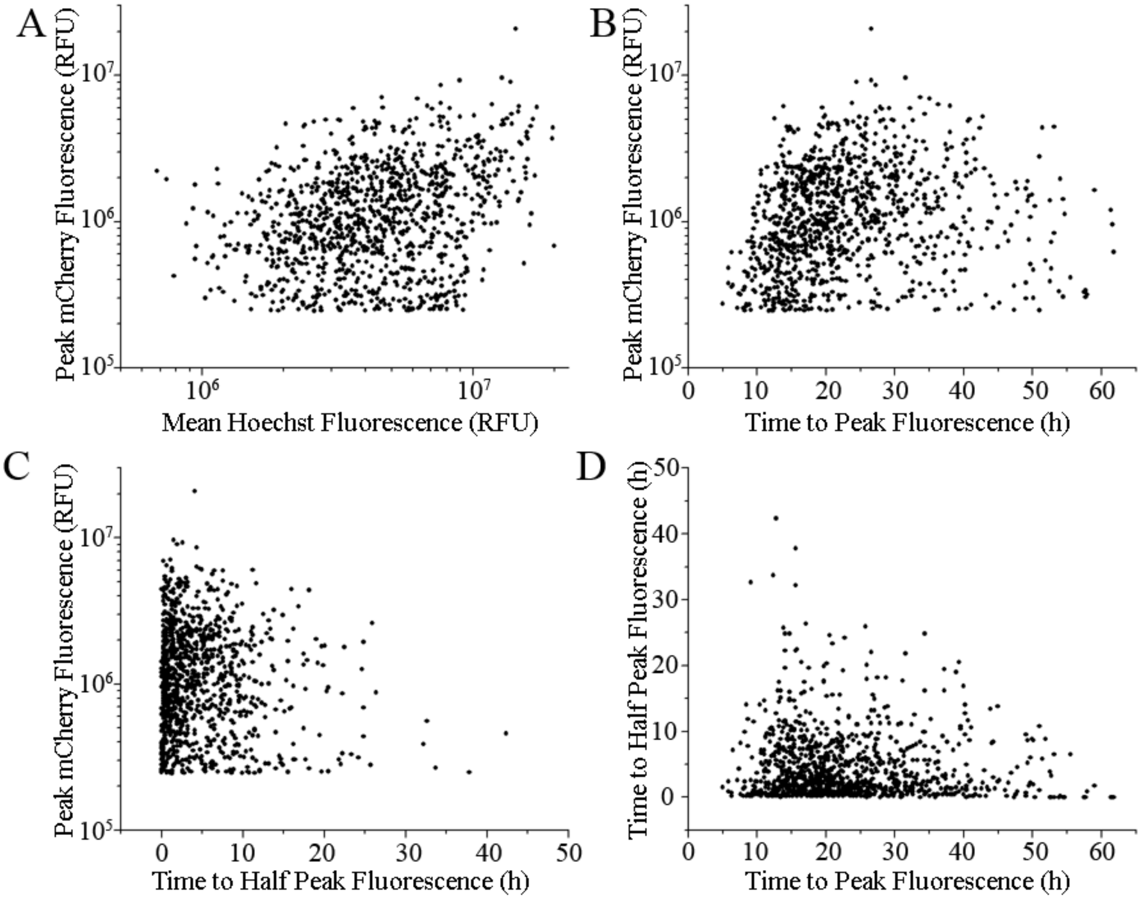

Figure 4.3. Comparisons between measured parameters from single-cell tracking of A375-BAR-mCherry cells (all 6 clones are shown pooled together) cultured on polystyrene after treatment with Wnt3a. (A) Peak mCherry fluorescence achieved versus the mean Hoechst fluorescence over the 62 h time-course ($r^2 = 0.09$) (B) Peak mCherry fluorescence versus the time required to reach peak fluorescence ($r^2 = 0.15$) (C) Peak mCherry fluorescence achieved versus the time required for signal to decay to half peak fluorescence ($r^2 = 0.01$) (D) The time required for signal to decay to half peak fluorescence versus the time required for cells to reach peak fluorescence ($r^2 = 0.006$).

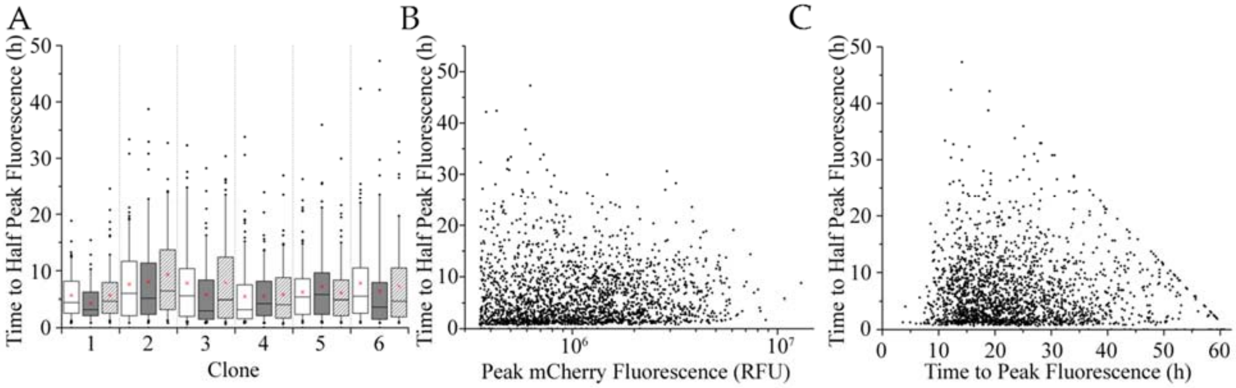

Figure 4.4. Characterization of BAR-mCherry reporter relaxation. Box and whisker plots showing the distributions of (A) the times to reach peak mCherry fluorescence, (B) the peak mCherry fluorescence intensity achieved and (C) the time required for signal to decay to half peak mCherry fluorescence for single A375-BAR-mCherry cells cultured on polystyrene (clear boxes), fibronectin (dark gray boxes) and gelatin (diagonal striped boxes). Red circles mark the population mean for each distribution. Outliers shown are observations above the 5th and below the 95th percentile. The boxes mark the 25th, 50th (median) and 75th percentiles within the distribution while the whiskers mark the 5th and 95th percentiles.

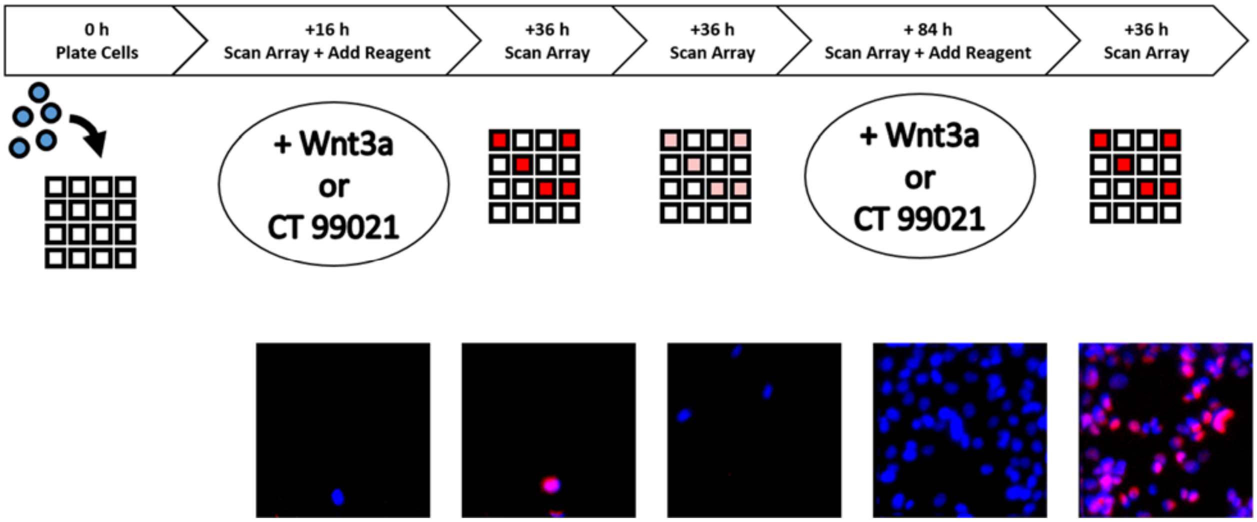

Figure 4.5. Process flow for the parallel clonogenic screen on the arrays. The experiment begins by seeding a single cell suspension of A375-BAR-mCherry cells onto the arrays. After 16 h the arrays are scanned to measure basal mCherry expression and then treated with either Wnt-3a or CT 99021. 36 h after treatment, the array is washed and scanned again to measure peak mCherry fluorescence activation. After an additional 36 h, the array is again scanned to track the relaxation of the mCherry signal. 84 h following the relaxation scan, the array is again scanned to confirm that the cells have reached basal activation levels and treated again with Wnt-3a or CT 99021. 36 h post-treatment, the arrays are washed and scanned again to measure peak mCherry fluorescence. Shown below the process flow is a series of images taken of a single clone over the course of the experiment. Hoechst 33342 and mCherry fluorescence is shown in blue and red, respectively.

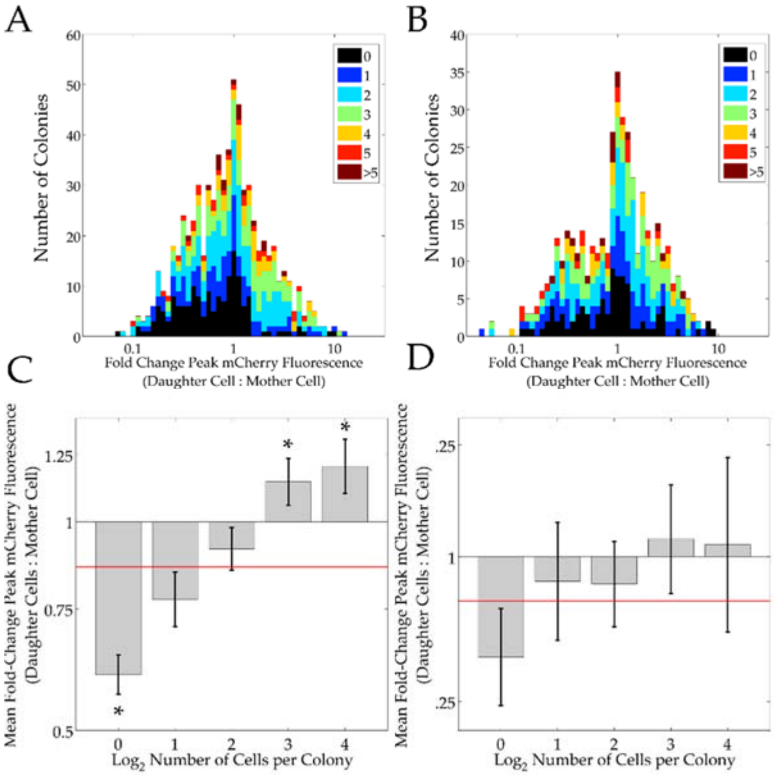

Figure 4.6. Distribution of the mean fold change in fluorescence density (RFU / pixel) between each clonal colony in the final time point and its corresponding mother cell for arrays treated with (A) Wnt-3a and (B) CT 99021. The bar color marks the nearest whole number of divisions each clonal colony underwent. Bar charts showing the mean fold-change for cells in each corresponding number of divisions for cells treated with (C) Wnt-3a and (D) CT 99021. Error bars show the standard error of the mean. Red line marks the total population mean. Asterisks mark populations found to be significantly different from the population mean ($p < 0.01$). Bars are not shown for colonies with >4 divisions due to an insufficient number of colonies greater than that size.

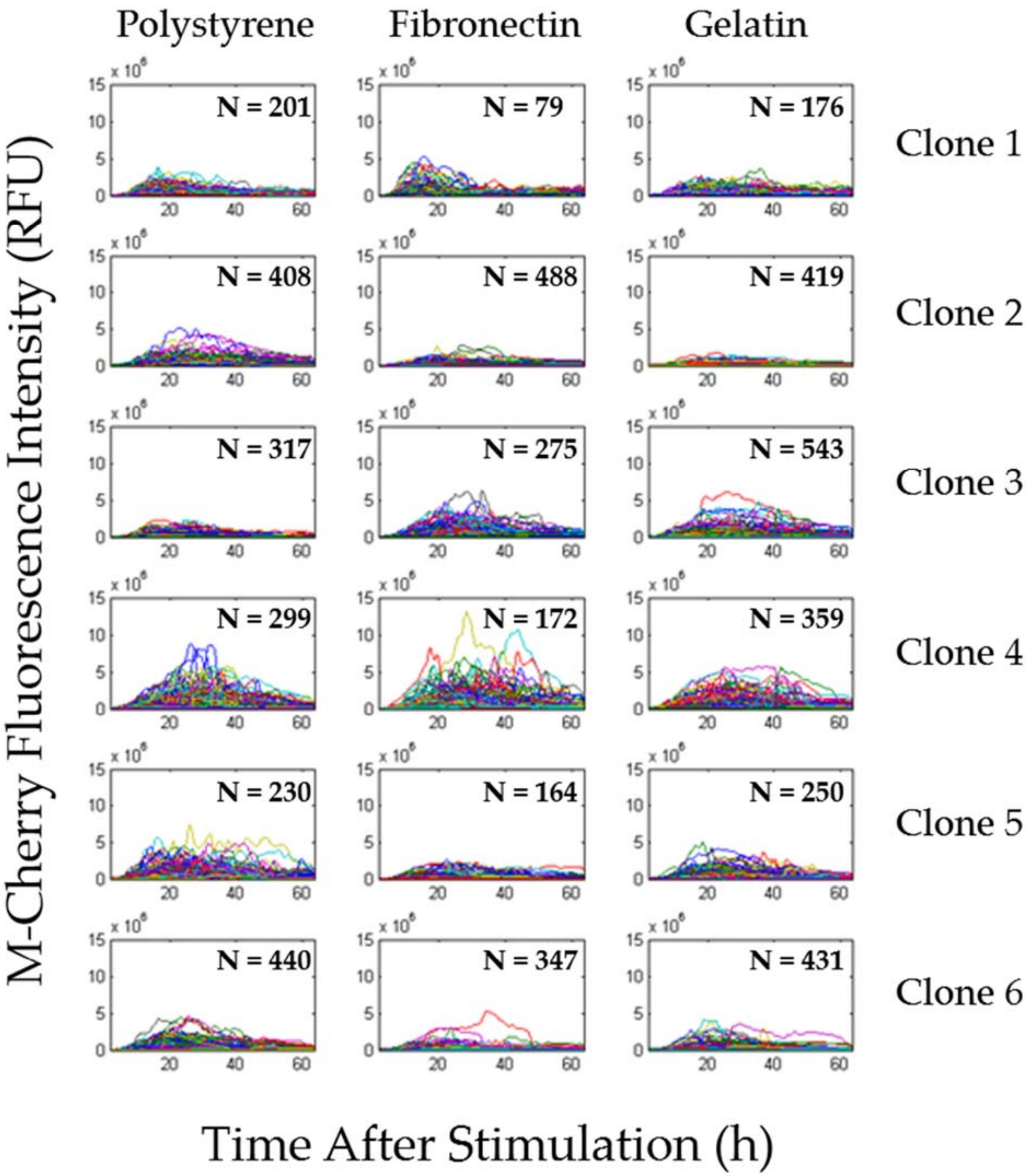

Figure 4.7. Traces showing the dynamics of mCherry fluorescence after stimulation of 6 clonal A375-BAR-mCherry cell lines with 1 μg/mL recombinant Wnt-3a for 2 h.

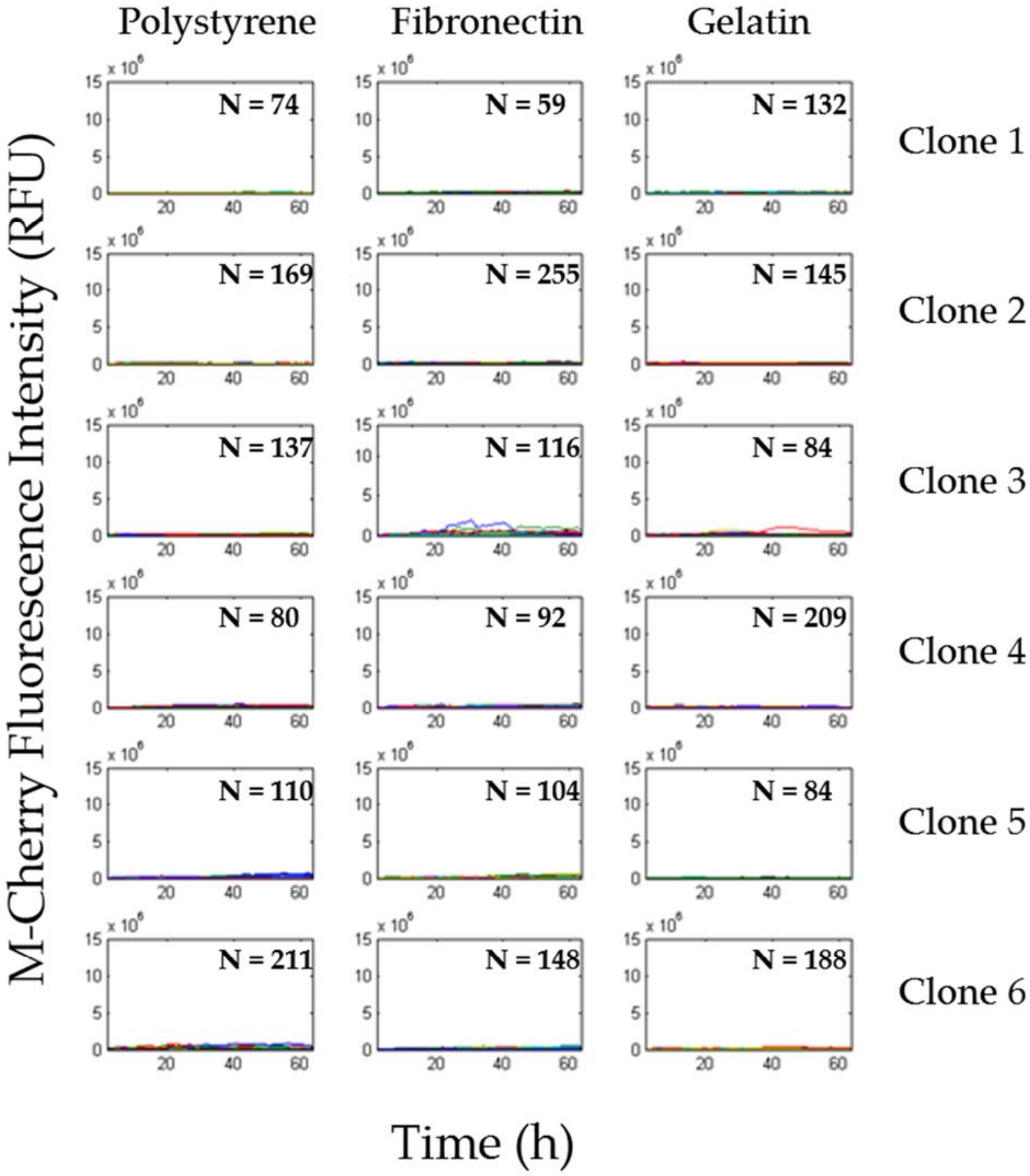

Figure 4.8. Traces showing measurement of mCherry fluorescence in control A375-BAR-mCherry cells treated with the vehicle for recombinant Wnt-3a (0.1% BSA in DI water stock concentration) for 2 h.

## 4.6 Tables

| | **Clone 1** | **Clone 2** | **Clone 3** | **Clone 4** | **Clone 5** | **Clone 6** |
|---|---|---|---|---|---|---|
| **Clone 1** | 1 | **1.14E-14** | 0.054695 | **5.74E-10** | **8.91E-09** | **3.74E-13** |
| **Clone 2** | **1.14E-14** | 1 | **5.49E-06** | **1.69E-29** | **2.05E-29** | **1.88E-22** |
| **Clone 3** | 0.054695 | **5.49E-06** | 1 | **3.77E-10** | **9.86E-10** | **4.37E-13** |
| **Clone 4** | **5.74E-10** | **1.69E-29** | **3.77E-10** | 1 | 0.155183 | 0.294269 |
| **Clone 5** | **8.91E-09** | **2.05E-29** | **9.86E-10** | 0.155183 | 1 | **0.000509** |
| **Clone 6** | **3.74E-13** | **1.88E-22** | **4.37E-13** | 0.294269 | **0.000509** | 1 |

Table 4.1. P-values for the two-tailed Wilcoxon rank sum test comparing the median peak reporter activation magnitude between each pair of clonal A375-BAR-mCherry cell lines cultured on polystyrene. Pair-wise comparisons that were found to be significant ($\alpha = 0.01$) are shown in bold.

| | **Clone 1** | **Clone 2** | **Clone 3** | **Clone 4** | **Clone 5** | **Clone 6** |
|---|---|---|---|---|---|---|
| **Clone 1** | 1 | **5.69E-05** | **0.000226** | **1.43E-10** | **3.65E-10** | **5.57E-06** |
| **Clone 2** | **5.69E-05** | 1 | 0.789757 | **0.006017** | 0.041012 | 0.495437 |
| **Clone 3** | **0.000226** | 0.789757 | 1 | 0.057556 | 0.174166 | 0.625638 |
| **Clone 4** | **1.43E-10** | **0.006017** | 0.057556 | 1 | 0.407026 | 0.113721 |
| **Clone 5** | **3.65E-10** | 0.041012 | 0.174166 | 0.407026 | 1 | 0.355528 |
| **Clone 6** | **5.57E-06** | 0.495437 | 0.625638 | 0.113721 | 0.355528 | 1 |

Table 4.2. P-values for the two-tailed Wilcoxon rank sum test comparing the median time to reach peak reporter activation between each pair of clonal A375-BAR-mCherry cell lines cultured on polystyrene. Pair-wise comparisons that were found to be significant ($\alpha = 0.01$) are shown in bold.

| | **Clone 1** | **Clone 2** | **Clone 3** | **Clone 4** | **Clone 5** | **Clone 6** |
|---|---|---|---|---|---|---|
| **Clone 1** | 1 | 0.057693 | 0.450691 | 0.038412 | 0.576431 | 0.099773 |
| **Clone 2** | 0.057693 | 1 | 0.740352 | **0.001893** | 0.169575 | 0.971958 |
| **Clone 3** | 0.450691 | 0.740352 | 1 | 0.044307 | 0.657881 | 0.787086 |
| **Clone 4** | 0.038412 | **0.001893** | 0.044307 | 1 | 0.010573 | **0.002302** |
| **Clone 5** | 0.576431 | 0.169575 | 0.657881 | 0.010573 | 1 | 0.246888 |
| **Clone 6** | 0.099773 | 0.971958 | 0.787086 | **0.002302** | 0.246888 | 1 |

Table 4.3 P-values for the two-tailed Wilcoxon rank sum test comparing the median time to reach half peak reporter activation between each pair of clonal A375-BAR-mCherry cell lines cultured on polystyrene. Pair-wise comparisons that were found to be significant (α = 0.01) are shown in bold.

| **Clone:** | **1** | **2** | **3** | **4** | **5** | **6** |
|---|---|---|---|---|---|---|
| Peak mCherry Fluorescence vs Mean Hoechst Fluorescence | 0.0342 | 0.0801 | 0.0932 | 0.1808 | 0.3903 | 0.0705 |
| Peak mCherry Fluorescence vs Time to Peak Fluorescence | 0.0008 | 0.0250 | 0.0156 | 0.0180 | 0.0004 | 0.0255 |
| Peak mCherry Fluorescence vs Time to Half Peak Fluorescence | 0.0001 | 0.0364 | 0.0355 | 0.0000 | 0.0047 | 0.0044 |
| Time to Peak Fluorescence vs Time to Half Peak Fluorescence | 0.0418 | 0.0162 | 0.0549 | 0.0012 | 0.0033 | 0.0078 |

Table 4.4. R2 values for parameter comparisons between control measurements made on single cells from each monoclonal population of A375-BAR-mCherry cells cultured on tissue culture polystyrene.

| **Clone** | **1** | **2** | **3** | **4** | **5** | **6** |
|---|---|---|---|---|---|---|
| PS vs Fbn | 0.015467 | 0.930512 | 0.067268 | 0.383456 | 0.469664 | 0.013488 |
| PS vs Gel | 0.683797 | 0.099148 | 0.856897 | 0.500818 | 0.55149 | 0.538264 |
| Fbn vs Gel | 0.048942 | 0.151066 | 0.043366 | 0.970127 | 0.249788 | 0.073528 |

Table 4.5. p-values for the two-tailed Wilcoxon rank sum test to evaluate the null hypothesis that the median times to reach half peak fluorescence are not different for each pair of cell culture substrates tested for each clone. At the $\alpha = 0.01$ level, the test failed to reject the null hypothesis for all comparisons.

| **Clone** | **1** | **2** | **3** | **4** | **5** | **6** |
|---|---|---|---|---|---|---|
| PS vs Fbn | 0.502104 | 0.275798 | 0.06618 | **0.00258** | 0.358901 | 0.341907 |
| PS vs Gel | 0.205828 | 0.284172 | 0.038567 | 0.793116 | 0.874622 | 0.411383 |
| Fbn vs Gel | 0.165635 | 0.048529 | **1.83E-05** | **0.005946** | 0.464554 | 0.657918 |

Table 4.6. P-values for the two-tailed Wilcoxon rank sum evaluating the null hypothesis that the median time to reach peak fluorescence for each test pair is not significantly different. The test failed to reject the null hypothesis for all but three cases for $\alpha = 0.01$ level. In clones 3 and 4, the median time to reach peak fluorescence for cells cultured on fibronectin was significantly longer than for cell cultured on gelatin and in clone 4 the median time was also significantly longer for cells cultured on fibronectin than for cells cultured on polystyrene.

| **Clone** | **1** | **2** | **3** | **4** | **5** | **6** |
|---|---|---|---|---|---|---|
| PS vs Fbn | 1.42E-08 | 0.00057 | 2.55E-09 | **0.0412** | 9.71E-06 | **0.0269** |
| PS vs Gel | **0.02896** | **0.66139** | 8.16E-05 | 0.0032 | 0.00011 | 1.34E-11 |
| Fbn vs Gel | 1.72E-05 | 2.41E-09 | 1.29E-18 | **0.96308** | **0.37721** | 4.76E-05 |

Table 4.7. p-values for the two-tailed Wilcoxon rank sum test to evaluate the null hypothesis that the median intensity of each pair of conditions is not statistically significantly different. Values that fail to reject the null hypothesis at the $\alpha = 0.01$ level are shown in bold.

| **Clone** | **1** | **2** | **3** | **4** | **5** | **6** |
|---|---|---|---|---|---|---|
| PS | 7.10E-09 | 2.86E-04 | 1.27E-09 | **0.0206** | **1** | **0.987** |
| Gel | 8.59E-06 | 1.20E-09 | 6.47E-19 | **0.519** | **0.812** | 2.38E-05 |

Table 4.8. p-values for the single-tailed Wilcoxon rank sum test to evaluate the null hypothesis that the median intensity of the fibronectin distribution is not greater than the median intensities of PS or Gel. At the α = 0.01 level, the rank sum test shows a statistically significantly higher median fluorescence intensity for Clones 1-3 when cultured on fibronectin than either of the alternate substrates and a high median fluorescence intensity for Clone 6 when cultured on fibronectin than on gelatin.

| **Format** | **Ideal Clonal Yield** | **Media Consumption per Clone (mL)** | **Wnt-3a Consumption per clone (µg)** |
|---|---|---|---|
| 384-well plate | 141 ± 12 | 1.305 | 0.435 |
| Cell Array | 4,047 ± 64 | 0.006 | 0.002 |
| Reduction | | 99.5% | 99.5% |

Table 4.9. Comparison of reagent consumption and clonal yield of screening performed using conventional 384 well plates and a 1 $in^2$ cell array containing 12,100 elements. Expected clonal yield was estimated using the Poisson distribution for a seeding ratio of 1 cell per well or array element; the error shown is the standard deviation of the Poisson distribution for the corresponding mean. Media consumption was calculated for 6 exchanges of 80 µL per well for the 384 well plate and 4 mL per cell array. Wnt-3a consumption was calculated for two 80 µL doses of 1 µg/mL Wnt-3a for the 384 well plate and two 4 mL doses for the cell array.

## 4.7 References

1. Berndt, J. D., Biechele, T. L., Moon, R. T. & Major, M. B. Integrative analysis of genome-wide RNA interference screens. *Sci. Signal.* **2,** pt4 (2009).

2. James, R. G., Biechele, T. L., Conrad, W. H., Camp, N. D., Fass, D. M., Major, M. B., Sommer, K., Yi, X., Roberts, B. S., Cleary, M. A., Arthur, W. T., MacCoss, M., Rawlings, D. J., Haggarty, S. J. & Moon, R. T. Bruton's tyrosine kinase revealed as a negative regulator of Wnt-beta-catenin signaling. *Sci. Signal.* **2,** ra25 (2009).

3. Chung, N., Marine, S., Smith, E. A., Liehr, R., Smith, S. T., Locco, L., Hudak, E., Kreamer, A., Rush, A., Roberts, B., Major, M. B., Moon, R. T., Arthur, W., Cleary, M., Strulovici, B. & Ferrer, M. A 1,536-well ultra-high-throughput siRNA screen to identify regulators of the Wnt/beta-catenin pathway. *Assay Drug Dev. Technol.* **8,** 286–94 (2010).

4. Major, M. B., Roberts, B. S., Berndt, J. D., Marine, S., Anastas, J., Chung, N., Ferrer, M., Yi, X., Stoick-Cooper, C. L., von Haller, P. D., Kategaya, L., Chien, A., Angers, S., MacCoss, M., Cleary, M. a, Arthur, W. T. & Moon, R. T. New regulators of Wnt/beta-catenin signaling revealed by integrative molecular screening. *Sci. Signal.* **1,** ra12 (2008).

5. Vermeulen, L., De Sousa E Melo, F., van der Heijden, M., Cameron, K., de Jong, J. H., Borovski, T., Tuynman, J. B., Todaro, M., Merz, C., Rodermond, H., Sprick, M. R., Kemper, K., Richel, D. J., Stassi, G. & Medema, J. P. Wnt activity defines colon cancer stem cells and is regulated by the microenvironment. *Nat. Cell Biol.* **12,** 468–76 (2010).

6. Navin, N., Kendall, J., Troge, J., Andrews, P., Rodgers, L., McIndoo, J., Cook, K., Stepansky, A., Levy, D., Esposito, D., Muthuswamy, L., Krasnitz, A., McCombie, W. R., Hicks, J. & Wigler, M. Tumour evolution inferred by single-cell sequencing. *Nature* **472,** 90–4 (2011).

7. Almendro, V., Marusyk, A. & Polyak, K. Cellular heterogeneity and molecular evolution in cancer. *Annu. Rev. Pathol.* **8,** 277–302 (2013).

8. Hou, Y., Song, L., Zhu, P., Zhang, B., Tao, Y., Xu, X., Li, F., Wu, K., Liang, J., Shao, D., Wu, H., Ye, X., Ye, C., Wu, R., Jian, M., Chen, Y., Xie, W., Zhang, R., Chen, L., Liu, X., Yao, X., Zheng, H., Yu, C., Li, Q., Gong, Z., Mao, M., Yang, X., Yang, L.,

Li, J., Wang, W., Lu, Z., Gu, N., Laurie, G., Bolund, L., Kristiansen, K., Wang, J., Yang, H., Li, Y., Zhang, X. & Wang, J. Single-Cell Exome Sequencing and Monoclonal Evolution of a JAK2-Negative Myeloproliferative Neoplasm. *Cell* **148,** 873–885 (2012).

9. Anderson, A. R. A., Weaver, A. M., Cummings, P. T. & Quaranta, V. Tumor Morphology and Phenotypic Evolution Driven by Selective Pressure from the Microenvironment. *Cell* **127,** 905–915 (2006).

10. Zaslaver, A., Bren, A., Ronen, M., Itzkovitz, S., Kikoin, I., Shavit, S., Liebermeister, W., Surette, M. G. & Alon, U. A comprehensive library of fluorescent transcriptional reporters for Escherichia coli. *Nat. Methods* **3,** 623–8 (2006).

11. Major, M. B., Roberts, B. S., Berndt, J. D., Marine, S., Anastas, J., Chung, N., Ferrer, M., Yi, X., Stoick-Cooper, C. L., von Haller, P. D., Kategaya, L., Chien, A., Angers, S., MacCoss, M., Cleary, M. A., Arthur, W. T. & Moon, R. T. New regulators of Wnt/beta-catenin signaling revealed by integrative molecular screening. *Sci. Signal.* **1,** ra12 (2008).

12. Su, G. H., Sohn, T. A., Ryu, B. & Kern, S. E. A Novel Histone Deacetylase Inhibitor Identified by High-Throughput Transcriptional Screening of a Compound Library. *Cancer Res.* **60,** 3137–3142 (2000).

13. Biechele, T. L., Adams, A. M. & Moon, R. T. Transcription-based reporters of Wnt/beta-catenin signaling. *Cold Spring Harb. Protoc.* **2009,** pdb.prot5223 (2009).

14. Kobayashi, M., Honma, T., Matsuda, Y., Suzuki, Y., Narisawa, R., Ajioka, Y. & Asakura, H. Nuclear translocation of beta-catenin in colorectal cancer. *Br. J. Cancer* **82,** 1689–93 (2000).

15. Goentoro, L. & Kirschner, M. W. Evidence that fold-change, and not absolute level, of beta-catenin dictates Wnt signaling. *Mol. Cell* **36,** 872–84 (2009).

16. Kam, Y. & Quaranta, V. Cadherin-bound beta-catenin feeds into the Wnt pathway upon adherens junctions dissociation: evidence for an intersection between beta-catenin pools. *PLoS One* **4,** e4580 (2009).

17. Biechele, T. L. & Moon, R. T. Assaying beta-catenin/TCF transcription with beta-catenin/TCF transcription-based reporter constructs. *Methods Mol. Biol.* **468,** 99–110 (2008).

18. Biechele, T. L., Camp, N. D., Fass, D. M., Kulikauskas, R. M., Robin, N. C., White, B. D., Taraska, C. M., Moore, E. C., Muster, J., Karmacharya, R., Haggarty, S. J., Chien, A. J. & Moon, R. T. Chemical-Genetic Screen Identifies Riluzole as an Enhancer of Wnt/β-catenin Signaling in Melanoma. *Chem. Biol.* **17,** 1177–1182 (2010).

19. Bartfeld, S., Hess, S., Bauer, B., Machuy, N., Ogilvie, L. A., Schuchhardt, J. & Meyer, T. F. High-throughput and single-cell imaging of NF-kappaB oscillations using monoclonal cell lines. *BMC Cell Biol.* **11,** 21 (2010).

20. King, K. R., Wang, S., Irimia, D., Jayaraman, A., Toner, M. & Yarmush, M. L. A high-throughput microfluidic real-time gene expression living cell array. *Lab Chip* **7,** 77–85 (2007).

21. Ji, L. L., Sheng, Y. C., Chen, L. & Wang, Z. T. Establishment of a new cell line for high-throughput evaluation of chemokine CCR5 receptor antagonists. *Drug Discov. Ther.* **3,** 2–5 (2009).

22. Durocher, Y., Perret, S., Thibaudeau, E., Gaumond, M. H., Kamen, A., Stocco, R. & Abramovitz, M. A reporter gene assay for high-throughput screening of G-protein-coupled receptors stably or transiently expressed in HEK293 EBNA cells grown in suspension culture. *Anal. Biochem.* **284,** 316–26 (2000).

23. Li, X., Shen, F., Zhang, Y., Zhu, J., Huang, L. & Shi, Q. Functional characterization of cell lines for high-throughput screening of human neuromedin U receptor subtype 2 specific agonists using a luciferase reporter gene assay. *Eur. J. Pharm. Biopharm.* **67,** 284–92 (2007).

24. Giard, D. J., Aaronson, S. A., Todaro, G. J., Arnstein, P., Kersey, J. H., Dosik, H. & Parks, W. P. In vitro cultivation of human tumors: establishment of cell lines derived from a series of solid tumors. *J. Natl. Cancer Inst.* **51,** 1417–23 (1973).

25. Widlund, H. R., Horstmann, M. A., Price, E. R., Cui, J., Lessnick, S. L., Wu, M., He, X. & Fisher, D. E. Beta-catenin-induced melanoma growth requires the downstream target Microphthalmia-associated transcription factor. *J. Cell Biol.* **158,** 1079–87 (2002).

26. Wang, Y., Phillips, C., Xu, W., Pai, J.-H., Dhopeshwarkar, R., Sims, C. E. & Allbritton, N. Micromolded arrays for separation of adherent cells. *Lab Chip* **10,** 2917–24 (2010).

27. Edelstein, A., Amodaj, N., Hoover, K., Vale, R. & Stuurman, N. Computer control of microscopes using μManager. *Curr. Protoc. Mol. Biol.* **Chapter 14,** Unit14.20 (2010).

28. Carpenter, A. E., Jones, T. R., Lamprecht, M. R., Clarke, C., Kang, I. H., Friman, O., Guertin, D. A., Chang, J. H., Lindquist, R. A., Moffat, J., Golland, P. & Sabatini, D. M. CellProfiler: image analysis software for identifying and quantifying cell phenotypes. *Genome Biol.* **7,** R100 (2006).

29. Otsu, N. A Threshold Selection Method from Gray-Level Histograms. *IEEE Trans. Syst. Man. Cybern.* **9,** 62–66 (1979).

30. Shah, P. K., Hughes, M. R., Wang, Y., Sims, C. E. & Allbritton, N. L. Scalable synthesis of a biocompatible, transparent and superparamagnetic photoresist for microdevice fabrication. *J. Micromechanics Microengineering* **23,** 107002 (2013).

31. Wang, Y., Bachman, M., Sims, C. E., Li, G. P. & Allbritton, N. L. Stability of virtual air walls on micropallet arrays. *Anal. Chem.* **79,** 7104–9 (2007).

32. Hadjihannas, M. V, Bernkopf, D. B., Brückner, M. & Behrens, J. Cell cycle control of Wnt/β-catenin signalling by conductin/axin2 through CDC20. *EMBO Rep.* **13,** 347–54 (2012).

33. Davidson, G., Shen, J., Huang, Y.-L., Su, Y., Karaulanov, E., Bartscherer, K., Hassler, C., Stannek, P., Boutros, M. & Niehrs, C. Cell cycle control of wnt receptor activation. *Dev. Cell* **17,** 788–99 (2009).

34. Adams, J. Potential for proteasome inhibition in the treatment of cancer. *Drug Discov. Today* **8,** 307–315 (2003).

35. Almond, J. B. & Cohen, G. M. The proteasome: a novel target for cancer chemotherapy. *Leukemia* **16,** 433–43 (2002).

36. Adams, J., Palombella, V. J. & Elliott, P. J. Proteasome Inhibition: a New Strategy in Cancer Treatment. *Invest. New Drugs* **18,** 109–121 (2000).

37. Liu, Y., Chattopadhyay, N., Qin, S., Szekeres, C., Vasylyeva, T., Mahoney, Z. X., Taglienti, M., Bates, C. M., Chapman, H. A., Miner, J. H. & Kreidberg, J. A. Coordinate integrin and c-Met signaling regulate Wnt gene expression during epithelial morphogenesis. *Development* **136,** 843–53 (2009).

38. Crampton, S. P., Wu, B., Park, E. J., Kim, J.-H., Solomon, C., Waterman, M. L. & Hughes, C. C. W. Integration of the beta-catenin-dependent Wnt pathway with integrin signaling through the adaptor molecule Grb2. *PLoS One* **4,** e7841 (2009).

39. Olivares-Navarrete, R., Hyzy, S. L., Park, J. H., Dunn, G. R., Haithcock, D. A., Wasilewski, C. E., Boyan, B. D. & Schwartz, Z. Mediation of osteogenic differentiation of human mesenchymal stem cells on titanium surfaces by a Wnt-integrin feedback loop. *Biomaterials* **32,** 6399–411 (2011).

40. De Toni, F., Racaud-Sultan, C., Chicanne, G., Mas, V. M.-D., Cariven, C., Mesange, F., Salles, J.-P., Demur, C., Allouche, M., Payrastre, B., Manenti, S. & Ysebaert, L. A crosstalk between the Wnt and the adhesion-dependent signaling pathways governs the chemosensitivity of acute myeloid leukemia. *Oncogene* **25,** 3113–22 (2006).

41. Hughes, P., Marshall, D., Reid, Y., Parkes, H. & Gelber, C. The costs of using unauthenticated, over-passaged cell lines: how much more data do we need? *Biotechniques* **43,** 575–586 (2007).

42. Masters, J. R. Human cancer cell lines: fact and fantasy. *Nat. Rev. Mol. Cell Biol.* **1,** 233–6 (2000).

43. Wang, Y., Young, G., Aoto, P. C., Pai, J.-H., Bachman, M., Li, G. P., Sims, C. E. & Allbritton, N. L. Broadening cell selection criteria with micropallet arrays of adherent cells. *Cytometry. A* **71,** 866–74 (2007).

44. Quinto-Su, P. a, To'a Salazar, G., Sims, C. E., Allbritton, N. L. & Venugopalan, V. Mechanisms of pulsed laser microbeam release of SU-8 polymer "micropallets" for the collection and separation of adherent cells. *Anal. Chem.* **80,** 4675–9 (2008).

45. Salazar, G. T., Wang, Y., Young, G., Bachman, M., Sims, C. E., Li, G. P. & Allbritton, N. L. Micropallet arrays for the separation of single, adherent cells. *Anal. Chem.* **79,** 682–7 (2007).

46. Martinez, E. J., Owa, T., Schreiber, S. L. & Corey, E. J. Phthalascidin, a synthetic antitumor agent with potency and mode of action comparable to ecteinascidin 743. *Proc. Natl. Acad. Sci.* **96,** 3496–3501 (1999).

47. Piddini, E. & Vincent, J.-P. Interpretation of the Wingless Gradient Requires Signaling-Induced Self-Inhibition. *Cell* **136,** 296–307 (2009).

48. Hoang, B. H. Dickkopf 3 Inhibits Invasion and Motility of Saos-2 Osteosarcoma Cells by Modulating the Wnt- -Catenin Pathway. *Cancer Res.* **64,** 2734–2739 (2004).

49. Latres, E., Chiaur, D. S. & Pagano, M. The human F box protein beta-Trcp associates with the Cul1/Skp1 complex and regulates the stability of beta-catenin. *Oncogene* **18,** 849–54 (1999).

50. Jho, E. -h., Zhang, T., Domon, C., Joo, C.-K., Freund, J.-N. & Costantini, F. Wnt/ -Catenin/Tcf Signaling Induces the Transcription of Axin2, a Negative Regulator of the Signaling Pathway. *Mol. Cell. Biol.* **22,** 1172–1183 (2002).

51. Rasola, A., Fassetta, M., De Bacco, F., D'Alessandro, L., Gramaglia, D., Di Renzo, M. F. & Comoglio, P. M. A positive feedback loop between hepatocyte growth factor receptor and beta-catenin sustains colorectal cancer cell invasive growth. *Oncogene* **26,** 1078–87 (2007).

52. Kim, D., Rath, O., Kolch, W. & Cho, K.-H. A hidden oncogenic positive feedback loop caused by crosstalk between Wnt and ERK pathways. *Oncogene* **26,** 4571–9 (2007).

53. Kapinas, K., Kessler, C., Ricks, T., Gronowicz, G. & Delany, A. M. miR-29 modulates Wnt signaling in human osteoblasts through a positive feedback loop. *J. Biol. Chem.* **285,** 25221–31 (2010).

54. Kang, D. W., Lee, S.-H., Yoon, J. W., Park, W.-S., Choi, K.-Y. & Min, D. S. Phospholipase D1 drives a positive feedback loop to reinforce the Wnt/beta-catenin/TCF signaling axis. *Cancer Res.* **70,** 4233–42 (2010).

55. Monga, S. P. S., Mars, W. M., Pediaditakis, P., Bell, A., Mule, K., Bowen, W. C., Wang, X., Zarnegar, R. & Michalopoulos, G. K. Hepatocyte Growth Factor Induces Wnt-independent Nuclear Translocation of {beta}-Catenin after Met-{beta}-Catenin Dissociation in Hepatocytes. *Cancer Res.* **62,** 2064–2071 (2002).

56. Cho, J.-H., Dimri, M. & Dimri, G. P. A positive feedback loop regulates the expression of polycomb group protein BMI1 via WNT signaling pathway. *J. Biol. Chem.* **288,** 3406–18 (2013).

57. Hoeben, R. C., Migchielsen, A. A., van der Jagt, R. C., van Ormondt, H. & van der Eb, A. J. Inactivation of the Moloney murine leukemia virus long terminal repeat in

murine fibroblast cell lines is associated with methylation and dependent on its chromosomal position. *J. Virol.* **65,** 904–912 (1991).

58. Lecault, V., Vaninsberghe, M., Sekulovic, S., Knapp, D. J. H. F., Wohrer, S., Bowden, W., Viel, F., McLaughlin, T., Jarandehei, A., Miller, M., Falconnet, D., White, A. K., Kent, D. G., Copley, M. R., Taghipour, F., Eaves, C. J., Humphries, R. K., Piret, J. M. & Hansen, C. L. High-throughput analysis of single hematopoietic stem cell proliferation in microfluidic cell culture arrays. *Nat. Methods* **8,** 581–6 (2011).

59. Mueller, D. L., Jenkins, M. K. & Schwartz, R. H. An accessory cell-derived costimulatory signal acts independently of protein kinase C activation to allow T cell proliferation and prevent the induction of unresponsiveness. *J. Immunol.* **142,** 2617–28 (1989).

60. Cloutier, J.-F. & Veillette, A. Cooperative Inhibition of T-Cell Antigen Receptor Signaling by a Complex between a Kinase and a Phosphatase. *J. Exp. Med.* **189,** 111–121 (1999).

# Chapter 5: Conclusions

The primary goal of the work presented in this dissertation was the development of an integrated platform for sorting single adherent cells and colonies based on imaging cytometry measurements. Towards this goal an imaging cytometry platform was developed which incorporated micropallet array technology with automated microscope control and imaging as a flexible base upon which applications of imaging cytometry and micropallet array sorting could be implemented. While sorting capabilities of the designed system are currently limited only to micropallet arrays, the cytometry functions of the platform can be applied to a variety of microfabricated array modalities including microwell arrays and microraft arrays. Indeed, one of the key areas for future development of this platform will be the incorporation of functionality allowing for the automated release and collection of microrafts.

The work presented here covered three major aspects of developing and demonstrating this integrated platform including materials development (Chapter 2), system development and integration (Chapter 3) and the demonstration of the unique capabilities of micropallet-array based cytometry (Chapter 4).

## 5.1 The Development of a Novel Magnetic Photoresist for Micropallet Fabrication

While the primary goal of the work presented in Chapter 2 was to develop a scalable synthesis for a magnetic photoresist that could be used for micropallet array fabrication, the material developed has broader applications in the fabrication of magnetically active microdevices. Three key performance parameters were essential to the success of this material: optical clarity, tissue culture biocompatibility and magnetic functionalization.

Development of an optically clear photoresist depended on the sTable 4.dispersion of the magnetic colloid into the base photoresist. This proved challenging due to the incompatibility of solvent systems commonly utilized in nanoparticle synthesis and GBL, the solvent system used in the 1002F base photoresist. This was surmounted through a surface ligand exchange which replaced the hydrophobic coating used in the nanoparticle synthesis with a polymeric matrix comprised of PMMA/MMA which is soluble in GBL.[1] PMMA/MMA was selected due to its excellent optical properties, demonstrated biocompatibility and the presence of epoxy-reactive carboxylic acid side-groups which would allow it to cross-link with the 1002F base photoresist. DSC confirmed the hypothesis that PMMA/MMA will form a single phase with 1002F and characterization of the resulting composite photoresist showed excellent photolithographic performance, achieving aspect ratios >10. MTT assays showed no significant effect on the metabolism of HeLa cells when grown on the new composite PMMA/1002F photoresist relative to glass. Primary murine mesenchymal stem cells were also shown to exhibit typical morphologies when cultured on the PMMA/1002F composite. The magnetic functionalization of the PMMA/1002F photoresist was also demonstrated by fabricating a micropallet array using it and successfully releasing clonal colonies of fluorescent HeLa cells (HeLa-H2B-GFP) from the array and collecting the released colonies against gravity using a solid state magnet. The excellent optical, mechanical and magnetic properties of the PMMA/1002F composite, as well as its excellent biocompatibility, made it a useful tool in microdevice fabrication.

## 5.2 Micropallet Array Scan and Release Automation

The integration of micropallet array technology into an imaging cytometry platform require the development of three components: a fully computerized microscope platform, a software utility for the automated imaging of microfabricated cell arrays and a software utility for the automated release of individual micropallets from an array. The first component was built using off-the-shelf components and incorporated a motorized microscope frame, motorized stage, computer-controlled shutters and cooled CCD camera. Both software utilities were developed using a common framework which relied upon the user to provide the data required to register a microfabricated array to the microscope's stage coordinate system. The array's geometry was first registered in the XY plane by the user-assisted location of two opposing corners of the array and the input of the array's physical geometry (number of rows and columns and the size and spacing of the array's elements). From this information the position of every element within the array could interpolated to within 3 μm, an accepTable 4.error when considering the resolution of low magnification microscope objectives and the repeatability of motorized stage positioning. The array's orientation in the Z plane was then registered through the user initialization of a set of guide points. With a minimum of 4 points in the array located in X, Y and Z coordinates, a plane of best fit could be calculated using the singular value decomposition of the initialized positions. The flatness of the array surface meant that errors in the focus plane calculated were typically within the depth of focus of the objective utilized (<2 μm). With the initialization of these two data, the array could be rapidly scanned in an automated fashion by navigating to each calculated field of view within the array. To simplify image analysis and data processing, the image acquired at each field of view was segmented based on the interpolated position and the user-provided size of each micropallet and an individual image of each micropallet was saved. Metadata relating the relative position of each micropallet with the array was stored in the image filename, allowing data from multiple scans to be co-registered. The automation of micropallet array scanning and release was demonstrated with a simple application in which EpCAM+ cancer cells from a PDX tissue sample were purified from a background of EpCAM- contamination. This purification would be challenging to perform using conventional FACS and MACS due to the extremely small numbers of viable cell yielded from the PDX tissue samples. With micropallet arrays, however, three samples of 7,584, 1,087 and 875 cells each were successfully sorted, yielding 257, 16 and 7 EpCAM+ cells, respectively. Image analysis for this application was performed using a CellProfiler pipeline for segmentation and achieved a false-negative rate of 1%, 0% and 0% for the three sample sorted and a false-positive rate of 0%, 8% and 9%. This performance far exceeds that of MACS and FACS for samples 10× as large[2] demonstrating both the value of micropallet-array based isolations for small tissue samples that are often produced by animal model research and primary tissue biopsies as well as the successful integration of both automated imaging and automated release for micropallet arrays.

## 5.3 Massively Parallel Clonogenic Screening with Micropallet Arrays

Advances in high throughput screening approaches and the development of robust transcriptional reporters for signaling have accelerated the pace of discovery for targeted therapies for cancer.[3–5] The performance of these screens is highly dependent on the dynamic range and variability of the reporter utilized. While significant improvements have been made to luminescence and fluorescence-based readouts, little is understood about the dynamics of transcriptional reporter evolution. A common approach to reducing variability in transcriptional reporter cell lines is to generate monoclonal populations. Several groups have published data showing the emergence of heterogeneity in monoclonal cell lines[6–9], and evidence exists for epigenetic silencing of reporter genes play a role[10]. In order to better understand the dynamics of the reporter evolution process, 6 monoclonal reporter cell lines were developed using microraft array cloning of a cell line bearing a transcriptional for β-catenin signaling (BAR-mCherry). These clonal cell lines were then stimulated with recombinant Wnt3a and the single-cell dynamics of signal activation and relaxation quantified. Single-cell tracking revealed distinct signaling phenotypes present in the monoclonal populations and a dependency of both signaling kinetics and magnitude on ECM-mediated signaling. In order to characterize a larger number of clones to better capture the dynamics of the original polyclonal cell line, micropallet arrays were used to conduct a massively parallel clonogenic screen. Single A375-BAR-mCherry cells seeded onto micropallet arrays were stimulated with either recombinant Wnt-3a or CT 99021, an inhibitor of GSK3β. The peak activation magnitude was measured of the individual cells after stimulation for 36 h and the stimulus was removed. After 5 days of expansion, the clonal colonies which grew from the individual mother cells were assayed in the same fashion. The screen revealed a 100-fold difference in the overall population in the range of the change in signaling magnitude relative to the mother cells within 6 rounds of cell division. Additionally, self-inhibitory signaling was directly observed in cells stimulated with Wnt-3a that remained viable but non-proliferative during the 5 day expansion period. This self-inhibition disappeared in cells that divided and colonies that had passed 3 divisions exhibited positive feedback in signaling relative to their mother cells. The conclusion that the positive and negative feedback processes that were observed were not reporter artifacts is supported by the lack of an observed trend in colonies treated with CT 99021 which would bypass mechanisms of positive and negative feedback for Wnt-mediated β-catenin signaling described in the literature.[11–16]

In addition to these biological observations, this work suggests that phenotypic homogeneity rather than genotypic homogeneity is more important for the optimization of reporter systems in high throughput screening. Monoclonal selection will likely not only fail to reduce heterogeneous signaling intensity, but may bias the assay or screen due to the inclusion of an atypical signaling phenotype. Micropallet arrays were a key enabling technology in the performance of this clonogenic screen. Performing the same assay in a conventional multiwall format would need an average of 3,042 wells to be seeded, consuming eight 384-well plates, 1.2 L of culture media and 245.8 µg of Wnt-3a. Additionally, the micropallet array format allows for characterized clones to be sorted for further analysis, enabling future investigations into the molecular, genetic and epigenetic modulation of β-catenin signaling and the role that cell division may play in the mediation of positive and negative feedback.

## 5.4 References

1. Shah, P. K., Hughes, M. R., Wang, Y., Sims, C. E. & Allbritton, N. L. Scalable synthesis of a biocompatible, transparent and superparamagnetic photoresist for microdevice fabrication. *J. Micromechanics Microengineering* **23,** 107002 (2013).

2. Xu, W., Sims, C. E. & Allbritton, N. L. Microcup arrays for the efficient isolation and cloning of cells. *Anal. Chem.* **82,** 3161–7 (2010).

3. Kain, S. R. Green fluorescent protein (GFP): applications in cell-based assays for drug discovery. *Drug Discov. Today* **4,** 304–312 (1999).

4. Croston, G. E. Functional cell-based uHTS in chemical genomic drug discovery. *Trends Biotechnol.* **20,** 110–115 (2002).

5. Mere, L., Bennett, T., Coassin, P., England, P., Hamman, B., Rink, T., Zimmerman, S. & Negulescu, P. Miniaturized FRET assays and microfluidics: key components for ultra-high-throughput screening. *Drug Discov. Today* **4,** 363–369 (1999).

6. Navin, N., Kendall, J., Troge, J., Andrews, P., Rodgers, L., McIndoo, J., Cook, K., Stepansky, A., Levy, D., Esposito, D., Muthuswamy, L., Krasnitz, A., McCombie, W. R., Hicks, J. & Wigler, M. Tumour evolution inferred by single-cell sequencing. *Nature* **472,** 90–94 (2011).

7. Hou, Y., Song, L., Zhu, P., Zhang, B., Tao, Y., Xu, X., Li, F., Wu, K., Liang, J., Shao, D., Wu, H., Ye, X., Ye, C., Wu, R., Jian, M., Chen, Y., Xie, W., Zhang, R., Chen, L., Liu, X., Yao, X., Zheng, H., Yu, C., Li, Q., Gong, Z., Mao, M., Yang, X., Yang, L., Li, J., Wang, W., Lu, Z., Gu, N., Laurie, G., Bolund, L., Kristiansen, K., Wang, J., Yang, H., Li, Y., Zhang, X. & Wang, J. Single-Cell Exome Sequencing and Monoclonal Evolution of a JAK2-Negative Myeloproliferative Neoplasm. *Cell* **148,** 873–885 (2012).

8. Bartfeld, S., Hess, S., Bauer, B., Machuy, N., Ogilvie, L. A., Schuchhardt, J. & Meyer, T. F. High-throughput and single-cell imaging of NF-kappaB oscillations using monoclonal cell lines. *BMC Cell Biol.* **11,** 21 (2010).

9. Vermeulen, L., De Sousa E Melo, F., van der Heijden, M., Cameron, K., de Jong, J. H., Borovski, T., Tuynman, J. B., Todaro, M., Merz, C., Rodermond, H., Sprick, M. R., Kemper, K., Richel, D. J., Stassi, G. & Medema, J. P. Wnt activity defines colon cancer stem cells and is regulated by the microenvironment. *Nat. Cell Biol.* **12,** 468–76 (2010).

10. Hoeben, R. C., Migchielsen, A. A., van der Jagt, R. C., van Ormondt, H. & van der Eb, A. J. Inactivation of the Moloney murine leukemia virus long terminal repeat in murine fibroblast cell lines is associated with methylation and dependent on its chromosomal position. *J. Virol.* **65,** 904–912 (1991).

11. Cho, J.-H., Dimri, M. & Dimri, G. P. A positive feedback loop regulates the expression of polycomb group protein BMI1 via WNT signaling pathway. *J. Biol. Chem.* **288,** 3406–18 (2013).

12. Kim, D., Rath, O., Kolch, W. & Cho, K.-H. A hidden oncogenic positive feedback loop caused by crosstalk between Wnt and ERK pathways. *Oncogene* **26,** 4571–9 (2007).

13. Rasola, A., Fassetta, M., De Bacco, F., D'Alessandro, L., Gramaglia, D., Di Renzo, M. F. & Comoglio, P. M. A positive feedback loop between hepatocyte growth factor receptor and beta-catenin sustains colorectal cancer cell invasive growth. *Oncogene* **26,** 1078–87 (2007).

14. Monga, S. P. S., Mars, W. M., Pediaditakis, P., Bell, A., Mule, K., Bowen, W. C., Wang, X., Zarnegar, R. & Michalopoulos, G. K. Hepatocyte Growth Factor Induces Wnt-independent Nuclear Translocation of {beta}-Catenin after Met-{beta}-Catenin Dissociation in Hepatocytes. *Cancer Res.* **62,** 2064–2071 (2002).

15. Kapinas, K., Kessler, C., Ricks, T., Gronowicz, G. & Delany, A. M. miR-29 modulates Wnt signaling in human osteoblasts through a positive feedback loop. *J. Biol. Chem.* **285,** 25221–31 (2010).

16. Kang, D. W., Lee, S.-H., Yoon, J. W., Park, W.-S., Choi, K.-Y. & Min, D. S. Phospholipase D1 drives a positive feedback loop to reinforce the Wnt/beta-catenin/TCF signaling axis. *Cancer Res.* **70,** 4233–42 (2010).

## Appendix: Creative Commons License

This appendix contains the text of Creative Commons' Attribution-NonCommercial-NoDerivs License, version 4.0.[1]

### A.1 License Text

By exercising the Licensed Rights (defined below), You accept and agree to be bound by the terms and conditions of this Creative Commons Attribution-NonCommercial-NoDerivatives 4.0 International Public License ("Public License"). To the extent this Public License may be interpreted as a contract, You are granted the Licensed Rights in consideration of Your acceptance of these terms and conditions, and the Licensor grants You such rights in consideration of benefits the Licensor receives from making the Licensed Material available under these terms and conditions.

### Section 1 – Definitions.

a. **Adapted Material** means material subject to Copyright and Similar Rights that is derived from or based upon the Licensed Material and in which the Licensed Material is translated, altered, arranged, transformed, or otherwise modified in a manner requiring permission under the Copyright and Similar Rights held by the Licensor. For purposes of this Public License, where the Licensed Material is a musical work, performance, or sound recording, Adapted Material is always produced where the Licensed Material is synched in timed relation with a moving image.

---

[1] *See:* http://creativecommons.org/licenses/by-nc-nd/4.0/deed.en_US.

b. **Copyright and Similar Rights** means copyright and/or similar rights closely related to copyright including, without limitation, performance, broadcast, sound recording, and Sui Generis Database Rights, without regard to how the rights are labeled or categorized. For purposes of this Public License, the rights specified in Section 2(b)(1)-(2) are not Copyright and Similar Rights.

c. **Effective Technological Measures** means those measures that, in the absence of proper authority, may not be circumvented under laws fulfilling obligations under Article 11 of the WIPO Copyright Treaty adopted on December 20, 1996, and/or similar international agreements.

d. **Exceptions and Limitations** means fair use, fair dealing, and/or any other exception or limitation to Copyright and Similar Rights that applies to Your use of the Licensed Material.

e. **Licensed Material** means the artistic or literary work, database, or other material to which the Licensor applied this Public License.

f. **Licensed Rights** means the rights granted to You subject to the terms and conditions of this Public License, which are limited to all Copyright and Similar Rights that apply to Your use of the Licensed Material and that the Licensor has authority to license.

g. **Licensor** means the individual(s) or entity(ies) granting rights under this Public License.

h. **NonCommercial** means not primarily intended for or directed towards commercial advantage or monetary compensation. For purposes of this Public License, the exchange of the Licensed Material for other material subject to Copyright and Similar

Rights by digital file-sharing or similar means is NonCommercial provided there is no payment of monetary compensation in connection with the exchange.

i. **Share** means to provide material to the public by any means or process that requires permission under the Licensed Rights, such as reproduction, public display, public performance, distribution, dissemination, communication, or importation, and to make material available to the public including in ways that members of the public may access the material from a place and at a time individually chosen by them.

j. **Sui Generis Database Rights** means rights other than copyright resulting from Directive 96/9/EC of the European Parliament and of the Council of 11 March 1996 on the legal protection of databases, as amended and/or succeeded, as well as other essentially equivalent rights anywhere in the world.

k. **You** means the individual or entity exercising the Licensed Rights under this Public License. **Your** has a corresponding meaning.

**Section 2 – Scope.**

a. **License grant**.

   1. Subject to the terms and conditions of this Public License, the Licensor hereby grants You a worldwide, royalty-free, non-sublicensable, non-exclusive, irrevocable license to exercise the Licensed Rights in the Licensed Material to:

      A. reproduce and Share the Licensed Material, in whole or in part, for NonCommercial purposes only; and

      B. produce and reproduce, but not Share, Adapted Material for NonCommercial purposes only.

2. Exceptions and Limitations. For the avoidance of doubt, where Exceptions and Limitations apply to Your use, this Public License does not apply, and You do not need to comply with its terms and conditions.
3. Term. The term of this Public License is specified in Section 6(a).
4. Media and formats; technical modifications allowed. The Licensor authorizes You to exercise the Licensed Rights in all media and formats whether now known or hereafter created, and to make technical modifications necessary to do so. The Licensor waives and/or agrees not to assert any right or authority to forbid You from making technical modifications necessary to exercise the Licensed Rights, including technical modifications necessary to circumvent Effective Technological Measures. For purposes of this Public License, simply making modifications authorized by this Section 2(a)(4) never produces Adapted Material.
5. Downstream recipients.
    - A. Offer from the Licensor – Licensed Material. Every recipient of the Licensed Material automatically receives an offer from the Licensor to exercise the Licensed Rights under the terms and conditions of this Public License.
    - B. No downstream restrictions. You may not offer or impose any additional or different terms or conditions on, or apply any Effective Technological Measures to, the Licensed Material if doing so restricts exercise of the Licensed Rights by any recipient of the Licensed Material.

6. No endorsement. Nothing in this Public License constitutes or may be construed as permission to assert or imply that You are, or that Your use of the Licensed Material is, connected with, or sponsored, endorsed, or granted official status by, the Licensor or others designated to receive attribution as provided in Section 3(a)(1)(A)(i).

b. **Other rights**.

1. Moral rights, such as the right of integrity, are not licensed under this Public License, nor are publicity, privacy, and/or other similar personality rights; however, to the extent possible, the Licensor waives and/or agrees not to assert any such rights held by the Licensor to the limited extent necessary to allow You to exercise the Licensed Rights, but not otherwise.
2. Patent and trademark rights are not licensed under this Public License.
3. To the extent possible, the Licensor waives any right to collect royalties from You for the exercise of the Licensed Rights, whether directly or through a collecting society under any voluntary or waivable statutory or compulsory licensing scheme. In all other cases the Licensor expressly reserves any right to collect such royalties, including when the Licensed Material is used other than for NonCommercial purposes.

**Section 3 – License Conditions.**

Your exercise of the Licensed Rights is expressly made subject to the following conditions.

a. **Attribution**.

1. If You Share the Licensed Material, You must:

        A. retain the following if it is supplied by the Licensor with the Licensed Material:
            i. identification of the creator(s) of the Licensed Material and any others designated to receive attribution, in any reasonable manner requested by the Licensor (including by pseudonym if designated);
            ii. a copyright notice;
            iii. a notice that refers to this Public License;
            iv. a notice that refers to the disclaimer of warranties;
            v. a URI or hyperlink to the Licensed Material to the extent reasonably practicable;
        B. indicate if You modified the Licensed Material and retain an indication of any previous modifications; and
        C. indicate the Licensed Material is licensed under this Public License, and include the text of, or the URI or hyperlink to, this Public License.

    For the avoidance of doubt, You do not have permission under this Public License to Share Adapted Material.

2. You may satisfy the conditions in Section 3(a)(1) in any reasonable manner based on the medium, means, and context in which You Share the Licensed Material. For example, it may be reasonable to satisfy the conditions by providing a URI or hyperlink to a resource that includes the required information.

3. If requested by the Licensor, You must remove any of the information required by Section 3(a)(1)(A) to the extent reasonably practicable.

**Section 4 – Sui Generis Database Rights.**

Where the Licensed Rights include Sui Generis Database Rights that apply to Your use of the Licensed Material:

a. for the avoidance of doubt, Section 2(a)(1) grants You the right to extract, reuse, reproduce, and Share all or a substantial portion of the contents of the database for NonCommercial purposes only and provided You do not Share Adapted Material;
b. if You include all or a substantial portion of the database contents in a database in which You have Sui Generis Database Rights, then the database in which You have Sui Generis Database Rights (but not its individual contents) is Adapted Material; and
c. You must comply with the conditions in Section 3(a) if You Share all or a substantial portion of the contents of the database.

For the avoidance of doubt, this Section 4 supplements and does not replace Your obligations under this Public License where the Licensed Rights include other Copyright and Similar Rights.

**Section 5 – Disclaimer of Warranties and Limitation of Liability.**

a. Unless otherwise separately undertaken by the Licensor, to the extent possible, the Licensor offers the Licensed Material as-is and as-available, and makes no representations or warranties of any kind concerning the Licensed Material, whether express, implied, statutory, or other. This includes, without limitation, warranties of title, merchantability, fitness for a particular purpose, non-infringement, absence of latent or other defects, accuracy, or the presence or absence of errors, whether or not known or discoverable. Where disclaimers of warranties are not allowed in full or in part, this disclaimer may not apply to You.

b. To the extent possible, in no event will the Licensor be liable to You on any legal theory (including, without limitation, negligence) or otherwise for any direct, special, indirect, incidental, consequential, punitive, exemplary, or other losses, costs, expenses, or damages arising out of this Public License or use of the Licensed Material, even if the Licensor has been advised of the possibility of such losses, costs, expenses, or damages. Where a limitation of liability is not allowed in full or in part, this limitation may not apply to You.

c. The disclaimer of warranties and limitation of liability provided above shall be interpreted in a manner that, to the extent possible, most closely approximates an absolute disclaimer and waiver of all liability.

**Section 6 – Term and Termination.**

a. This Public License applies for the term of the Copyright and Similar Rights licensed here. However, if You fail to comply with this Public License, then Your rights under this Public License terminate automatically.

b. Where Your right to use the Licensed Material has terminated under Section 6(a), it reinstates:

   1. automatically as of the date the violation is cured, provided it is cured within 30 days of Your discovery of the violation; or
   2. upon express reinstatement by the Licensor.

   For the avoidance of doubt, this Section 6(b) does not affect any right the Licensor may have to seek remedies for Your violations of this Public License.

c. For the avoidance of doubt, the Licensor may also offer the Licensed Material under separate terms or conditions or stop distributing the Licensed Material at any time; however, doing so will not terminate this Public License.

d. Sections 1, 5, 6, 7, and 8 survive termination of this Public License.

**Section 7 – Other Terms and Conditions.**

a. The Licensor shall not be bound by any additional or different terms or conditions communicated by You unless expressly agreed.

b. Any arrangements, understandings, or agreements regarding the Licensed Material not stated herein are separate from and independent of the terms and conditions of this Public License.

**Section 8 – Interpretation.**

a. For the avoidance of doubt, this Public License does not, and shall not be interpreted to, reduce, limit, restrict, or impose conditions on any use of the Licensed Material that could lawfully be made without permission under this Public License.

b. To the extent possible, if any provision of this Public License is deemed unenforceable, it shall be automatically reformed to the minimum extent necessary to make it enforceable. If the provision cannot be reformed, it shall be severed from this Public License without affecting the enforceability of the remaining terms and conditions.

c. No term or condition of this Public License will be waived and no failure to comply consented to unless expressly agreed to by the Licensor.

d. Nothing in this Public License constitutes or may be interpreted as a limitation upon, or waiver of, any privileges and immunities that apply to the Licensor or You, including from the legal processes of any jurisdiction or authority.

## A.2 Creative Commons Notice

Creative Commons is not a party to its public licenses. Notwithstanding, Creative Commons may elect to apply one of its public licenses to material it publishes and in those instances will be considered the "Licensor." Except for the limited purpose of indicating that material is shared under a Creative Commons public license or as otherwise permitted by the Creative Commons policies published at creativecommons.org/policies, Creative Commons does not authorize the use of the trademark "Creative Commons" or any other trademark or logo of Creative Commons without its prior written consent including, without limitation, in connection with any unauthorized modifications to any of its public licenses or any other arrangements, understandings, or agreements concerning use of licensed material. For the avoidance of doubt, this paragraph does not form part of the public licenses. Creative Commons may be contacted at creativecommons.org.